Fatigue Life Time Estimates of Welded Joints in Maritime Structures

a total life concept

MSC thesis - Ruben Slange

21-9-2023

T̃U Delft

[This page is intentionally left blank.]

[This page is intentionally left blank.]

Thesis for the degree of MSc in Marine Technology
Specialization: *Ship and Offshore structures*

Fatigue Life Time Estimates of Welded Joints in Maritime Structures

By

Ruben Slange

Performed at

Bureau Veritas

This thesis MT.22/23.045.M is classified as confidential in accordance with the general conditions for projects performed by the TUDelft.

21-9-2023

Company supervisors
Responsible supervisor: Nick Daniels
E-mail: nick.daniels@bureauveritas.com
Daily Supervisor(s): Chris Booij
E-mail: chris.booij@bureauveritas.com

Thesis exam committee
Chair/Responsible Professor: Dr. Ir. Henk den Besten
Staff Member: Dr. Ir. Marko Pavlovic
Staff Member: Dr. Ir. Xiaoli Jiang
Staff Member: Ir. Mathieu Koetsier
Company Member: Ir. Chris Booij

Author Details
Studynumber: 4783484
Author contact e-mail: *rubenslange@gmail.com*

Preface

Dear reader,

This thesis, "Fatigue Life Time Estimates of Welded Joints in Maritime Structures, a total life concept," is my final project for the master Marine Technology at TU Delft. The work was performed with the guidance and supervision of Henk den Besten (TU Delft), Chris Booij (Bureau Veritas) and Nick Daniels (Bureau Veritas).

My interest in ships did not stem from sailing or any of those common reasons. However, a small study about massive ship structures piqued my interest. From there, the master direction reason follows logically because if you are interested in cool structures, then study structures. From the first year of my bachelor's, I enjoyed strength courses the most, and in the second year, cracks were introduced, which really grasped my attention as they threaten these large structures but start on a micro-scale. My bachelor end project followed concerning fatigue testing, which had the same front picture as present this thesis. Followed by the master where in the fatigue of maritime structures course, Henk den Besten opened the metaphorical fatigue can of worms, where I handed in four more assignments with this picture on the front. Leading to this master thesis.

My gratitude firstly extends to Henk den Besten for the great supervision, helpful insights, detailed feedback, critical questions that pushed me forward, and the amazing open-door policy. Secondly, my thanks extend to Chris Booij for the supervision at Bureau Veritas and for helping a lot by creating models for me to use in the case study and showing me around Bureau Veritas and their software. Furthermore, my gratitude extends to Nick Daniels for the supervision and feedback. It also extends to Saloni Palkar for providing the work for me to build upon and for answering questions that provided helpful insights. Moreover, although contact was limited to some emails, my thanks also extend to Francois Hild for answering some helpful questions.

Finally, my thanks extend to my family and friends for being there for me. Specifically, my parents for always being there for me, especially when I needed to get my mind on or off something and giving me way too good advice, and Stefan for being the guy I could talk to about all my fatigue-related problems whilst having fun.

<div align="right">

R.L.G. (Ruben Leonard Geert) Slange
Delft, September 2023

</div>

Summary

Ships at sea encounter wave-induced cyclic loading, meaning fatigue is a governing limit state. The structural response introduces stress concentrations, hotspots, at notch geometry like welded joints locations. At the same time, the welding process typically introduces defects, meaning welded joints are typically the governing fatigue-sensitive details. Accurate predictions of the fatigue lifetime are paramount for ensuring safety and economic viability in the maritime sector.

Because of the welding-induced defects, the fatigue lifetime of welded joints is growth rather than initiation-dominated; adopting a cracked geometry-based fatigue damage criterion like the stress intensity factor seems straightforward. Weld notch characteristic crack growth behaviour, however, becomes crucial. Since both short and long crack growth are considered important, a typical one-stage Paris relation-based long crack model must be extended, particularly since most of the welded joint fatigue lifetime is spent in the notch-affected short crack growth region. The short crack growth behaviour can be both non-monotonic as well as monotonically increasing, depending on the elastoplastic response conditions. A two-stage crack growth model, incorporating both short crack growth behaviour and the long crack growth characteristic, has already been proposed in a different project based on compact tension (CT) specimen crack growth testing results obtained using potential drop measurements. However, the corresponding strain/stress field possibly explaining the crack growth behaviour in terms of elastoplasticity is not part of the output. Images have been captured, which can be analyzed with Digital Image Correlation (DIC) to provide the field measurements.

The first aim of the research has been to explore dedicated displacement field formulations to capture the crack tip location and corresponding stress intensity factor simultaneously by developing a one-step DIC approach. The expected benefits of this approach over other DIC methods consist of an expected increase in accuracy and the elimination of a post-processing step. Current DIC methods generally exist out of a two-step approach. First, a DIC procedure is employed with a generalized kinematic basis. Secondly, a post-processing step is employed to determine the crack tip location and stress intensity factor (SIF). Specifically for the crack tip, the post-processing step generally assumes a dedicated kinematic basis function describing the field around the crack. Directly incorporating the dedicated function into the DIC procedure allows for the intermediate generalized kinematic assumptions to be eliminated.

The resulting crack size and SIF from this approach can be used to determine the crack growth relationship. This relationship can be used for the second aim of this thesis, which has been to determine the material parameters of the proposed two-stage crack growth model and validate its ability to capture the short crack growth behaviour.

However, the SIF values obtained with the developed one-step DIC do not align with the analytically obtained values. Regarding the crack growth relationship, this difference in loading introduces a mean shift. Nevertheless, the observed crack growth behaviour aligns with the trends established in prior investigations, which combined potential drop crack size results with analytically determined SIF values.

A three-step approach has been adopted to investigate the accuracy of the SIF determination:

Step 1: A direct approach using a finite element formulation based on global rather than local DIC, enforcing displacement field continuity as required for a crack path-independent SIF calculation.

Step 2: An indirect approach using the global DIC-based displacement field (step 1) and Williams' crack tip displacement field formulation (Williams, 1952) to obtain the crack tip location and SIF at the same time.

Step 3: A direct approach using Williams' crack tip displacement field formulation to obtain the crack tip location and the SIF simultaneously.

Analyses showed that involving Williams' asymptotic solution (steps 2 and 3) for long cracks in a simple far-field stress condition is beneficial. Accurate crack tip location and SIF estimates have been obtained. However, for complex stress fields at notched geometries additionally containing geometry boundaries in the same region, higher order terms are required to obtain a converged displacement field. An accuracy improvement has been observed when adopting a direct approach (step 3) rather than an indirect one (step 2) approach. A global FEM-based direct approach (step 1) allows for describing complex displacement fields and obtaining SIF estimates independent of the Williams' formulation. The resulting estimates from this approach agree with the Williams-based estimations (steps 2 and 3). From this, it can be concluded that the obtained difference in the SIF follows from a fundamental difference in the load obtained by analytical determination and the DIC approaches. This

conclusion is supported by the difference in the structural stress obtained from the DIC approaches compared to the analytical estimate.

The second aim of this thesis requires further investigation into the loading discrepancy before the total life model can undoubtedly be validated. Nevertheless, preliminary usage remains possible with the usage of consistent SIF determination. Resulting in the establishment of model parameters using likelihood regression for the CT and as-welded joint specimens.

For the final aim of this thesis, the total life fatigue strength criterion is obtained by integrating the two-stage crack growth model. This criterion is applied in a case study to estimate the total fatigue lifetime of a critical welded joint in a general cargo carrier. In order to determine the estimated lifetime of the critical joint, the fatigue loading is required. While knowledge of the cargo load is available, the impact of wave-induced loading requires investigation. Two distinct approaches have been used to determine the wave loading. Initially, Four representative wave loading scenarios established by Bureau Veritas regulations are considered. The cumulative fatigue damage resulting from these scenarios is then extrapolated to encompass the entirety of loading conditions experienced by the ship.

Secondly, a wave spectrum approach is undertaken to address uncertainties in loading analysis. A hydro-structural solver is utilized to calculate loading across various sea states. The total fatigue damage is based on a weighted average of a representative sea spectrum. The fatigue lifetimes derived from these methodologies are compared to the hot spot structural stress concept as typically adopted in industry for reference purposes. A comparison of the results shows that the hot spot structural stress concept underestimates the fatigue lifetime due to the increased conservatism required in this model.

Contents

Nomenclature

CT .... compact tension

DFT .... discrete fourier transform

DIC .... digital image correlation

FFT .... fast fourier transform

FT .... fourier transform

ROI .... region of interest

SIF .... stress intensity factor

TIE .... transport of intensity equation

ZOI .... zone of interest

Δ .... prefix indicating stress range

ϵ_{xx} .... normal strain x component

ϵ_{xx} .... shear strain component in xy plain

ϵ_{yy} .... normal strain y component

γ .... loading & response ratio coefficient

κ .... Kolosov's constant

∇ .... prefix indicating stress range

ν .... Poisson ratio

Ω .... real part complex base functions

ω .... real base function amplitude

Ψ .... base functions

σ_y .... monotonic yield stress

σ_b .... bending stress

σ_e .... material fatigue limit

σ_m .... membrane stress

σ_n .... notch stress distribution

σ_r .... residual stress distribution

σ_s .... hot spot structural stress

σ_{th} .... threshold stress

σ_{xx} .... normal stress x component

σ_{xx} .... shear stress component in xy plain

σ_{yc} .... cyclic yield stress

σ_{yy} .... normal stress y component

θ .... angular coordinate

Υ .... imaginary part complex base functions

ε .... correlation radii

G .... Shear modulus

$\frac{da}{dn}$ .... crack growth rate

a .... crack size

a_0 .... material length

a_n .... notch size

C .... crack growth rate curve intercept

d .... crack tip misalignment

f .... reference image

g .... deformed image

K_f .... far field stress intensity distribution

K_I .... total stress intensity distribution

K_{th} .... threshold stress intensity

m .... crack growth rate curve slope

N .... number of cycles until failure

n .... elastoplastic coefficient

$N(x)$ .... linear shape functions

r .... radial coordinate

r_s .... structural bending stress ratio

r_{lr} .... loading & response ratio

t_p .... plate thickness

u .... displacement

v .... imaginary base function amplitude

w_s .... plate width

Y_f .... far field factor

Y_n .... notch factor

1. Introduction

Fatigue is a governing limit state defining the lifetime of maritime structures. Accurate predictions of the fatigue lifetime are paramount for ensuring both safety and economic viability in the maritime sector. In this chapter, the motivation of the research to be performed will be discussed. In addition, the research goal, scope and relevance will be presented.

1.1. Motivation

The governing fatigue-sensitive details in maritime structures with respect to fatigue behaviour are the commonly arc-welded joints. These types of welded joints generally contain defects serving as nucleation locations for crack development. Because of the welding-induced defects, the crack initiation time is most likely small relative to the total fatigue life. At the same time, in the case of notched geometries, the high-stress concentrations at the notches can lead to relatively small nucleation lives. In these cases, the growth of a crack (both short and long) is the dominant factor in the total fatigue life of the joint. Therefore, a cracked geometry assessment concept is preferred in these cases.

Cracks growing from notches often exhibit a two-stage behaviour. Short crack growth close to the notch and long crack growth away from the notch. Although the long crack growth behaviour can typically be described using the Paris relation, short crack growth behaviour at (weld) notches is not well understood. Short crack growth behaviour can be monotonically increasing as well as non-monotonic and seems to be elastoplasticity affected, incorporating a mean stress effect (Palkar, not published yet). The different crack growth behaviours are illustrated in Fig.1.1. To capture these behaviours, a two-stage (short and long) crack growth model has been developed in the SCReen project (Palkar, not published yet).
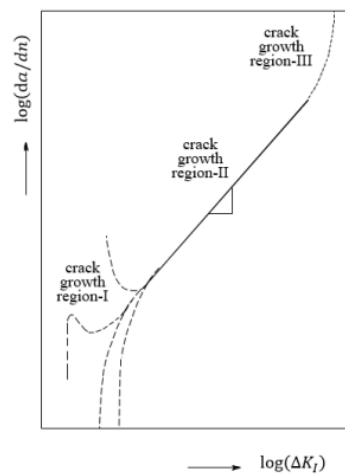

Figure 1.1: Crack growth behaviour (Palkar, not published)

The recently developed two-stage crack growth model is yet to be validated. Initial validation has been performed using potential drop measurements. Potential drop measurements can be used to measure the crack size in a specimen. These measurements are performed by applying an electrical current over the specimen and measuring the potential drop over the specimen. Propagation of the crack front reduces the material's thickness, increasing the electrical resistance. This increase in electrical resistance is measured as an increase in the potential drop over a specimen. Following, the increase in the potential is compared to the reference value of the specimen in uncracked condition, obtaining the change in potential drop. Calibration curves allow for estimating the crack size based upon the change in potential drop (Gandossi et al. 2001). These calibration curves can be established using analytical formulations or empirical formulations. For simple notch geometries, analytical formulations have been found by solving the Laplace equation (Clark & Knott, 1975). The main disadvantage of the potential drop method is the lack of information on the stress/strain field and stress intensity factors (SIF) values induced by the crack formation. Requiring analytical

formulations to obtain the SIF required for the crack growth relation. In addition, the accuracy of the measurement decreases in the case of empirical calibration curves (Gandossi et al. 2001).

Since images have been captured throughout the experiments, Digital Image Correlation (DIC) can be used to capture the crack tip location, the corresponding stress intensity factor, the crack tip stress/strain field information and the crack growth behaviour. In order to validate the two-stage crack growth model, the DIC procedure should be able to accurately handle discontinuities in the displacement field induced by the crack. Conventional DIC methodologies are assumed to have decreased accuracy when confronted with discontinuities, primarily attributed to the utilization of a generalized kinematic basis. Furthermore, the employment of a generalized kinematic basis necessitates a two-step procedure to obtain a continuous field description. This two-step approach includes the integration of the general kinematic basis as an intermediary step, thereby introducing a possible accuracy reduction. These disadvantages could be resolved by directly incorporating a relevant kinematic basis (Williams asymptotic solution (Williams, 1957)) in the DIC procedure, resulting in a one-step DIC approach (Vargas et al. 2016). The resulting one-step procedure can be used to simultaneously obtain the crack size and SIF of the specimens. Allowing for the crack growth relation to be obtained, this relation can be used to validate the two-stage crack growth model and obtain the relevant material parameters.

The validated two-stage crack growth model can be integrated to establish a total life-based fatigue strength criterion (Palkar, not published yet). This criterion is expected to have a reduced uncertainty compared to concepts commonly applied in engineering practice due to the increased stress state information incorporated. Reducing uncertainty reduces the required conservatism and improves the fatigue lifetime estimate. Bureau Veritas has provided a case study involving a ship structure containing unexpected cracks at different locations. The total life concept will be used for a fatigue assessment and compared to the hotspot structural stress concept commonly employed by Bureau Veritas. This comparison can provide insight into the use cases for this newly developed model, as in engineering practice, there is always a trade-off between accuracy and complexity.

1.2. Goal

The problem this research will be investigating follows from the gap in existing methods, and the current stage of development of the two-stage crack growth model. This problem can be formulated as follows:

> **The available crack growth models do (typically) not include all observed crack growth behaviour. A new model has been developed but needs to be validated using DIC (CT specimen experiment images) and verified (applying the model for fatigue assessment of a welded joint in a ship structure).**

In this statement, **the observed behaviour** refers to the non-monotonic short crack growth. In addition, **a new model** refers to the two-stage crack growth model developed by Palkar. Furthermore, **DIC** specifically refers to a one-step DIC approach, as mentioned in section 1.1, providing crack size and field information. The addition of this field information, compared to potential drop experiments, can help explain the deviant short crack growth behaviour.

1.3. Scope

In order to safeguard the feasibility of the study, some limitations are imposed on the scope. The determination of the field data through the use of DIC, is limited to analysing the far-field and notch region of a compact tension specimen. For the far-field region, only a mapping on the basic airy stress functions will be part of the scope. For the notch region, the assessment will be restricted to description by the truncated Williams asymptotic solution.

With respect to the validation of the two-stage crack growth model developed by Palkar, only earlier obtained data will be used. Meaning the execution of experiments will not be part of the research scope. This also allows for the obtained crack tip location to be compared to the results from potential drop experiments.

With concern to the analysis of the case study, the scope will be limited with respect to the loading. This research focuses on the structural response, and loading is therefore not of main concern. Initially, local water pressure and global hull girder forces/moments will be considered as governing load components. If shown to be insufficient, the critical load components will be searched for with the help of Bureau Veritas. Complete

modelling of the structure in order to obtain such loads is out of the scope, and in general the loading will be taken as provided by Bureau Veritas.

1.4. Relevance

It is crucial to consider the potential research implications before the research process. These include practical implications, scientific implications and societal implications.

1.4.1. Engineering

Practically this research will result in an integrated DIC code which can be used for fatigue crack assessment. Additionally, the crack growth of a ship will be assessed, hopefully resulting in a better prediction of the lifetime estimates. Such an improved estimate could then be used to assist in the judgement of repair. This could assist in a safer and extended lifetime of such a ship for when it is able to sail once more.

1.4.2. Science

This research aims to validate a new two-stage crack growth model. Validating such a model results in the next step towards the scientific goal of understanding crack growth behaviour. In addition, it provides a valuable tool for further research into crack growth analysis.

1.4.3. Society

The research helps to predict the lifetime of vessels better. This can in the end help to extend lifetime or reduce material usage. This reduces the impact of vessels on the environment. In addition, a better lifetime prediction can improve safety as it can prevent reaching the limit state.

1.5. Outline

This section provides an outline for the remaining part of the report. Shortly describing its content and relevance.

Initially, an exploration of current literature is performed to pursue the research's overarching objective. Starting in Chapter 2, different fatigue models are presented to provide insights into the research's underlying work. The well-established hotspot structural stress concept is discussed, which is currently the norm in engineering practice. This is followed by a discussion of the total life concept, a newly developed model to be validated within the scope of this research.

Chapter 3 presents the underlying mechanics of Digital Image Correlation (DIC) procedures. This chapter establishes the foundation upon which a one-step DIC procedure can be formulated and provides insight into the differently available DIC procedures. These alternative methods also provide a basis for comparison.

In tandem with this, Chapter 4 discusses image texture quality within the context of DIC procedures. The texture quality is relevant in determining feasible subset sizes for DIC analysis and serving as an image quality evaluation.

Continuing in Chapter 5, the analysis procedure of a far-field region is discussed. This analysis is important in accurately determining the applied loading magnitude on a specimen, which is important as a step in the validation procedure of the experimentally obtained model parameters.

In Chapter 6, the notch region analysis is described. This analysis is important because it can provide the Stress Intensity Factor (SIF) and the localization of the crack tip, both essential to describe the crack growth relation, providing insight into the current possibilities in literature to achieve the first aim of this research.

Following the literature, Chapter 7 identifies the research gap and sets out the research to be conducted in the form of a research hypothesis and research question followed by a series of sub-research questions.

The subsequent part of this thesis will describe the modelling performed in the context of this research. To this end, Chapter 8 presents the advancements within the two-step approach, followed by a description of the developed one-step DIC approach. With the developed one-step approach, the first aim of the thesis can be achieved by obtaining the crack tip location and field information in an integrated manner. Additionally, the

improvements in the two-step approach facilitate the two steps to evaluate the accuracy of the SIF obtained with the one-step approach.

In Chapter 9, the procedure will be described for obtaining the crack growth relation from the data obtained in the previous chapter. Furthermore, it is discussed how these crack growth relations can be used to estimate the parameters of the total life model. These procedures facilitate the second aim of this thesis of validating the total life concept.

Chapter 10 introduces the final modelling aspects required to achieve the final aim of this thesis, describing the calculations that facilitate the determination of the fatigue life for the case study. This modelling consists of the hotspot's loading determination and the hotspot's fatigue resistance following the total life model.

Subsequently, the thesis transitions to the presentation of the findings. Starting in Chapter 11, the DIC results concerning a few reference specimens are discussed to establish and validate the working of the developed one-step DIC approach and adjusted two-step approach.

Using the established DIC procedures, Chapter 12 presents the outcomes of the DIC analysis for the compact tension specimens, including a convergence study to determine the required amount of Williams terms. Furthermore, the crack-tip estimates, SIF estimates and resulting crack growth relation are compared to the results obtained in previous work through potential drop measurements and analytical formulations. This comparison allows for determining if the one-step DIC can effectively validate the crack growth model. Additionally, the loading upon the specimen is investigated by determining the structural stress following the applied forces and analytical determination. These results are compared to those from the DIC approaches to validate the applied and measured loading.

Chapter 13 presents the estimations of the parameters within the total life model for the compact tension specimen and as-welded data. These estimates are important in their contribution toward accurately determining the case study's lifetime behaviour, and validating the total life concept. Additionally, comparing the uncertainty of the data spread following the total life model and the structural hot spot concept provides an indication of the accuracy improvement.

Following the established parameters, Chapter 14 presents the case study's results, reaching this thesis's final aim. The fatigue lifetime following the total life concept is presented with wave loading based on a rule-based load case approach and a spectral approach. Besides, the results are compared to the structural hotspot stress results used according to the Bureau Veritas rules. These results provide valuable insights into the practical application of the total life model and its use in engineering practice.

The conclusions that can be drawn from the research are discussed in Chapter 15, presented according to the research question that followed from the literature review.

Lastly, Chapter 16 offers a discussion of the performed research. Additionally, it outlines avenues for potential future research and development.

I

Literature review

2. Fatigue models

Fatigue is a governing limit state defining the lifetime of maritime structures. Different models have been developed over time in order to estimate the fatigue lifetime. This chapter will present an overview of different concepts, and two concepts will be discussed in more detail. First, the structural hot spot stress concept, a common engineering concept, will be presented. Secondly, a state-of-the-art total lifetime concept will be discussed. These concepts serve as the foundation for the overarching goal of this thesis, which is to validate and implement the total life concept and provide a comparison with the structural hotspot concept.

2.1. Overview

Fatigue assessment concepts can be classified in accordance with den Besten, 2018 along four axes:

- Global or local information

- An intact or cracked geometry

- Stress, strain or energy-based

- Point, line or area/volume based

By taking more information into account, the dissimilarities between different structural details are incorporated. This reduces the amount of fatigue resistance curves, meaning a broader amount of structural details fatigue behaviour can be described by the same fatigue curve. This has the benefit that when designing a new detail, less or no additional experiments have to be conducted. In addition, it allows for more accurate fatigue life predictions and more possibilities for optimisation. An overview of the different concepts is presented in Fig. 2.1. Generally, when moving to the right in the figure, more similarities are included. However, a disadvantage of these models is that the complexity also increases.
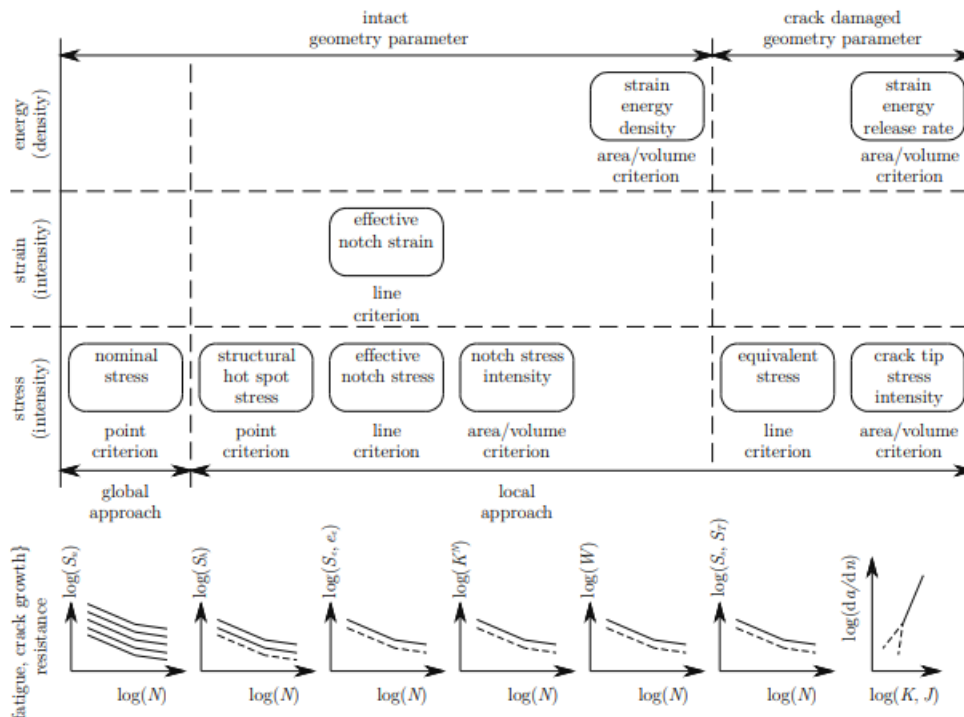

Figure 2.1: Fatigue assessment overview (den Besten, 2018)

The fatigue sensitive locations evaluated by these models can be loaded in a variety of ways, which can lead to different crack-opening modes. Three opening modes are distinguished, as can be seen in Fig 2.2. The first

two are in plane, and the third is out of plane. Often when using different concepts, only mode-I and mode-II effects are evaluated, as these are more prevalent in many structures.
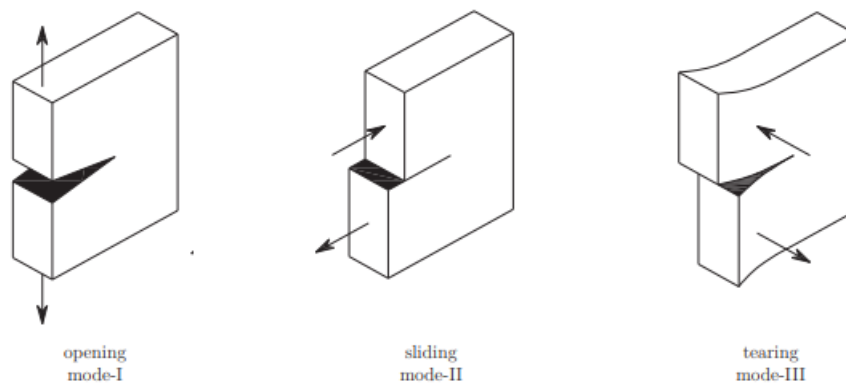

Figure 2.2: Crack surface displacement modes (Janssen et al. 2004)

Furthermore, different types of hot spots can be distinguished. This can be important as it can alter the procedure that needs to be taken within assessment concepts. The classification of the three types of hot spots in welded structures can be seen in Fig 2.3. Hot spot type A consists of notches at weld ends which develop cracks through the base plate. Hot spots type B are also located at the weld end but develop cracks over the full width of the plate, along the weld seam. Hot spot type C, on the contrary, is located along the weld seam and develops a through-thickness crack in the base plate.
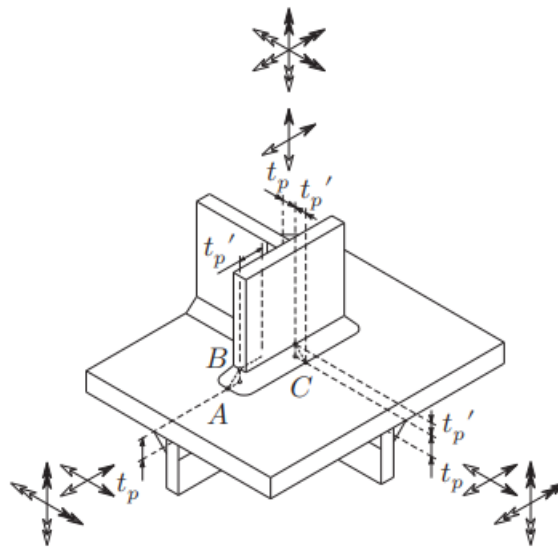

Figure 2.3: Classification of hot spots (den Besten, 2015)

2.2. Hot spot structural stress concept

The structural hot spot concept is commonly used in engineering practices. It is often prescribed by classification societies (e.g. Bureau Veritas rules: Steelships, Pt B, Ch 10, Sec 1, 4.2.5). It is an intact geometry concept, and it includes local information about the structural detail. It is a point criteria based upon a fictitious stress. The additional similarity included in this concept allows for a significant reduction in the amount of S-N curves to one curve for non-load-carrying joints and one for load-carrying joints. In order to obtain the structural stress, the stress distribution is linearized through the base plate thickness. This concept models the force- and moment equilibrium of the actual stress distribution at the notch. It, however, does not

model the actual geometry of the notch and the size of the components. Several options for this linearisation exist in literature: Linear surface extrapolation, non-linear surface extrapolation, virtual node below the surface and through-thickness linearisation.

Linear surface extrapolation makes use makes use of two points. The first point is just outside the notch-affected region. The second also called the reference point, is located further away. The exact distances are generally an engineering judgement; however, guidelines are provided by the IIW. In Fig. 2.4, the recommended distances as provided by the IIW can be seen. In the case of hot spot type B, non-linear surface extrapolation is generally recommended. This exists out of three points and extrapolates with a quadratic base.
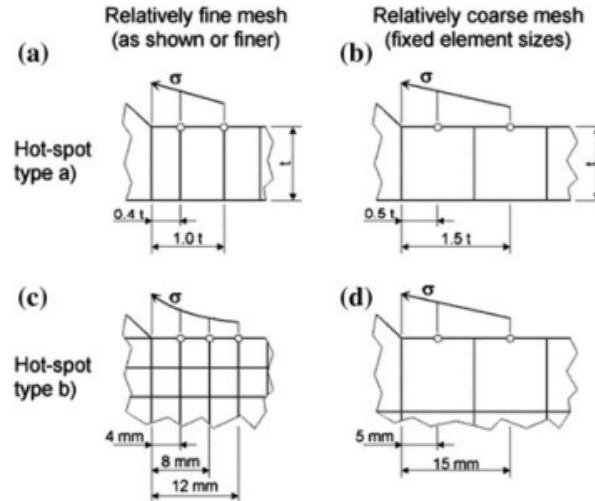

Figure 2.4: Reference points at different types of meshing. Stress type "a" (a, b), type "b" (c, d) (Hobbacher et al. 2016)

The sub-surface virtual node method takes the through-thickness stress value at the transition location from notch affected to far-field dominated region. This location can be obtained using a FEM solid model and is generally taken as 10% of the base plate thickness (Xiao & Yamada, 2004).

The last method is through-thickness linearization. This method can either be executed by a shell or solid finite element model.

In a shell model, the sectional moments and forces can be used to calculate the structural stress in Fig. 2.5 it can be seen how these values are defined at section B-B. The values can then be used in the equation below to obtain the structural stress in section AA (e.g. the weld) (Dong, 2001).

$$\sigma_s = \sigma_m + \sigma_b = f_{x'} t + 6(m_{y'} + \delta \cdot f_{z'}) t^2 \tag{2.1}$$
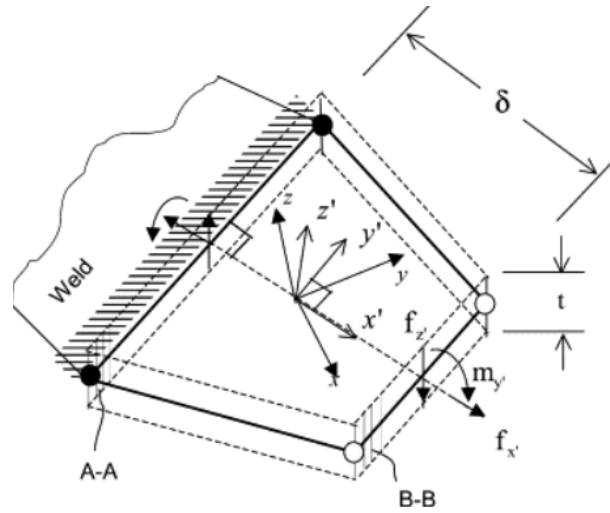
Figure 2.5: Structural stress procedures for a shell/plate element adjacent to a weld (Dong, 2001)

A similar procedure exists for a solid model. Moment and force equilibrium is exploited in order to define the structural stress at the weld from nodal forces and moments. In Fig. 2.6, the procedure for a solid model can be seen. The definition of the equilibrium equations in order to obtain the two structural stress components can be seen underneath (Dong, 2001).

$$\sigma_m = \frac{1}{t}\int_0^t \sigma_x(y) \cdot dy \tag{2.2}$$

$$\sigma_m\frac{t^2}{2} + \sigma_b\frac{t^2}{6} = \int_0^t \sigma_x(y) \cdot y \cdot dy + \delta\int_0^t \tau_{xy}(y) \cdot dy \tag{2.3}$$
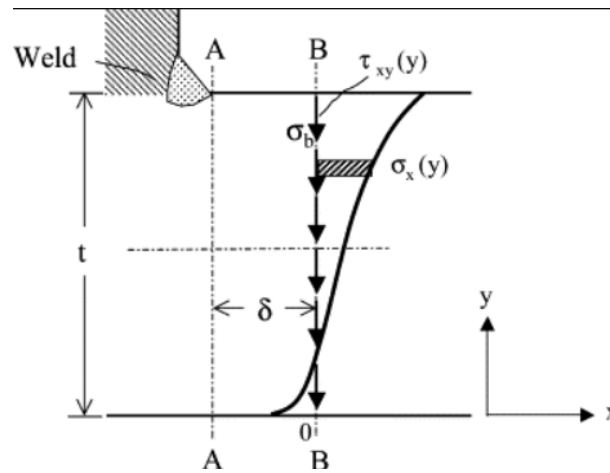
Figure 2.6: Structural stress procedures for a solid element model adjacent to a weld (Dong, 2001)

Alternatively, the structural stress formulation can be obtained from the nodal forces at the weld (A-A Fig. 2.6). In which the nodal forces are defined per unit width (Dong et al. 2006).

$$\sigma_{s,m} = \frac{\sum f_{x,i}}{tp} \tag{2.4}$$

$$\sigma_{s,b} = \frac{6(\sum f_{x,i} \cdot y_i - \sigma_{s,m} \cdot \frac{tp^2}{2})}{tp^2} \tag{2.5}$$

By obtaining the structural stress in maximum and minimum loading conditions, or the maximum whilst loaded in the opposite direction, the stress range can be defined ($\Delta\sigma_h = \sigma_{s,max} - \sigma_{s,min}$). This stress range

functions as the fatigue resistance criteria ($S_h = \Delta\sigma_h$) which can then be plotted against the number of cycles resulting in a Basquin-type relationship (S-N curve, $N = C \cdot S_h^{-m}$). However, because this stress range does not include the local geometry affected self-equilibrating stress, a theoretically infinite amount of fatigue resistance curves exist. In practice, only two extremes are distinguished. One for the weld load carrying (LC) cases and one for the non-load carrying cases (NLC). These two cases have a corresponding FAT class, and usage depends on engineering judgement.

2.3. Total life concept

A two-stage (short and long) crack growth model has been developed in the SCReen project (Palkar, not published yet); the model is based on the total stress intensity concept (den Besten, 2015). The total stress concept makes use of a stress-dependent crack growth model. A fatigue resistance parameter can be obtained by integrating the crack growth model over a representative crack size interval. The resulting concept is a local cracked geometry stress-based area criteria. In order to make the crack growth model as accurate as possible, the complete stress description at a hot spot is supposed to be captured. Therefore, these models include multiple stress contributions that combine to the so-called total stress. Both the new model and the total stress model include the geometry effects through the stress intensity factor (SIF). In addition, they both incorporate mean stress effects and notch plasticity. The total life concept improves upon the existing total stress description by including the threshold stresses and expanding the plasticity effect description. This new model was tested upon standard compact tension specimens (Fig 2.7). These types of specimens are widely used in order to determine the fatigue resistance of different materials.
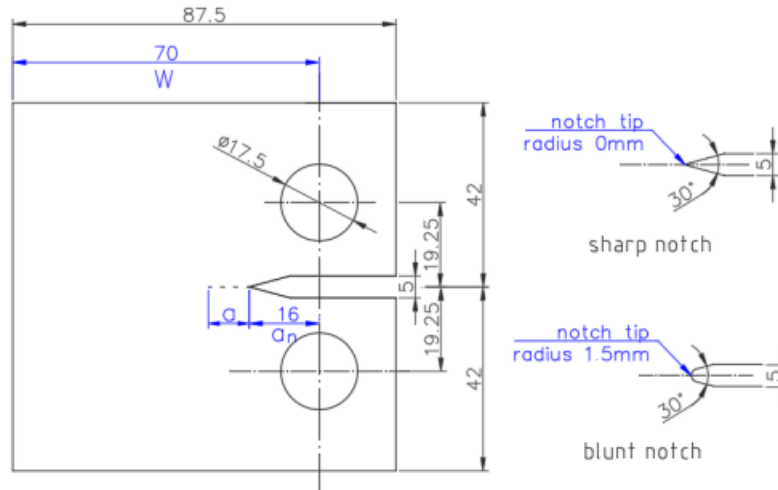

Figure 2.7: Standard Compact Tension specimen (Palkar, not published yet)

Compact tension specimens are generally only loaded in mode-I. Therefore, only the stress distribution and stress intensity factor of mode-I have to be taken into account in this application of the model.

The formulation of the Stress Intensity factor (SIF) for crack growth at a notch undergoing mode-I loading is given in equation 2.6. It comprises of a notch-related factor (Eq. 2.7), a far-field related factor (Eq. 2.8), the structural stress and a notch-angle related factor. The notch factor includes the analytical notch stress description. This description is dependent on symmetry and different geometric parameters; the further procedure is equivalent for every type of hot spot. Specific analytical formulations for the notch stress have been derived for CT specimens. Appropriate analytical functions can be used as a basis and combined with FEM to obtain the load-carrying factor. The far-field factor has been established parametrically as no complete analytical solution exists for a CT specimen.

The stress intensity formulation has been validated for all three different types of hot spots (Qin et al. 2021; Qin et al. 2019).

$$K_I(\frac{a}{tp}) = \sigma_s\sqrt{tp} \cdot Y_n(\frac{a}{tp}) \cdot Y_f(\frac{a}{tp}) \cdot \sqrt{\pi(\frac{a}{tp})} \qquad (2.6)$$

$$Y_n(\frac{a}{t_p}) = \frac{2}{\pi} \int_0^1 \frac{\sigma_n(\frac{r}{a} \cdot \frac{a}{t_p})/\sigma_s}{\sqrt{1 - (\frac{r}{a})^2}} d(\frac{r}{a}) \tag{2.7}$$

$$Y_f(\frac{a}{t_p}) = Y_{fm} - r_s(Y_{fm} - Y_{fb}) \tag{2.8}$$

Cracks only propagate when the stress level at the crack is high enough. For this reason, the two-stage model of Palkar includes a material-dependent threshold intensity K_{th}. It is purely material-dependent, and formulations for it have been developed previously (Tanaka et al. 1981).

$$\Delta K_{th} = \Delta \sigma_{th} \cdot \sqrt{\pi(a + a_0)} \tag{2.9}$$

Another critical factor in crack growth is mean stress. In addition, the assumption has been made that the negative part of the loading cycle does not contribute to the crack growth. These effects have been Incorporated through the loading response ratio and the loading and response ratio coefficient. Lastly, plasticity-induced residual stresses are included through plasticity correction factors n_1 to $n4$. Because, for fatigue loading, residual stress generated in the previous cycle is present as mean stress in the next cycle (Palkar, not published). The $(1 - r_l r)$ term corrects for the increased mean stress in the notch region. Whilst the $(\sigma_m ax/\sigma_y)$ term corrects for the load dependent size of the plasticity affected region. Including all these factors leads to the full two-stage model. In which the unknown parameters C, K_{th}, γ, m and $n_1 - n_4$ are only material dependent and can be obtained by a maximum likelihood estimate (Palkar, not published).

$$\frac{da}{dn} = C * \left[\frac{(Y_n + n_1 \cdot Y_n^{n_2 \cdot (1 - r_{lr})^{n_3} \cdot (\frac{\sigma max}{\sigma_y})^{n_4}}) \cdot Y_f \cdot (\Delta\sigma_s\sqrt{\pi a} - \Delta K_{th})}{(1 - r_{lr})^{1 - \gamma}} \right]^m \tag{2.10}$$

$$\log(\frac{da}{dn}) = \log(C) + m \cdot \log \left[\frac{(Y_n + n_1 \cdot Y_n^{n_2 \cdot (1 - r_{lr})^{n_3} \cdot (\frac{\sigma max}{\sigma_y})^{n_4}}) \cdot Y_f \cdot (\Delta\sigma_s\sqrt{\pi a} - \Delta K_{th})}{(1 - r_{lr})^{1 - \gamma}} \right] \tag{2.11}$$

$$r_{lr} = \frac{\sigma_{s,min}}{\sigma_{s,max}} \tag{2.12}$$

$$\gamma = p \quad \forall \quad (r_l \geq 0) \tag{2.13}$$
$$\gamma = 0 \quad \forall \quad (r_l < 0) \tag{2.14}$$

Due to the inclusion of the plasticity-induced residual stresses, the model is able to predict non-monotonic behaviour in the initial crack growth stage.

For a fatigue lifetime evaluation, not only the crack growth rate but also the total lifetime is of interest. Equivalent to the total stress model (den Besten, 2015), this can be done by an integration procedure resulting in a Basquin-type fatigue resistance relation (Eq. 2.15, 2.16), This model however loses the idea of a threshold stress. Instead a bi-linear Basquin model, a ordinary random fatigue limit model, a piecewise-continuous bi-linear random fatigue limit model or a generalised random fatigue limit model can be introduced to capture this behaviour (Qin et al. 2021) . Important to note here are the integration bounds; these bounds should not necessarily extend from a crack size of zero to the entire thickness of the material. Firstly, because at a crack size of zero, the integral shows a singularity. It is generally accepted that an initial defect size exists, which can vary depending on the material and construction method. For aluminium, it has been found to be approximately $\frac{a_i}{t_p} = 6 * 10^{-3}$, and for steel it is argued to be $\frac{a_i}{t_p} = 1 * 10^{-3}$ (Qin et al. 2019). This initial defect size may include statistical components besides the actual initial crack size due to back-calculation with maximum likelihood estimations. Another option is to adjust the final crack size to account for statistical effects. This can be relevant when using a two-stage model, as it does not physically make sense to extend the analysis to the final crack growth stage if the model does not include this behaviour.

$$\log(N) = \log(C^{-1}) - m \cdot \log(S_T) \tag{2.15}$$

$$S_T = \frac{\Delta\sigma_s}{(1 - r_{lr})^{1-\gamma} \cdot t_p^{\frac{2-m}{2m}} \cdot I_n^{\frac{1}{m}}} \tag{2.16}$$

$$I_n = \int_{a_f/t_p}^{a_i/t_p} \left(\frac{1}{(Y_n(\frac{a}{tp}) + n_1 \cdot Y_n(\frac{a}{tp})^{n_2 \cdot (1-r_{lr})^{n_3} \cdot (\frac{\sigma_{max}}{\sigma_y})^{n_4}}) \cdot Y_f(\frac{a}{tp}) \cdot \sqrt{\pi \frac{a}{tp}}} \right)^m d(\frac{a}{t_p}) \tag{2.17}$$

The new crack growth model has currently been validated through the use of potential drop measurements. However, these measurements do not provide stress/strain field information at the crack tip. Instead, Digital Image Correlation (DIC) could be used in order to capture the crack tip location (Roux and Hild, 2006), the corresponding stress intensity factor, the crack tip stress/strain field information and last but not least the crack growth behaviour.

3. Digital Image Correlation (DIC)

This chapter discusses the Digital Image Correlation (DIC) procedures principles. Providing a framework for the overarching aim of developing a one-step DIC approach. Following, the distinction between local (subset-based) and global (FEM-based) DIC approaches is discussed. Furthermore, specific concepts required for implementing these types of procedures will be presented. While the primary emphasis is placed on the concepts employed in the FEM-based implementation of Besnard et al. 2006, it is imperative to note that most of these concepts are widely adopted within the field of DIC. Furthermore, where applicable, some alternative approaches are highlighted. Subsequently, the different possible kinematic assumptions are examined. Lastly, the two possible DIC approaches are discussed based on the assumed kinematic basis.

3.1. Principles

Digital image correlation (DIC) is the process used to measure the displacement in an object by comparing consecutive images of the same object taken at different times or under different loading conditions. One of the applications is in objects that have experienced deformation due to the application of a certain load. When one picture has been taken before the load application and one afterwards, DIC can be used to capture the displacements and their derivatives. This can be used to compute the strain and stress field in the material.

Before a DIC algorithm can be used the images must be obtained first. This is an important step as it will significantly influence the DIC performance. Pictures can be captured by stereo set-ups which allow for 3D information to be captured or just single cameras. Furthermore, the resolution of the picture is essential as it determines the maximum resolution of the DIC algorithm. However, the resolution is also influenced by the object of which the picture is taken. Because when matching displacements, there need to be unique features to match. Therefore, one should be applied artificially when a surface does not have a fine and random structure. For example, this can be done by airbrushing a random dotted pattern on top of the surface. In Fig. 3.1, underneath an example of a set-up to take pictures for DIC can be seen.

Figure 3.1: Example DIC setup (den Besten, 2015)

In a DIC algorithm, the images are converted into a pure grey scale or must be inserted in such a format. Each pixel has one value in this format, i.e. its grey-scale value. The pixel values from the two images can then be compared. However, evaluating the whole picture at once does generally not work because in such case, only rigid body motions can be measured. On the other hand, single pixels can not be used either because there are multiple pixels with the same grey scale values. This results in no unique displacement solution existing. Therefore, pixels are grouped in so-called zones of interest (equivalent: subset, facet, element) to satisfy the uniqueness requirement.
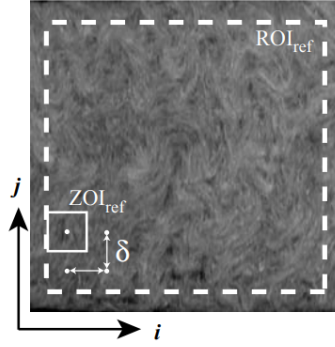
Figure 3.2: Example of a zone of interest (ZOI) inside a region of interest (ROI) (Réthoré et al. 2008)

The reference and deformed images are respectively called f(x) and g(x). An simplified diagram illustrating this process can be seen in Fig. 3.3.
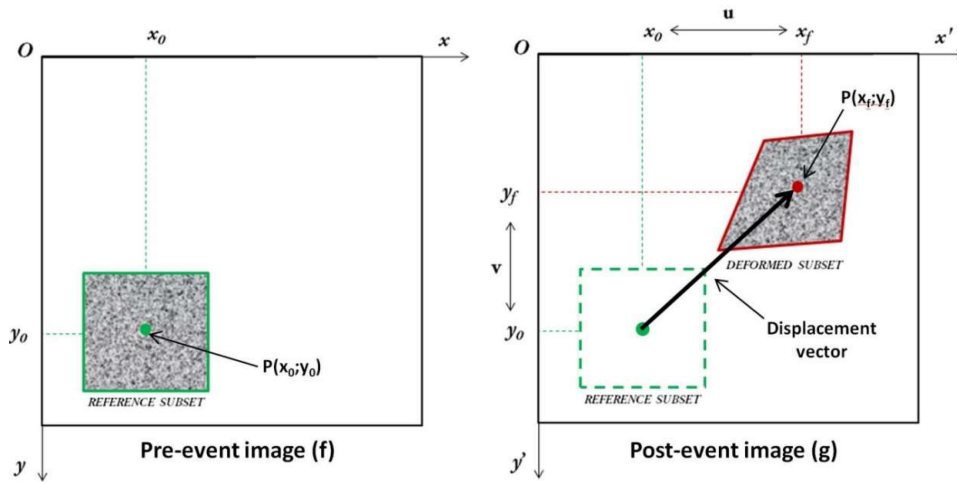

Figure 3.3: Schematic diagram of the basic principle of DIC (Caporossi et al. 2018)

In the method of Besnard et al. 2006 the assumption of conservation of optical flow is made, meaning that the apparent movement in an image is solely due to actual movement. This assumption could be invalidated when the applied texture is not random. Because, in such cases, an apparent optical motion could take place. One example would be a rotating bar with a helix pattern on its surface, as the helix would seem to move upward whilst it is purely rotating. Another case violating this assumption would be an observed change of brightness in the pattern. If such a change occurs, it is only possible to match pixel clusters appropriately if the change is specifically taken into account. Therefore lighting conditions must stay the same between images. These assumptions generally hold in lab conditions for two-dimensional analysis. The conservation property in mathematical terms is expressed below. In this description, f represents the original image and g the deformed image.

$$g(x) = f[x + u(x)] \tag{3.1}$$

Assuming that the reference image is differentiable, a first-order Taylor expansion of the optical flow conservation yields:

$$g(x) = f(x) + u(x) * \nabla f(x) \tag{3.2}$$

Various correlation criteria (i.e. similarity measures for f(x+u(x)) and g(x)) exist for DIC: Direct cross-correlation, zero mean cross-correlation, zero mean sum of squared differences, sum of squared differences and Parametric Sum of Squared Difference(Pan et al. 2010,Sutton et al. 2009). Maximising the cross-correlation criteria correspond to the minimisation of an equivalent sum of squared difference criteria.

$$DCC : \sum f_i g_i \tag{3.3}$$

$$ZMCC : \sum((f_i - \bar{f}) - (g_i - \bar{g})) \tag{3.4}$$

$$ZMSSD : \sum((f_i - \bar{f}) - (g_i - \bar{g}))^2 \tag{3.5}$$

$$SSD : \sum(f_i - g_i)^2 \tag{3.6}$$

$$PSSD : \sum(f_i + b - g_i)^2 \tag{3.7}$$

In these formulations, $\bar{f}$ and $\bar{g}$ the average of the summed subsets ($\bar{f} = \frac{1}{n}\sum f_i$). The differences between the different methods are mainly concerned with computational time and light intensity changes. However, as long as the optical flow conservation assumption holds, only computational time matters in the procedural choice Pan et al. 2010. Therefore, implementing the sum of squared differences is logical, as it is the computationally fastest of the criteria (Pan et al. 2010).

Because of the aforementioned uniqueness requirement, blocks of pixels (ZOI) are compared, and for that reason, the squared difference needs to be integrated over its area. Incorporating the integration and the image Taylor expansion results in the formulation to be minimised (Eq. 3.8).

$$\eta^2 = \int\int_\Omega [u(x) * \nabla f(x) + f(x) - g(x)]^2 dx \tag{3.8}$$

Within the existing procedures, DIC can mainly be divided along four axes. As discussed, based on certain assumptions and computational speed, different procedures can be chosen.

The first difference is the correlation procedure. The second differentiating factor is the dimension of the analysis. Two-dimensional DIC is the most accessible as the algorithms are less complex and only require a single camera. Three-dimensional DIC traditionally requires stereo setups to get a depth of field. Such a stereo setup consists of two cameras positioned at different angles. A sense of depth and three-dimensional space can be created by applying a 3D DIC (digital image correlation) algorithm to the images captured by the stereo setup. This technique is analogous to human depth perception, which relies on the use of two eyes to perceive the distance of objects in the environment. In Fig. 3.4 a sketch of such a stereo setup can be seen.
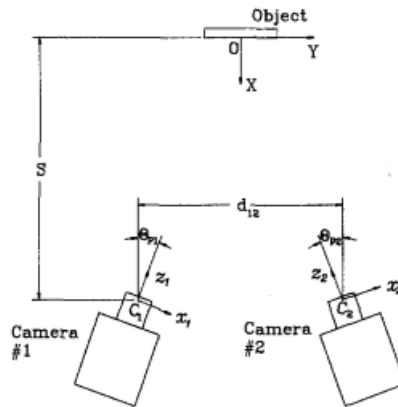

Figure 3.4: Stereo setup sketch (Luo et al. 1993)

The main disadvantage of stereo setups is the increase in cost and complexity; however, progress has been made towards only needing a single camera to capture the 3D field (Wu et al. 2022).

Furthermore, the methods distinguish themselves on the matching area. The ZOI's can be matched individually (local DIC) or in a brother framework (Global DIC). The chosen method influences the last difference between methods, namely the basis functions. The displacements are assumed to behave according to a particular function. These can be general or special to the situation at hand assumed base functions.

3.2. Local subset-based formulation

Drawing from the principles of the DIC, the most rational implementation strategy would be a subset-based approach. The subset-based DIC process analyses images in a point-by-point manner to determine the deformation. At every measurement point, a reference subset (ZOI) is selected, centred around this measurement point. The counterpart of this subset is then sought for in the deformed image by matching

with the highest degree of similarity (Wang et al. 2015). When evaluating the correlation criteria (Eq. 3.8), this means the domain over which the integration takes place is constrained to the subset. This has the advantage of being able to perform the correlation procedure in parallel (Yang & Bhattacharya, 2019). There exist multiple ways to solve the correlation procedure, including the Inverse Compositional Gauss-Newton (IC-GN) scheme (Baker & Matthews, 2004; Besnard et al. 2012; Yang & Bhattacharya, 2019), the Inverse Compositional Levenberg-Marquardt (IC-LM) scheme (Baker & Matthews, 2004) and FFT based approaches (Grebenyuk & Ryabukho, 2011).

In subset-based DIC, each subset is analysed independently, without taking into account the relationship or continuity with other subsets. Therefore, inter-subset continuity is not enforced during the correlation process. This lack of inter-subset continuity can lead to inaccuracies in the displacement and deformation measurements, particularly in cases where there are large deformations or non-uniform displacement fields. This is a significant shortcoming of the subset-based DIC method, as it could result in a lack of continuity and smoothness in the displacement field and can introduce errors in the measurements (Hild & Roux, 2012; Wang et al. 2015).

Some techniques have been developed to overcome these limitations, such as filtering the image signal. This reduces noise and improves accuracy due to the implicit incorporation of information from surrounding regions (Yang & Bhattacharya, 2019). Alternatively, constraints can also be incorporated to satisfy continuity in the form of Lagrange multipliers. This divides the problem into two subproblems, one is solved locally, as in the standard subset approach, and one constitutes of a global updating (Yang & Bhattacharya, 2019).

3.3. Global (Finite element based) formulation

In order to overcome the issues related to subset DIC, a more global approach has been developed. Global or FEM-based DIC evaluates all the subsets at the same time. It creates an element mesh out the different subsets. These elements are connected by shared nodes from which elemental shape functions are defined. A global correlation matrix is established from these elements, allowing for a continuous displacement field (Fig. 3.5). This approach has been shown to improve accuracy (Hild & Roux, 2012; Yang & Bhattacharya, 2019). This improvement can be explained by the fact that the individual correlation of the subsets is more susceptible to local imaging problems, introduces discontinuities that can lead to issues with deformation gradient calculation and is generally noisier (Yang & Bhattacharya, 2019).

Furthermore, the FEM-like description allows applying the obtained displacements onto a finite element model to determine the nodal forces and stresses. These forces and stresses can be used to obtain an estimation of the applied loading. The FEM-based DIC analysis also allows for the post-processing steps commonly employed in FEM. For example, path-independent integrals can be calculated to determine stress intensity values (SIF) due to the enforced continuity (Barhli et al. 2017; Bower, 2009).
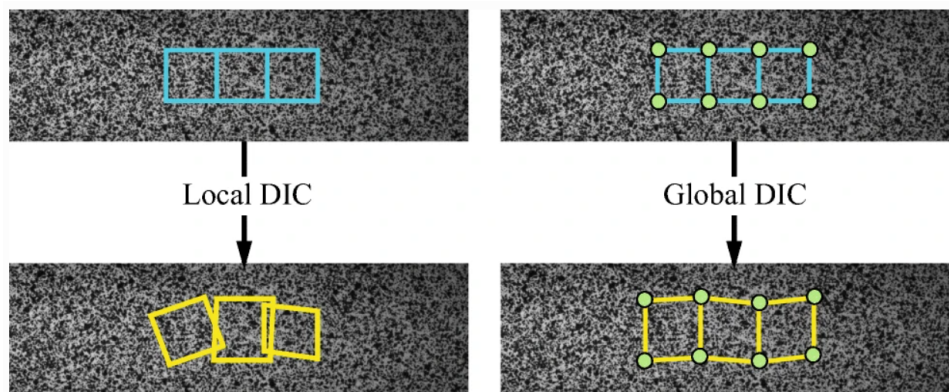
Figure 3.5: Comparison between local (subset-based) and Global (Fem based) DIC (Yang & Bhattacharya, 2019)

The general DIC principles have been explained in section 3.1. The implementation of a FEM-based DIC procedure requires some additional concepts. The concepts Besnard et al. 2006 makes use of are discussed in the sections below, as well as some alternatives for these specific implementations. Some of the implemented concepts are optional based on the type of images considered.

3.3.1. Elements

Essential for a FEM-based DIC approach is the chosen element base. In the implementation of Besnard et al. 2006, Q4P1 elements are chosen to function as the displacement field base functions. These elements are quadrilaterals consisting of 4 nodes at their corner points. These types of elements are a logical choice in the case of DIC due to the rectangular nature of pixels, as well it allows for easy comparison with FEA models (Besnard et al. 2006). A representation of such an element and its shape function can be seen Fig. 3.6.
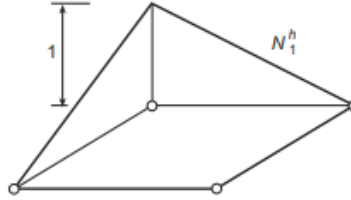

Figure 3.6: Q4P1 element and shape function of node 1 (Zienkiewicz & Taylor, 2000)

The sizing of these elements is set to encompass the defined ZOI size. With this element formulation, the displacement field within an element can be constructed as a summation of shape functions and respective amplitudes (Eq. 3.9). In this specific formulation, there exist a total of eight amplitudes, which are dependent on the chosen basis. Two amplitudes per elemental node for both the x and y directions.

$$u^e(x) = \sum_{n=1}^{4} \sum_{\alpha} a_{\alpha n}^e N_n(x) e_\alpha \tag{3.9}$$

The elemental displacement description can be utilised in the correlation criteria (Eq. 3.8). However, in order to calculate the quadratic difference for the whole image, a summation over the elements is required.

$$\eta^2 = \sum_e \int \int_\Omega \left[\sum_{\alpha,n} a_{\alpha n}^e N_n(x) \nabla f(x).e_\alpha + f(x) - g(x) \right]^2 dx \tag{3.10}$$

In this formulation, $\nabla f.e_\alpha$ denotes the directional derivative, which follows from the directionality present in the displacement formulation (Eq. 3.9). In order to obtain the displacements, this function needs to be minimised, which corresponds to setting the derivative with respect to the objective (i.e. the sought for amplitudes) equal to zero. Rewriting this results in a linear system, where the solutions are the amplitudes of the element displacements.

$$\sum_{\beta,m} a_{\beta,m}^e \int \int_{\Omega_e} [N_m(x) N_n(x) \partial_\alpha f(x) \partial_\beta f(x)] dx = \int \int_{\Omega_e} [g(x) - f(x)] N_n(x) \partial_\alpha f(x) dx \tag{3.11}$$

$$\mathbf{Ma} = \mathbf{b} \tag{3.12}$$

The individual components of the matrices to be solved can be formulated as in equations 3.13 and 3.14. In which the index e represents the element, subscripts n and m represent the row and column and α and β the direction.

$$\mathbf{M}_{\alpha n \beta m}^e = \int \int_{\Omega_e} [N_m(x) N_n(x) \partial_\alpha f(x) \partial_\beta f(x)] dx \tag{3.13}$$

$$\mathbf{b}_{\alpha n}^e = \int \int_{\Omega_e} [g(x) - f(x)] N_n(x) \partial_\alpha f(x) dx \tag{3.14}$$

Due to the random nature of the evaluated texture, standard FEA integration schemes (e.g. Gauss integration) can not be used. For this reason, a Riemann sum needs to suffice instead (Besnard et al. 2006). The inside of the integrals are calculated for each pixel within an element, after which they are summed up to result in the element contribution.

Independent of the chosen base functions, an issue arises in the M-matrix. Because the role played by images f and g is symmetric and up to second-order terms, exchanging them simply leads to a change of sign. This is due to the Taylor approximation of the deformed image in Eq. 3.2, as the original image could also be formulated

as the deformed image minus the deformation. In order to compensate for variations of the texture and to cancel the first-order induced error in u, the original image f(x) can be substituted by the average of the original and deformed image (f(x)+g(x))/2 Besnard et al. 2006. This substitution does not have to be done for the b-elemental description, as the same issue doe not occur here. This makes the estimate of the displacement field more stable and accurate. The downside is the increased computation time to establish the element matrices.

3.3.2. Masking

In case an object does not cover the entire image, masking is required. Because the DIC algorithm requires uniqueness for it to match the pixels. Therefore, parts outside any object should be masked away. In case proper lighting conditions are in place, an automated masking procedure can be used in order to mask away the background based on the high contrast. This procedure could be beneficial in the case of odd-shaped structures where manual masking can prove to be complicated. Especially in these cases, it is important for the masking procedure to maintain the original coordinates of the region in order to see the effects in the bigger picture. Masking can also be used to speed up computation time; if the region of interest for the displacement field is not the entire object, the additional area can be masked. In fatigue experiments, masking can also be used to separate the object into different sections in order to capture information relevant to these sections. The two areas of Interest at a hot spot location are the notch-affected region and the far field region (Fig. 3.7).
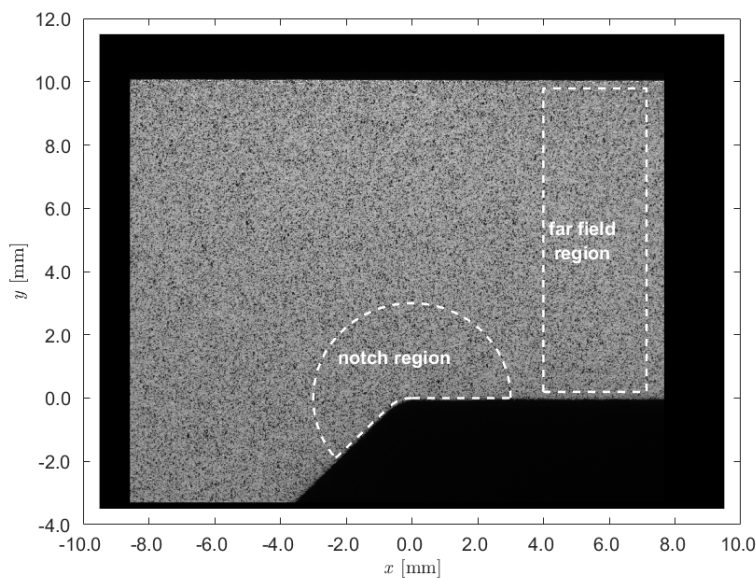

Figure 3.7: Respective notch and far field region

3.3.3. Fourier transform

The Fourier transform is the mathematical technique used to decompose a function into its individual frequency components. A signal is transformed into a rotating signal in the complex plane by multiplying it with an exponential (Maljar & Stopjaková, 2021). Where its radius describes the magnitude of the original signal, and the angle relates to its original coordinate or phase angle. However, in the transformation from coordinate to angle, a frequency is introduced in the power of the exponent and can be arbitrarily chosen. By integrating the transformed function, the apparent centre of mass in this complex plane can be found. For an arbitrarily chosen transformation frequency, the centre of mass is typically close to zero (Fig. 3.8 left). However, when the introduced frequency reaches the frequency of the non-transformed signal with respect to the non-transformed coordinate, it deviates from zero (Fig. 3.8 right). The Fourier transform is this deviation of the centre of mass as a function of the transformation frequency, meaning a peak in this function represents a frequency which is present in the original signal. Additionally, when the signal is not centred around zero, initial peaks may appear before the signal stabilises (Fig. 3.9).
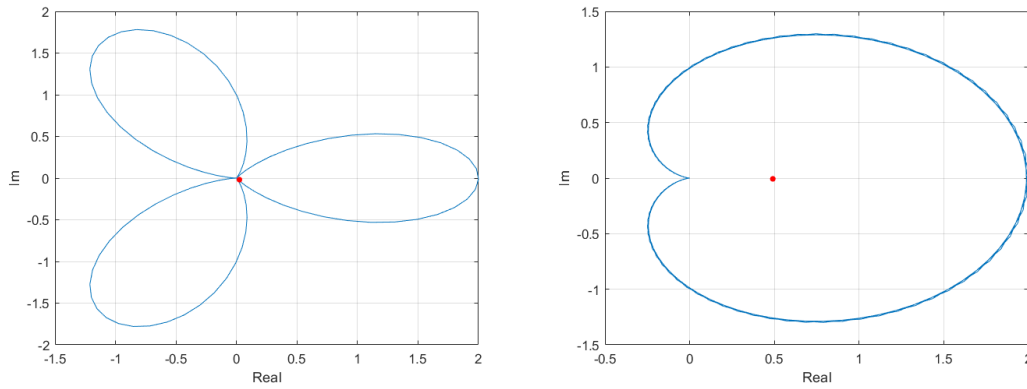
Figure 3.8: Rotating signal of $\cos(6\pi \cdot t) + 1$ at rotating frequency at 1 Hz (left) and at 3 Hz (right)
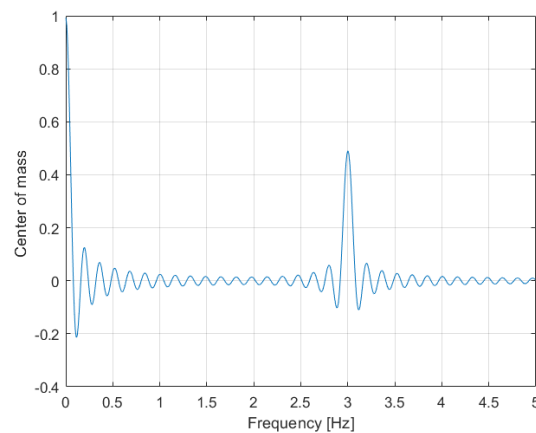

Figure 3.9: Real part center of mass as function of rotating frequency

The above description implicitly assumes a continuous function. However, a discrete formulation of the Fourier transform can also be used. In such a case, a summation is evaluated rather than an integral. The amount of frequency components that can be evaluated depends on the sampling frequency and the number of sampling points. This reinforces the idea that DIC requires a minimum ZOI size for evaluation if this concept is used. A problem that arises is that frequency components appear twice, once as their real one and once as a higher-order frequency. In addition, both components appear with half of the actual magnitude. However, this can easily be solved by eliminating all components above the Nyquist limit, which is the sampling frequency divided by two, and doubling all magnitudes below this limit. These magnitudes can then be normalised by the number of sampling points. In the applications of the DFT in DIC, the inverse of the Fourier transform is always taken afterwards, meaning no correction is needed. Various algorithms have been developed to more efficiently calculate the DFT to improve computational speed. The most widely used method is the Fast Fourier Transform (FFT), which reduces the complexity of computing the DFT from $O(N^2)$ to $O(N\log N)$ by factorizing the DFT matrix into a product of sparse factors (Van Loan, 1992).

When comparing two images, the pixels in the images may not line up precisely with each other. This can lead to errors in the measurements of displacement and deformation. Subpixel interpolation allows for matching of the grey scales inbetween pixels, leading to a more precise displacement measurement.

One way to perform subpixel interpolation is by using the fast Fourier transform (FFT) (Besnard et al. 2006). As mentioned earlier, the FFT decomposes a signal into its constituent frequencies. By applying the FFT to a grid of pixels in an image, we can obtain the decomposition of the image into a series of sines and cosines. This allows us to accurately represent the positions of the pixels in the spectral domain, which can then be translated without losing precision. The inverse Fourier transform can then be used to transform the modified spectral representation back into the spatial domain, resulting in a new image with interpolated values.

The formulation for the translation is given below (Bracewell & Bracewell, 1986). In which the ω represents the frequency and k is the subpixel displacement.

$$x(n-k) \overset{\text{FT}}{\longleftrightarrow} e^{-j\omega k} X(\omega) \tag{3.15}$$

In the quadratic difference formulation, it is also required to calculate the gradient of the reference image. This can be solved by using the differential property of the Fourier transform in the spectral domain (Bracewell & Bracewell, 1986).

$$\frac{d}{dt}x(t) \overset{\text{FT}}{\longleftrightarrow} j\omega \cdot X(\omega) \tag{3.16}$$

3.3.4. Multi-scale procedure

The implementation of Besnard et al. 2006 makes use of a multi-scale procedure. This approach is used because the derivatives require the displacement to be relatively small in comparison to the ZOI size. The idea, therefore is to start at a coarser scale with so-called super-pixels. The grey levels of the pixels contained in each super-pixel are averaged in order to obtain a single super-pixel value. These super-pixels are a size 2^n longer and wider. This means that when the ZOI is consists out of 16 by 16 pixels square, it covers a significantly larger area. Following, the displacements are calculated for this coarser image. Afterwards, the resolution is increased with the previously determined displacements already taken into account.

Within this iteration procedure, another iteration procedure is implemented. This convergence procedure determines the displacements within a certain resolution scale. In order to reduce computation time, an initial mean displacement guess is made. This can be done computationally fast by exploiting an additional Fourier transform property. This is done by maximising the cross-correlation function for each pixel of the ROI in the spectral domain (Hild et al. 2002; Lewis, 2001). The formulation of the cross-correlation in the spectral domain follows from Bracewell and Bracewell, 1986, in which the bar represents the complex conjugate, the capitals the Fourier transform and $\mathscr{F}$ the Fourier transform operator.

$$f \star g = \mathscr{F}[\bar{F}(v)G(v)] \tag{3.17}$$

In each iteration, the deformed image g(x) is updated with the previously calculated displacement. The iteration process is continued until the displacement changes by less than a predetermined threshold. These convergence steps are necessary because the sub-pixel interpolation relies on the results of the previous iteration. For instance, consider a pixel cluster that is believed to have moved one and a half pixels. In the next iteration, sub-pixel interpolation is used to estimate the grey level of the image at the half-pixel displacement. If the estimated grey level does not perfectly match the actual value, the displacement may need to be slightly adjusted in order to achieve the best fit.

3.3.5. Edge blurring

Images have a finite domain represented by the number of pixels. However, when the image is transformed into the spectral domain using a Fourier transformation, it is represented as a combination of sines and cosines with an infinite domain. This can cause issues at the edges of the image because the Fourier transform assumes that the image repeats infinitely in all directions. When the opposite edges of the image do not match, the Fourier transform tries to align them by introducing oscillations near the edges. To address this issue, several methods can be used. In the method of Besnard et al. 2006 the pixel values of opposite edges are averaged in order to prevent large discontinuities. In addition, each element is enlarged to a size that is an integer power of two, including a frame around each element. The enlarged element is used for determining the subpixel interpolation and the gradient calculations. Because these are the processes in which the Fast Fourier Transform (FFT) was applied. After these calculations, the original element is cut out of the enlarged zone again, removing the region where the most significant edge effects occur altogether.

Alternative methods to limit these effects could also be used. For example windowing, (Hild et al. 2002) which is the process of selecting a selected part of the grey scale range and stretching that range two cover the entire available range. In this way, extremes should be windowed out, resulting in less excessive fluctuations.

Another possibility is neutral padding (Bergonnier et al. 2007). In this process, the image is embedded in a larger frame. The difference between the two is the domain which is used to implement the periodicity. In order not to introduce additional information that may perturb the image, the high-frequency components in Fourier space are set to zero. The number of modes is chosen to be equal to the difference in the size of the

frame and original image in order to have a uniquely defined problem. The solution to this problem can be formulated as a linear system. However, due to it being partly formulated in real space and partly in Fourier space, an exact solution is difficult to obtain. Instead, approximate solutions can be found with an iterative scheme.

Alternatively, a symmetrization procedure can be used (Volkov et al. 2002). This method extends the image also beyond its original borders. It does this in a symmetrical way which satisfies the transport of intensity equation. An even symmetric extension of the original image proved to suffice and be the most effective (Volkov et al. 2002).
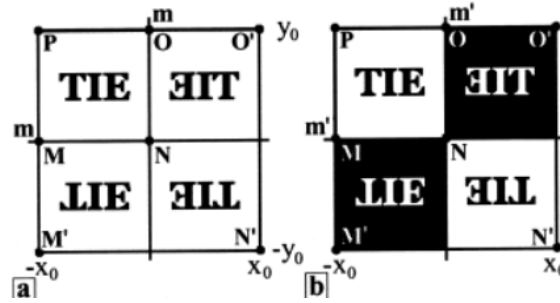

Figure 3.10: Even (a) and odd (b) symmetrization (Volkov et al. 2002)

Lastly, there is also the possibility of linear trend removal (Ravandi & Toriumi, 1995). In this procedure, linear trends over the whole domain are removed from the data, which can be induced in the correlation procedure. Edge blurring is, however, easily implemented and robust (Besnard et al. 2006).

3.3.6. Strain fields

From the obtained displacement field, a strain field can be calculated. The strain field is of importance because it is required in order to determine the SIF. There are different methods for obtaining the strain values.

One such method is Infinitesimal strain. Infinitesimal normal strains are simply defined by the gradients of the displacement into their respective direction.

$$\epsilon_{xx} = \frac{\partial u}{\partial x} \quad , \quad \epsilon_{yy} = \frac{\partial v}{\partial y} \quad , \quad \epsilon_{zz} = \frac{\partial w}{\partial z} \tag{3.18}$$

Shear strains can be obtained by taking the gradients with respect to the displacements orthogonal direction, as can be seen in the formulations below.

$$\epsilon_{xy} = \epsilon_{yx} = \frac{1}{2}(\frac{\partial u}{\partial y} + \frac{\partial v}{\partial x}) \quad , \quad \epsilon_{yz} = \epsilon_{zy} = \frac{1}{2}(\frac{\partial v}{\partial z} + \frac{\partial w}{\partial y}) \quad , \quad \epsilon_{zx} = \epsilon_{xz} = \frac{1}{2}(\frac{\partial w}{\partial x} + \frac{\partial u}{\partial z}) \tag{3.19}$$

However, this strain formulation only holds for relatively small strains. If it does not hold, the finite strains can be calculated. There exist multiple formulations for this: nominal, green-Lagrange and logarithmic strain (Hild & Roux, 2008).

If the strain can be considered small is mainly based upon two factors, namely the material elasticity and the deformation region (Oertel, 1996). Deformation in extremely elastic materials (e.g. rubbers) is generally too big to use the infinitesimal strain approximation. In metals, this is generally not the case; however, when plastic deformation occurs, the deformation could exceed the validity range. In fatigue crack growth, the plasticity area is of limited size in front of the crack tip, and the application of infinitesimal strains can be argued.

3.3.7. Implementation overview

In Fig. 3.11, a schematic overview of the implementation of Q4 DIC is given (Besnard et al. 2006). Only the main code to determine the displacements is shown. The pre-processing possibilities and visualisation possibilities are not shown. However, these steps take place respectively before and after the shown procedure. It is an iterative process with multiple layers. Each layer is represented by a colour, where the darkest is the highest iteration level. The white blocks represent the steps before and after iteration. The element iteration is repeated until all elements in the ROI are taken into account. On the contrary, the higher-level iteration schemes are performed until a specific condition is satisfied. The convergence criterion is embedded into the code, whilst the coarsening is defined as user input.
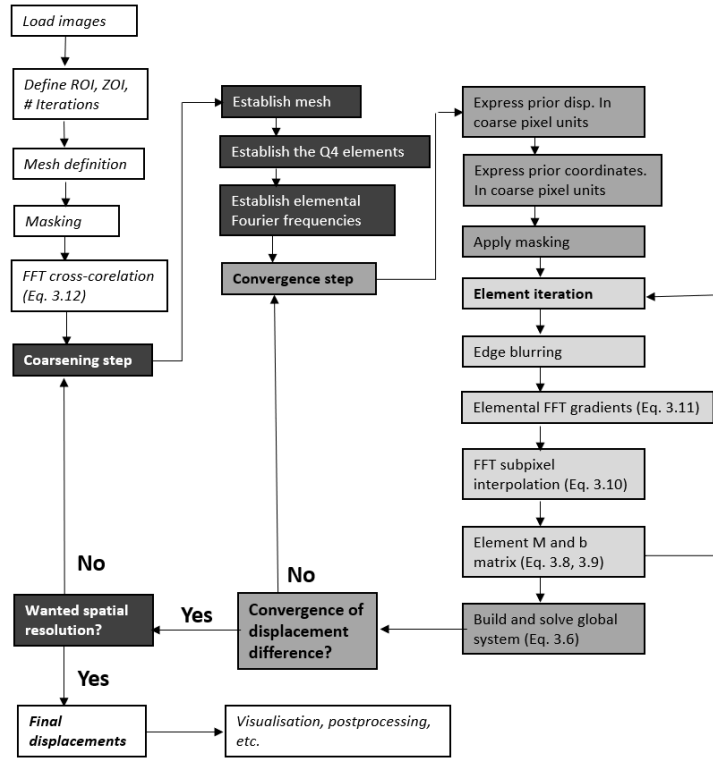
Figure 3.11: Q4P1 DIC code overview

3.4. Kinematic basis functions

In order to relate displacements or stresses over a domain, kinematic basis functions are required. Dependent on the DIC approach and the analysed situation, different kinematic base functions have to be assumed. The formulations can be divided into general polynomial formulations and special situation-dependent formulations.

3.4.1. General polynomial formulations

General polynomial formulations are common in most DIC procedures. These functions are not related to specific kinematics and therefore are applicable in a wide range of situations. However, these functions can not inherently be exactly matched to the evaluated displacement field. To address this limitation, a general polynomial function should be applied to a small domain where lower-order terms can accurately approximate the kinematics, or additional higher-order terms should be taken into account. However, due to the required size for accurate correlation, the reduction of element size is bounded. This introduces a trade-off between spatial resolution and accuracy of the displacement field. In the case of the subset-based DIC approach, the domain such a function should cover is the subset (ZOI). In this case, the functions are typically linear combinations of monomials (Eq. 3.20). The amplitudes corresponding to respective monomials can be physically interpreted as the local translation, rotation and strains dependent on their monomials order (Xu et al. 2015).

$$u(x, y) = C_0 + C_1 * x + C_2 * y + C_3 * x^2 + C_4 * x * y + ... \tag{3.20}$$

In finite element based DIC approaches, a Lagrangian basis is used (Eq. 3.21). These functions are one on their corresponding node and zero at all other nodes of the element. Analogous to FEM, the possible order of the shape functions is dependent on the chosen element type (Zienkiewicz & Taylor, 2000) because the number of nodes determines the possible order of the shape functions. Commonly used in DIC are cubic spline (Eq. 3.23) and linear functions (Eq. 3.22). These functions describe the shape function corresponding to node (j,k). The elemental displacement description (Eq.3.9) is constructed by summing the shape functions with their respective amplitudes. In order to ensure the Lagrangian properties, elements used with these formulations are generally normalised such that the elements x and y coordinates are in the [0,1] domain. In the case of Q4P1 elements (Besnard et al. 2006), this results in a relatively simple linear description (Eq. 3.24).

$$\mathscr{L}_{n,j}(x) = \prod_{i=0, i \neq j}^{n} \frac{x - x_i}{x_j - x_i} \tag{3.21}$$

$$\mathscr{L}_{1,j,k}(x,y) = \prod_{i=0, i \neq j}^{1} \frac{x - x_i}{x_j - x_i} \cdot \prod_{q=0, q \neq k}^{1} \frac{y - y_q}{y_k - y_q} \tag{3.22}$$

$$\mathscr{L}_{3,j,k}(x,y) = \prod_{i=0, i \neq j}^{3} \frac{x - x_i}{x_j - x_i} \cdot \prod_{q=0, q \neq k}^{3} \frac{y - y_q}{y_k - y_q} \tag{3.23}$$

$$u(x,y) = C_1 * (1 - x) + C_2 * (1 - y) + C_3 * x(1 - y) + C_4 * (1 - x)y \tag{3.24}$$

3.4.2. Special formulations

Instead of a generally applicable kinematic basis, the analytical formulation of the actual kinematics can be used as well. These types of special formulations are case-dependent, as geometry and loading affect the stress and displacement field. The displacement functions are mainly derived from the airy stress functions on a case-by-case basis. These types of functions are defined over the whole region of interest and can therefore be effectively used in global approaches. In simple cases, the stress distribution is often merely a combination of a membrane and a bending component. Therefore, a linear airy function can often be assumed (Eq. 3.26).

$$\varphi = C_{22} y^2 + C_{33} y^3 \tag{3.25}$$

$$\sigma_{xx} = \frac{\partial^2 \varphi}{\partial y^2} = 2C_{22} + 6C_{33} y \tag{3.26}$$

$$\sigma_{yy} = \frac{\partial^2 \varphi}{\partial x^2} = 0 \tag{3.27}$$

$$\sigma_{xy} = -\frac{\partial^2 \varphi}{\partial y^2} = 0 \tag{3.28}$$

Because DIC is a surface measurement tool, a plane stress condition can be assumed for the observed field. In order to map the stress function onto the displacements, the stress-strain relation needs to be established. Using Hooke's law leads to the following stress-strain relation.

$$\epsilon_{xx} = \frac{(\kappa + 1)\sigma_{xx} - (3 - \kappa)\sigma_{yy}}{8G} = \frac{(\kappa + 1)(6C_{33} y + 2C_{22}}{8G} \tag{3.29}$$

$$\epsilon_{yy} = -\frac{(\kappa + 1)\sigma_{yy} - (3 - \kappa)\sigma_{xx}}{8G} = -\frac{(3 - \kappa)(6C_{33} y + 2C_{22}}{8G} \tag{3.30}$$

$$\epsilon_{xy} = \frac{\sigma_x y}{2G} = 0 \tag{3.31}$$

$$\kappa = \frac{3 - \nu}{1 + \nu} \quad \text{Kolosov's constant} \tag{3.32}$$

Following the stress-strain relation, the strains can be related to the displacement. As discussed in section 3.3.6, the use of infinitesimal strain is not necessarily valid. However, plasticity should not be reached in the far-field region, meaning the small strain approach can be used. By making use of these relations, the final displacement description can be reached.

$$\mathbf{u}(z) = u_x + i \cdot u_y \tag{3.33}$$
$$= \sum_k C_k \Psi_k$$
$$= C_x + C_y \cdot i + C_r \cdot (ix - y) +$$
$$\frac{C_{22}}{G} \cdot \frac{2(\kappa + 1)x - 2(3 - \kappa)iy}{8} +$$
$$\frac{C_{33}}{G} \cdot \frac{-3(\kappa + 1)ix^2 + 6(\kappa + 1)xy - 3(3 - \kappa)iy^2}{8}$$

In the case of fatigue assessment, situations with a more complex stress distribution are of more interest for analysis. In case of a sharp notch, the Williams (Williams, 1952) V-shaped notch stress should be included. In addition, terms of the general Michell solution in Polar coordinates (Barber & Klarbring, 2003) can be added to include the weld load carrying stress (den Besten, 2015).

$$\varphi = r^{\lambda+1} \cdot [C_1 \cos((\lambda+1)\theta) + C_2 \cos((\lambda-1)\theta) + \tag{3.34}$$
$$C_3 \sin((\lambda+1)\theta) + C_4 \sin((\lambda-1)\theta)] +$$
$$A_{11} r^3 \cos(\theta) + B_{22} r^3 \sin(\theta)$$

Assuming linear elasticity, the displacement description can be derived in a similar manner as the linear airy stress function. The resulting description is written as a complex function in polar coordinates with eigenvalues λ_s and λ_a and their coefficients χ_s, χ_a. These eigenvalues correspond to the non-trivial solution of the eigenvalue problems for the symmetric and anti-symmetric parts of the airy stress function when inserting the boundary conditions and are dependent on the half-notch angle α (den Besten, 2015).

$$\mathbf{u}(z) = C_x + C_y \cdot i + C_r \cdot i(r \cdot e^{i\theta}) + \tag{3.35}$$
$$(\frac{K_I^N}{G}) \cdot \frac{r^{\lambda_s}}{2(2\pi)^{1-\lambda_s} \lambda_s(\lambda_s+1)(\chi_s-1)} \cdot$$
$$(\chi_s \kappa \cdot e^{i\lambda_s \theta} - \chi_s \lambda_s \cdot e^{-i(\lambda_s-2)\theta} + (\lambda_s+1) \cdot e^{-i\lambda_s \theta}) +$$
$$(\frac{K_{II}^N}{G}) \cdot i \cdot \frac{r^{\lambda_a}}{2(2\pi)^{1-\lambda_a} \lambda_a(\chi_a(\lambda_a-1)-(\lambda_s+1))} \cdot$$
$$(\chi_a \kappa \cdot e^{i\lambda_a \theta} + \chi_a \lambda_a \cdot e^{-i(\lambda_a-2)\theta} - (\lambda_a+1) \cdot e^{-i\lambda_a \theta}) +$$
$$(\frac{A_{11}}{G}) \cdot \frac{\kappa \cdot e^{i2\theta} - 2}{2} \cdot r^2 + (\frac{B_{22}}{G}) \cdot i \cdot \frac{\kappa \cdot e^{-i2\theta} - 2}{2} \cdot r^2$$

Where κ is Kolosov's constant as defined in equation 3.32, as the plane stress assumption still holds. G is defined as the shear modulus and is in some literature written as the Lamé's modulus (μ) (Mathieu et al. 2012). Similarly, the relations for a blunt notch can be derived (den Besten, 2015). In this description, some additional parameters are introduced due to the origin location, as shown in Fig. 3.12.
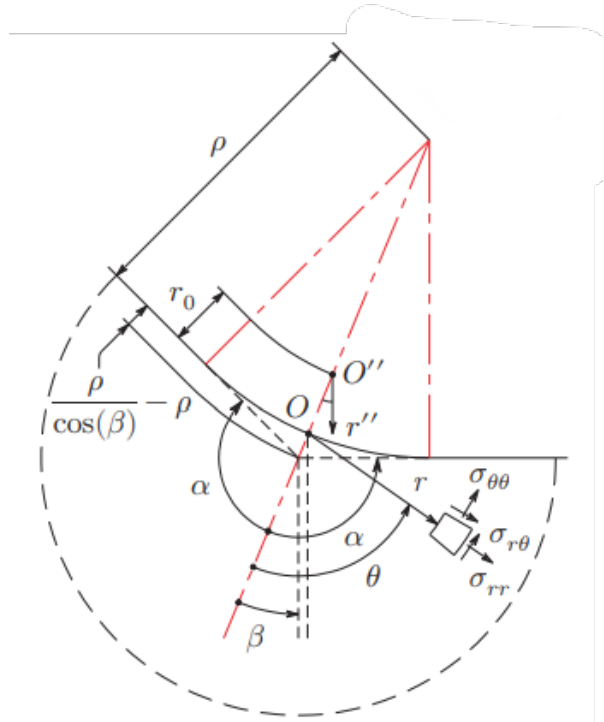

Figure 3.12: Blunt notch parameters (den Besten, 2015)

$$\mathbf{u}(z) = C_x + C_y \cdot i + C_r \cdot i (r'' \cdot e^{i\theta}) + \tag{3.36}$$

$$(\frac{K_I^N}{G}) \cdot \frac{1}{2(2\pi)^{1-\lambda_s} \lambda_s (\lambda_s + 1)(\chi_s - 1)} \cdot$$

$$((r'')^{\lambda_s} (\chi_s \kappa \cdot e^{i\lambda_s \theta} - \chi_s \lambda_s \cdot e^{-i(\lambda_s - 2)\theta} + (\lambda_s + 1) \cdot e^{-i\lambda_s \theta}) +$$

$$r_0^{\lambda_s - \zeta_s} \cdot \frac{\frac{2\alpha}{\pi}}{4(\frac{2\alpha}{\pi} - 1)} \cdot (\frac{\lambda_s}{\zeta_s}) \cdot$$

$$(r'')^{\zeta_s} (-\omega_{s2} \kappa \cdot e^{i\zeta_s \theta} + \omega_{s2} \zeta_s \cdot e^{-i(\zeta_s - 2)\theta} + \omega_{s1} \cdot e^{-i\zeta_s \theta})) +$$

$$(\frac{K_{II}^N}{G}) \cdot i \cdot \frac{1}{2(2\pi)^{1-\lambda_a} \lambda_a (\chi_a (\lambda_a - 1) - (\lambda_s + 1))} \cdot$$

$$i \cdot ((r'')^{\lambda_a} (\chi_a \kappa \cdot e^{i\lambda_a \theta} + \chi_a \lambda_a \cdot e^{-i(\lambda_a - 2)\theta} - (\lambda_a + 1) \cdot e^{-i\lambda_a \theta}) +$$

$$r_0^{\lambda_a - \zeta_a} \cdot \frac{1}{4(\zeta_a - 1)} \cdot (\frac{\lambda_a}{\zeta_a}) \cdot$$

$$(r'')^{\zeta_a} (-\omega_{a2} \kappa \cdot e^{i\zeta_a \theta} - \omega_{a2} \zeta_a \cdot e^{-i(\zeta_a - 2)\theta} - \omega_{a1} \cdot e^{-i\zeta_a \theta})) +$$

$$(\frac{A_{11}}{G}) \cdot \frac{\kappa \cdot e^{i2\theta} - 2}{2} \cdot r^2 + (\frac{B_{22}}{G}) \cdot i \cdot \frac{\kappa \cdot e^{-i2\theta} - 2}{2} \cdot r^2$$

If a crack is present, a stress distribution based upon an infinitely sharp v-notch can be adopted. This description can again be rewritten into a displacement field description with the use of the linear elasticity and small strain assumption. This results in the asymptotic Williams series solution (Williams, 1957), a sharp crack formulation. Assuming an initial crack size always exists, as is the case in arc welded joints, the description can already be used for pictures with no visible crack formation. This description can be formulated as a truncated series in complex coordinates. (den Besten, 2015; Mathieu et al. 2012; Roux & Hild, 2006).

$$\mathbf{u}(z) = \sum_n [\omega_n \mathbf{\Omega}_n(z) + \upsilon_n \mathbf{\Upsilon}_n(z)] \tag{3.37}$$

$$\mathbf{\Omega}_n(z) = \frac{(-1)^{(1-n)/2}}{2G\sqrt{2\pi}} r^{n/2} [\kappa e^{\frac{in\theta}{2}} - \frac{n}{2} e^{\frac{i(4-n)\theta}{2}} \tag{3.38}$$

$$+ ((-1)^n + \frac{n}{2}) e^{-\frac{in\theta}{2}}]$$

$$\mathbf{\Upsilon}_n(z) = \frac{i(-1)^{(1-n)/2}}{2G\sqrt{2\pi}} r^{n/2} [\kappa e^{\frac{in\theta}{2}} + \frac{n}{2} e^{\frac{i(4-n)\theta}{2}} \tag{3.39}$$

$$+ ((-1)^n - \frac{n}{2}) e^{-\frac{in\theta}{2}}]$$

3.5. Two-step approach

The described kinematic basis function can be incorporated into DIC in different ways. In standard DIC procedures, this is commonly done in the form of a two-step procedure (den Besten, 2015; Roux & Hild, 2006). In such a procedure, a simple and robust basis is incorporated in the determination of the displacements. This allows for a situation-independent procedure that can be commercially distributed and allows for use without a deeper understanding of the underlying DIC procedure. However, these procedures do not directly provide stress field related information. In order to obtain these, a situation-specific procedure has to be adopted. The general idea is to map one of the earlier described special basis on the obtained displacements. This can be implemented in the form of minimising the squared difference in order to obtain the amplitudes of the special kinematic basis.

3.6. One-step approach

In contrast with the two-step procedure, it is also possible to immediately incorporate special basis functions in the DIC procedure. This would remove the extra assumption layer, which should improve the accuracy, especially in the crack tip region due to the discontinuities. In addition, it would also remove the need for

the post-processing step, as the fatigue relevant parameters would be a direct result of the DIC (Vargas et al. 2016). Intuitively, it also seems to be removing a redundant step in the procedure, as now a displacement basis is assumed only once. However, because of the case dependency of the different functions, it is not logical to implement commercially, and for individual use, it requires a deeper understanding of the procedure to implement.

3.7. Alternative approaches

Alternative DIC procedures and alternatives to DIC altogether have also been developed, for example, calculating the strains with reverse optical flow and obtaining 3D displacement fields in this way (El-Awady et al. 2023). The benefit of such methods is that it is completely non-invasive and three-dimensional. However, fatigue specimens are for one-time use, and the application of the speckle pattern does not alter the results. Therefore, being slightly invasive is not a concern. In some instances, the extra dimension could be used to investigate out-of-plane behaviour as occurs in mode three crack surface displacement. Another more common method for obtaining an additional dimension in a 3D image is, as mentioned in the previous section, through the use of a stereo setup (Luo et al. 1993).

Other alternatives to DIC are neural networks and FEM-based solutions. While neural networks can be trained to determine crack locations and stress intensity factors (Chen & Liu, 2022; Long et al. 2021), checking the reliability of their outcomes and the training of the model can only be performed by using DIC or another evaluation method. This makes neural networks a "black box" whose underlying physics is not interpretable, making them less useful for research purposes. Instead, their main application lies in the industry (Long et al. 2021), where they may be used as a continuous monitoring method. It is worth noting that, at its core, this method is still an image correlation procedure, with the correlation algorithm incorporated into the neural network.

Finite element methods (FEM) (Elguedj et al. 2018; Zi & Belytschko, 2003) and boundary element methods (BEM) (Cisilino & Aliabadi, 1997) are numerical techniques that can be used to model the fracture process and compare the results with experimental data. However, these methods are numerical models and do not directly incorporate experimental data, requiring validation through experiments. As such, digital image correlation (DIC), which makes use of experimental data, is the preferred approach.

4. Texture quality

As discussed in Chapter 3, it is imperative that the images subjected to Digital Image Correlation (DIC) have a finely detailed, random pattern and are adequately illuminated. In this chapter, the required pre-processing steps are presented to assess image quality and determine specific parameters (the ZOI/subset size). This pre-processing mitigates a potential reduction in the precision and accuracy of the following DIC analysis.

First, in order to evaluate the quality of the pictures, some texture analysis can be performed. A greyscale histogram can point out image saturation problems. It is preferable to have a wide grey scale range, which is in line with the ability of the used camera (Besnard et al. 2006).
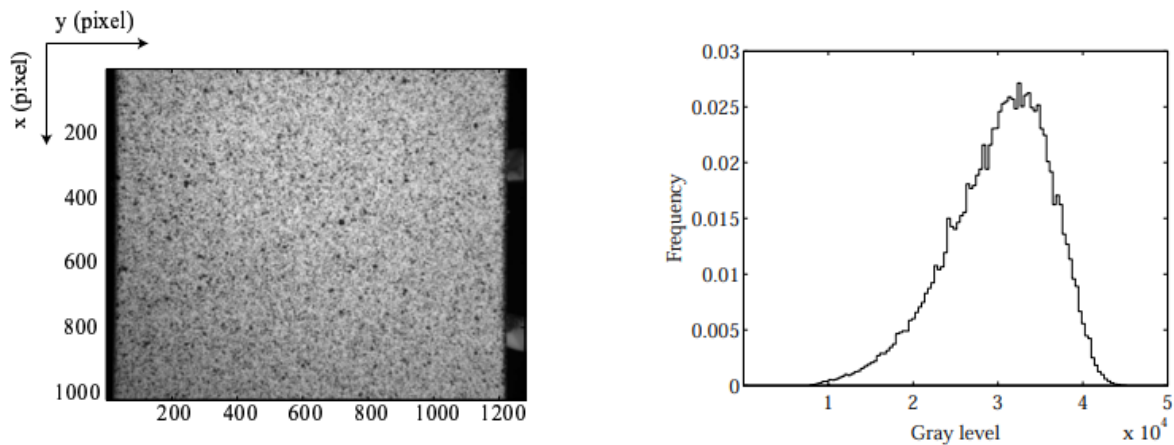

Figure 4.1: Typical speckle pattern and grey level distribution (Besnard et al. 2006)

Because of the random pattern, the greyscale distribution for each subset or element will be unique. In order to determine if there are enough gradients to accurately determine the displacements, the grey scale fluctuations can be evaluated. Each ZOI is characterised by the standard deviation of its own grey level. Following, this value is averaged over all ZOIs and normalised by the maximum grey level of the image. The obtained value should be greater than 1% of the total grey scale. Instead of evaluating the mean of all ZOIs, it is also possible to evaluate the minimum. Comparing different ZOI sizes gives a first indication of its required size. In Fig. 4.2, it can be seen that the mean fluctuations satisfy this criterion for every size. However, the ZOI size needs to be at least 16 in order to suffice for every single ZOI.
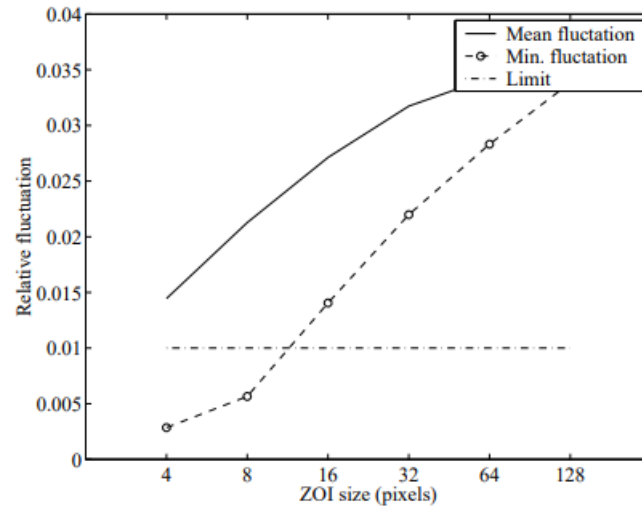
Figure 4.2: Typical Minimum and mean relative RMS fluctuations as functions of the element size (Besnard et al. 2006)

The correlation radii of the image texture are another important feature that can be used to evaluate the quality of an image for use in DIC. These radii provide information about the isotropy and size of the texture, which can be used to determine whether small-scale details in the image are likely to be accurately captured by the DIC process. It is generally desirable for the correlation radii to be as small as possible, as this can help to ensure that the texture's grey level distribution is unique and well-defined. As a practical guideline, the correlation radii should be no more than 25% of the subset size in order to achieve good results (Besnard et al. 2006).

To estimate the correlation radii, a parabolic interpolation of the image's auto-correlation function can be performed at the centre of the subset, taking into account only the eight neighbouring pixels (den Besten, 2015). This process results in the correlation radii being the principal axis lengths of an ellipse in the (x,y) direction of the autocorrelation. The ratio of the two correlation radii values can be used as a measure of the texture's anisotropy. In Fig. 4.3, it can be seen that the correlation radii are only small enough for a subset size of 21 pixels or larger.
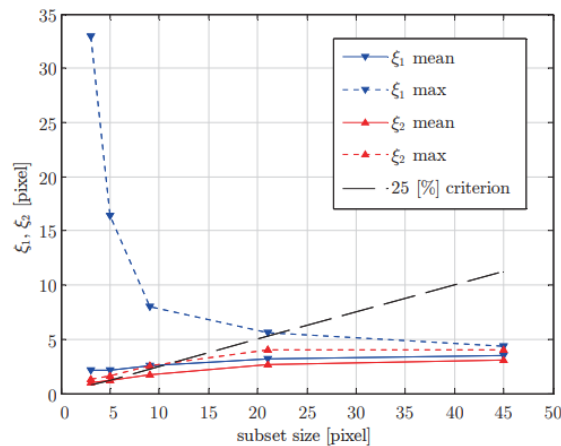

Figure 4.3: typical correlation radii (den Besten, 2015)

5. Far field region analysis

For a full fatigue analysis, both the fatigue-sensitive location and the far field region need to be taken into account. The far-field stress distribution is required in order to obtain the SIF-related far-field information (σ_s, r_l, r_s). In standard DIC procedures, this is commonly done in the form of a two-step approach (den Besten, 2015; Roux & Hild, 2006). However, a one-step approach has also been developed (Vargas et al. 2016). In this chapter, the far-field analysis with a general kinematic basis and a special basis assumption will be discussed.

5.1. General basis

In a two-step procedure, the analysis starts with a general basis. The far-field region is not directly affected by the notch-induced stress concentration. Therefore, cracks will generally not form in this region, and no stress singularities or displacement jumps will occur. For this reason, a subset-based or FEM-based DIC procedure can be used without additional problems. These procedures make use of general polynomial basis functions (3.4.1), leading to a discrete displacement field. With a small strain assumption and Hooke's law, a discrete stress field can be obtained. However, for further analysis, global stress field parameters are required, which require a continuous stress field description.

5.2. Special basis

If a general basis has been used, further steps have to be taken in order to obtain the stress distribution. Through the mapping of an appropriate special base function (Eq. 3.33) on the earlier obtained displacements, a continuous stress field description can be obtained. The unknowns in such a procedure are the coefficients of the special basis functions. The coefficients can be obtained by minimising the squared difference between the two displacement descriptions(Roux & Hild, 2006), where N is the amount of measured displacement points.

$$\sum_{i=1}^{N} ||u(z) - \sum_k C_k \Psi_k||^2 \tag{5.1}$$

This minimisation can be converted to solving a linear system. However, due to the proprieties of the displacement function, an inverse can not be calculated. Therefore, the linear system resulting in the stress distribution includes the pseudo inverse (den Besten, 2015). Resulting in a formulation to determine the most likely coefficient matrix.

$$\mathbf{C} = \mathbf{\Psi}_{\text{pseudo}}^{-1} \mathbf{u}(z) \tag{5.2}$$

In Fig. 5.1, a typical displacement field before and after post-processing can be seen. The shown displacements are in the x direction and are given in the unit of pixels.
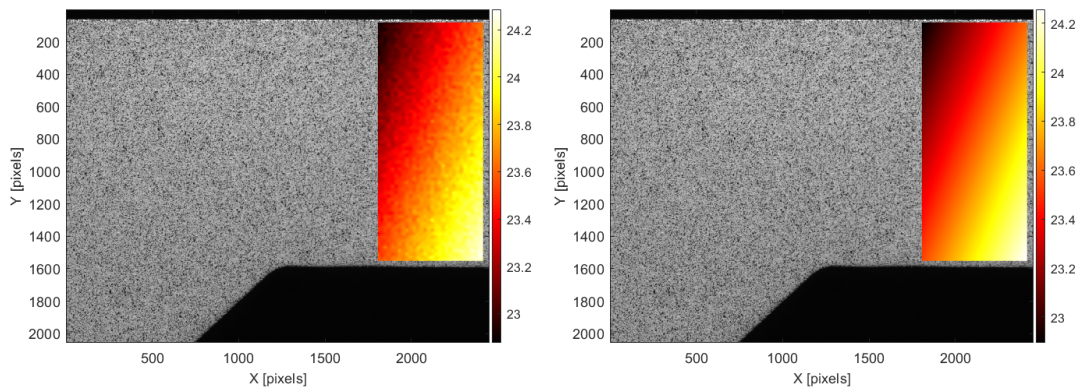

Figure 5.1: typical far field displacement field in x direction. Obtained directly from DIC (left) and after post-processing (right)

The coefficients of the displacement field directly relate to coefficients in the stress field due to the derivation of these fields. Obtaining the relevant far-field parameters.

The far-field stress distribution can also be directly integrated into the DIC procedure, resulting in a one-step procedure. Firstly, the five terms of the displacement basis corresponding to the linear stress distribution can be mapped on the region of interest. This can be done by defining each term over the entire ROI. Following, each can be assigned an amplitude operator for which the correlation criteria can be solved by the same general procedure as in a two-step approach. From this result, five amplitudes, of which two directly correspond to the stress distribution coefficients.

6. Notch region analysis

The notch region is of the upmost importance for fatigue analysis, as a notch introduces a macro stress concentration making it a fatigue hot spot. The stress distribution in this region is more complicated when compared to the far-field, meaning a linear stress distribution can no longer be assumed. In addition, the stress concentration means that cracks can start to form at these locations, which alters the stress distribution in their own respect. Similar to the far field region, the analysis can be performed in the form of a two- or a one-step approach. In this chapter, it will be discussed how to obtain the crack tip location and the relevant stress field parameters in case of a general basis and special basis assumption.

6.1. General basis

The first step in a two-step approach for analysing the notch region using DIC is similar to the equivalent step in far-field region analysis. A general polynomial basis is used in a subset or FEM-based DIC approach in order to measure the deformation and strain fields.

6.1.1. Crack effects

However, one of the primary challenges of FEM-based DIC in the presence of cracks is the enforcement of displacement continuity over the Region of Interest (ROI). The displacement continuity assumption is violated when a crack forms in the ROI, resulting in a displacement jump over the crack flanks. Because of the enforced continuity, the displacement is averaged over the crack region. This inconsistency can lead to inaccuracies in the measured displacement fields and, therefore, in the resulting strain and stress fields (Yang & Bhattacharya, 2019).

To overcome these challenges, various techniques have been proposed, such as masking of the direct crack region, crack-tip enrichment, and special kinematic basis (Mathieu et al. 2012). The masking technique involves manually disconnecting the elements in the direct crack region, which can effectively account for the discontinuity in displacement due to crack formation. The crack-tip enrichment method involves using specialized enrichment functions to model the crack-tip region (Roux-Langlois et al. 2015), improving the accuracy of the strain fields. The special kinematic basis is a theoretical framework that can model complex deformation fields, including those present in the notch region, and provide more accurate strain measurements.

6.1.2. SIF calculation

After displacements have been determined on a general basis, further calculations are required in order to obtain the relevant stress field information. There exist three main possibilities, of which two are also used in FEM-based procedures.

The first of these approaches requires a special type of mesh. The solid near the crack tip must be meshed with quadratic elements (eight-noded quadrilaterals or six-noded triangles). The elements connected to the crack tip must be quadrilateral. One side of each element connected to the crack tip is collapsed to make the three nodes on the side coincident. The mid-side nodes on the elements connected to the crack tip are shifted to one-quarter point positions. If the coincident nodes are permitted to move independently, an r^{-1} singularity in strain is produced, which is required to prescribe the crack tip plasticity. The obtained stress can then be used in the SIF formulation (Bower, 2009).
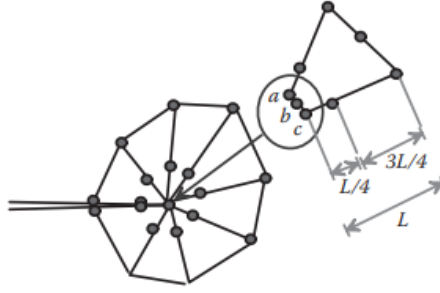
Figure 6.1: Element mesh near a crack tip (Bower, 2009)

$$K_I = \lim_{x \to 0} \sqrt{2\pi r}\, \sigma_{\theta\theta}(r, \theta = 0) \tag{6.1}$$

Alternatively, the energy release rate can be used to calculate the SIF (Bower, 2009). This procedure has the advantage that it is an path independent contour integral and therefore does not require information directly at the crack tip. Instead, more accurate stresses farther away can be used.

$$K_I = \sqrt{\frac{GE}{1 - v^2}} \tag{6.2}$$

$$G = \int_{\Gamma} (W \delta_{j1} - \sigma_{ij} \frac{\partial u_i}{\partial x_1}) m_j \, ds \tag{6.3}$$

In the formulation of the release energy, W is the strain energy density, σ_{ij} is the stress field, u_i is the displacement field, m_i is a unit vector normal to Γ, and the e_1 basis vector is parallel to the direction of crack propagation. In the case of an elastic material in a quasi-static loading condition, G reduces to Rice's J Integral (Rice, 1968).
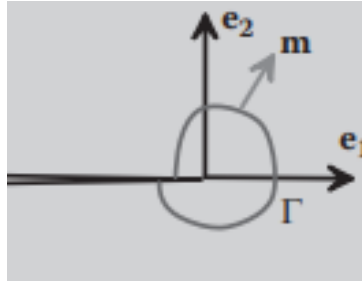

Figure 6.2: Element mesh near a crack tip (Bower, 2009)

The last procedure makes use of a special basis to map the displacements on. A relevant kinematic field is mapped on the obtained displacement to get a full field description. This procedure is similar to the far field analysis (Eq. 5.1), but a different basis has to be assumed. In case no crack has formed, different functions can be chosen based on blunt or sharp notch (Eq. 3.36, 3.35). (den Besten, 2015; Williams, 1952). Assuming a crack is present, a stress distribution based upon an infinitely sharp v-notch can be adopted (Williams, 1957). This results in the asymptotic truncated series solution (Eq. 3.37,3.38,3.39).

Different terms in the truncated Williams series have a different physical interpretations. Their corresponding amplitudes (ω_n, v_n) are the stress field related parameters sought for. The zero-order term corresponds to rigid body motions. The first-order term corresponds to the mode 1 and mode 2 SIF, and the second-order terms correspond to the T-stresses. Higher-order terms might also be included, but these have less of a direct physical interpretation. In addition, also negative values could be used as these so-called supersingular terms take non-linearities into account.

6.1.3. Crack tip location identification

When a general basis is used in the analysis, the crack tip region is still unknown. Similar to the SIF, it can be obtained by mapping a special basis on the obtained displacement field. The truncated Williams series has the crack tip defined as its origin. This means that when the crack tip location is not accurately assumed, the mapping will include a larger residual error. By mapping the special basis upon the obtained displacement field with different crack tip assumption, and comparing the global residual error the crack-tip location can be obtained (Fig. 6.3) (Roux & Hild, 2006).

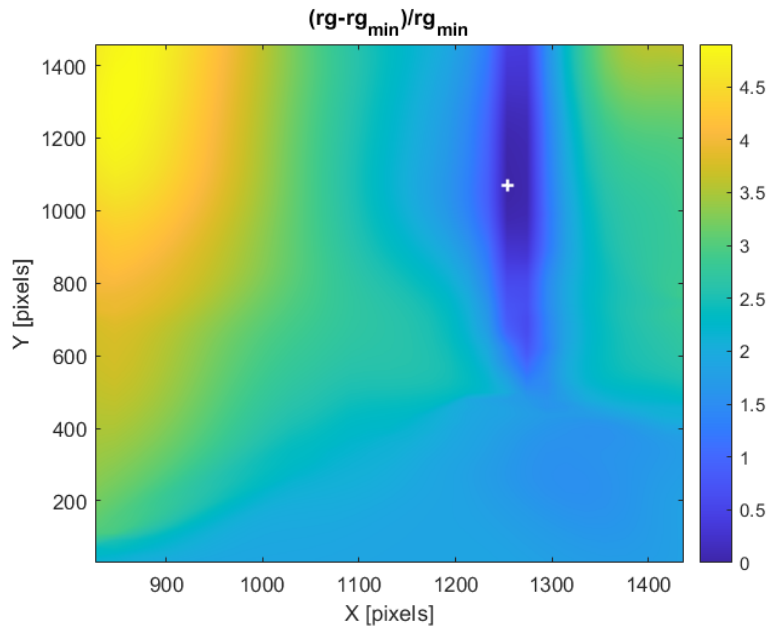$$r_g = \sum_i (u_i(z)_{DIC} - u_i(z)_{Subset})^2 \tag{6.4}$$

Figure 6.3: Relative residual error for different crack tip assumptions

6.2. Special basis

Similar to the far-field analysis, the special basis can be adopted in two different ways. First of all, it can be used to map the displacements on in the second step of a two-step approach. Alternatively, it can be directly implemented in the one-step DIC algorithm proposed by Vargas et al. 2016. This approach is an integration of the two steps of a FEM-based two-step procedure with mapping of a special basis on the displacements in post-processing.

6.2.1. Williams expansion

For evaluation of the notch region, the truncated asymptotic Williams solution (Eq.3.37, 3.38, 3.39) is recommended. The Williams stress field is a well-established analytical formulation for the stress field around a crack tip. The derived displacement field formulation (Williams asymptotic solution) can be used directly as the displacement field basis function. In the correlation procedure that follows, the sought for amplitudes become the stress field parameters instead of the nodal displacements. The different terms of the Williams series can be evaluated upon a mesh which can be refined to not have an effect on the outcome. Keeping such a mesh and dividing the ROI into different ZOIs allows for the use of the multi-scale implementation of Q4 DIC (Vargas et al. 2016).

An important factor in any approach, including the truncated Williams solution, is the number of terms that have to be taken into account. In order to capture the SIF, the first-order terms have to be taken into account. Additionally, supersingular fields ($n < 0$) can be taken into account to describe plastic behaviour near the crack tip (Roux et al. 2009). Taking the truncated terms from -3 has been shown to incorporate all the non-linear

behaviour around the crack tip (Henninger et al. 2010; Mathieu et al. 2012). In order to get a proper description, additional higher-order terms have to be included. For an elastoplastic material in the small-scale yielding regime it has been shown that truncating up until term 7 should suffice (Henninger et al. 2010). However, the considered terms are not orthogonal, meaning including more terms can affect the lower-order amplitudes. This can result in problems when looking for crack tip convergence based on these amplitudes (Section 6.2.3). Therefore, a comparative analysis with a different number of terms is recommended (Vargas et al. 2016). In such analysis, the grey scale level residual is an excellent method to see which basis describes the kinematics better. Additionally, one can look at the convergence of the parameters of interest when taking more terms into account. In Fig. 6.4, a typical displacement field before and after post-processing can be seen. The shown displacement is in the x direction and is given in pixels.
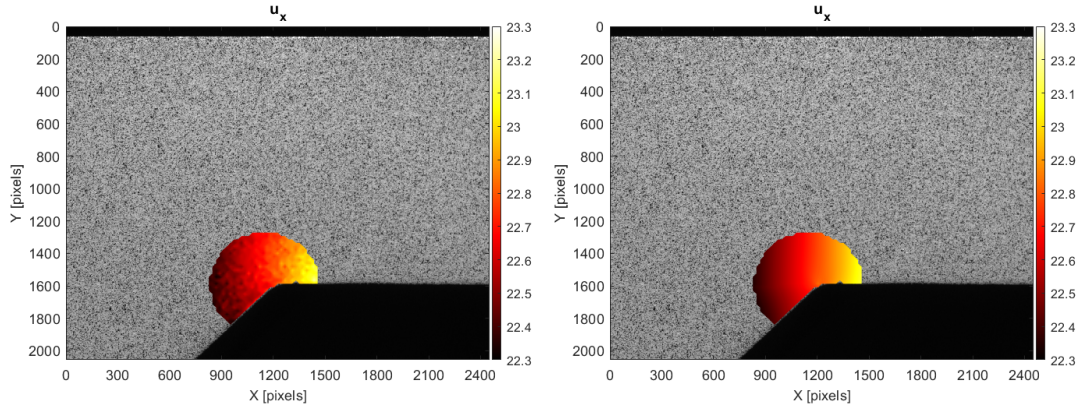

Figure 6.4: typical notch displacement field in x direction. Obtained directly from DIC (left) and after post-processing (right)

6.2.2. SIF calculation

As mentioned in section 6.1.2, the SIF correspond to the amplitudes of the first-order terms ($n = 1$) in the Williams solution. When a one-step special basis approach is used, no additional SIF calculation is required. Because the resulting amplitudes from the correlation procedure are the desired stress field parameters. However, two concerns should be taken into account, those are the shear modules and the units of the amplitudes. Because, the amplitudes can be defined as the stress field parameters divided by the shear modules. In order to determine the actual SIF of the stress field, these amplitudes should therefore be multiplied by the shear modules. Determination of the shear modulus can be done directly from the material properties or from the applied load and the obtained displacements in the far field region. With regard to the units, it is important to note the units used in the shape functions. Because the amplitudes are scaled in order to let these functions match the present displacement field.

6.2.3. Crack tip location identification

One of the main difficulties in the one-step procedure is that the Williams solution (Eq. 6.5,3.37) is defined with its origin at the crack tip. Therefore, the crack tip needs to be determined during the correlation procedure. The crack tip location can be obtained directly from the special basis formulation. Making use of a special property of the Williams solution (Eq. 6.6) in order to linearize the field with a small crack-tip misplacement (eq. 6.7), a relation between the amplitudes and the misplacement can be obtained (Eq. 6.8). Taking the fact that the first order singular term should be zero when no mispositioning is present a simple expression for the shift can be obtained (Eq. 6.9) (Roux et al. 2009).

$$u = \sum_{n,j} \omega_j^n \phi_j^n(z) \tag{6.5}$$

$$\frac{\partial \phi_j^n}{\partial x} = -\frac{n}{2} \cdot \phi_j^{n-2} \tag{6.6}$$

$$u(z+d) = \sum_{n,j} \tilde{\omega}_j^n \phi_j^n(z+d) \tag{6.7}$$

$$\omega_j^n = \tilde{\omega}_j^n - \frac{n+2}{2} \tilde{\omega}_j^{n+2} d \tag{6.8}$$

$$d = \frac{2\omega_{-1}}{\omega_1} \tag{6.9}$$

This method has the advantage of being less computationally demanding than the residual error method and providing an exact location. However, it assumes a straight crack tip path as only a mispositioning in a single direction is given in this method. This is not an issue for symmetric CT specimens with a groove because in, such cases, the crack is forced into a straight crack path. However, in the case of standard maritime joints (e.g. T joint), the crack does not necessarily propagate straight forward. However, an extension towards a description which also takes the crack-tip misplacement normal to the crack propagation is not trivial. The complication stems from the fact that a lower-order term does not simply define the derivative of the field in this direction. Because in contrast to when the derivative is taken along the crack growth direction (6.6), the angle is $\pi/2$ instead of zero, meaning various contributions do not cancel out in addition to the inherent differences following form deriving with respect to a different coordinate, making the special property not hold. Another issue is that this determination of the crack tip offsets requires the amplitudes, which can only be obtained when a crack tip location is assumed. Two different possible solutions for this problem have been proposed.

Firstly, a finite element based DIC method can be used in order to give an initial estimate of the crack tip location (Vargas et al. 2016). The integrated DIC will be employed with the estimated crack tip location as the origin for the Williams solution. From the first normal and the first supersingular term, the crack tip shift can then be calculated. With this shift, the crack tip location can be updated, and the integrated DIC can be used again with a new fixed origin. These steps can be repeated until the crack tip position has converged.

Another possibility is not employing the Finite element based DIC and taking the location of the uncracked notch as the initial crack tip estimate (Vargas et al. 2018). The advantage is that the finite element based assumptions are completely eliminated. However, at the long crack growth stage, it could result in additional computational time because of the larger location bridging the convergence procedure has to perform. Another problem could arise in the form of the Williams formulation not aligning at all due to a faulty initial location assumption.

For both methods, it is important that an appropriate masking is applied. Because near the crack tip, the elastic fields can not describe the non-linear behaviour that is occurring near the crack tip. Therefore, these regions need to be masked; however, the region should be small enough to let the supersingular fields correctly determine the crack tip location (Leplay et al. 2011; Réthoré et al. 2011). This procedure could be more difficult in the case of a not straight crack path as the approximate location can vary more widely.

7. Research overview

After the presented literature review, some conclusions can be drawn. in this chapter the previous findings will be combined to identify the research gap and formulate a hypothesis. Following the research to be conducted can be formulated, in the form of research questions and a research plan. Lastly, a indicative planning for this research will be given.

7.1. Research gap

Three research gaps in literature have been found:

(1) Concerning the total life concept there exists a clear gap in the validation of the model. The current potential drop measurements do not provide the full stress field related information, and more accurate crack tip localisation is aimed for.

(2) Furthermore, the advantage such model brings should be investigated. Comparing the model with the current industry standard, will provide valuable insights for possible application.

(3) Lastly, current DIC methods have shortcomings with respect to crack analysis. A one-step approach could provide a more accurate evaluation. However, such method as well as a way to construct such method is not widely available.

7.2. Research hypothesis

The main hypotheses can be stated as follows:

> **In order to improve the fatigue total life time estimate of arc-welded joints in steel marine structures, validation of the involved two-stage crack growth model requires a one-step DIC approach.**

7.3. Research questions

The main research question following from the research hypothesis is formulated as follows:

> **Can a two-stage crack growth model be used to improve the fatigue life time estimate of arc-welded joints in marine structures?**

To answer the research question the following six sub questions will be answered.

1. Can Airy stress functions be used in a one-step DIC approach to effectively capture the far field stress distribution?

2. Can the Williams displacement field solution be used in a one-step DIC procedure as a reduced kinematic basis for the notch region?

3. Does one-step DIC improve the crack tip estimate with respect to a two-step approach?

4. Can one-step DIC be effectively used to Validate a crack growth model?

5. Can the two stage crack growth model predict the life time behaviour of a hot spot in an actual vessel?

6. Can the two stage crack growth model improve the prediction of the life time behaviour with respect to a classification rule based assessment?

7.4. Research plan

Answering the research question can also be formulated by actions that have to be performed. This results in the following three steps.

1. Establish a one-step DIC code based on Williams asymptotic solution.

2. Validate the total life concept established by Palkar.

3. Apply the model to a case study.

The research will be successful when a working integrated DIC code has been delivered, it has shown if the newly developed model can indeed accurately predict the two stage crack growth behaviour and the new model has been applied to a case study. In addition, it would be interesting if it can be judged how beneficial the model is compared to existing models.

II

Modelling

8. DIC developments

The first aim of the research is to explore dedicated displacement field formulations to capture the crack tip location and corresponding stress intensity factor simultaneously by developing a one-step DIC approach. This chapter discusses the development of a multi-scale global one-step DIC approach, starting from the framework of a two-step FEM-based approach. First, the findings concerning the two-step approach will be presented. Following the developments resulting in the global one-step DIC procedure will be presented, influenced by the concepts outlined in Roux and Hild, 2006. The developed procedures general framework remains equal to the two-step approach as outlined in Section 3.3.7. Whilst the general structure remains, notable distinctions arise in constructing the elemental matrix and incorporating constraints based on series analysis.

8.1. Local two-step FEM-based approach

In the context of employing a two-step DIC approach, the amplitudes of William's asymptotic solution can be calculated in the post-processing step using the pseudo inverse (Eq.5.2). However, This method introduces a problem when the amplitudes are used to determine the approximate crack-tip misalignment with the singular term method. The resulting amplitudes can be complex values with no straightforward decomposition, as the decomposition in a complex and real part based on the displacement direction only holds for the product of the amplitudes with their shape functions. This problem can be overcome by enforcing the amplitudes to be in the real domain. Considering these amplitudes should represent physical properties of the stress field as the stress intensity factors, it becomes imperative to enforce these values to be real. This enforcement can be obtained by employing a property of the complex conjugate (Eq 8.1) in the mapping procedure.

$$|z|^2 = z \cdot \bar{z} \tag{8.1}$$

$$\eta = |U - a\Psi|^2 = (U - a\Psi)(\bar{U} - a\bar{\Psi}) \tag{8.2}$$

$$\frac{d\eta}{da} = -\Psi^T \bar{U} + a\Psi^T \bar{\Psi} - \bar{\Psi}^T U + a\bar{\Psi}^T \Psi = 0 \tag{8.3}$$

The adjusted derivation results in the following linear system to be solved. In which both the a and b matrices are entirely defined with real entries.

$$Ma = b \tag{8.4}$$

$$M = \Psi^T \bar{\Psi} + \bar{\Psi}^T \Psi \tag{8.5}$$

$$b = \Psi^T \bar{U} + \bar{\Psi}^T U \tag{8.6}$$

The Stress intensity factors follow directly from the amplitudes of the Williams solution. However, during implementation, defining the amplitudes with the shear modulus included is often beneficial, meaning a multiplication with this value becomes necessary afterwards to obtain the SIF. Furthermore, When the displacement field is normalised or evaluated in pixel units, this has to be corrected, for in the case of the SIF, this correction is the square of the pixel size in mm or m, dependent on the units of choosing.

In the case of a rotated crack angle, the obtained displacement field from the first step should be angled before mapping the Williams solution on top of it. As in the Williams solution, the crack should be aligned with the negative real axis. In accordance, the x and y coordinates of the points on which the Williams functions are mapped are rotated. In which the x coordinate is chosen to correspond to the real axis. The radius and the angle are determined, as the Williams solution in polar coordinates is used.

$$r = \sqrt{x^2 + y^2} \tag{8.7}$$

$$\theta = \arctan \frac{X'}{Y'} \tag{8.8}$$

From there, the linear system can be solved by mapping the functions on the discrete displacement field. Afterwards, the obtained displacement field must be rotated back into the reference frame to obtain the

sought-for results. All rotations can be simply performed with the use of the rotation matrix, as can be seen with the counterclockwise rotation matrix in Eq. 8.9-8.10.

$$\begin{bmatrix} X' \\ Y' \end{bmatrix} = \begin{bmatrix} \sin\phi & \cos\phi \\ -\sin\phi & \cos\phi \end{bmatrix} \begin{bmatrix} X \\ Y \end{bmatrix} \tag{8.9}$$

$$\begin{bmatrix} U \\ V \end{bmatrix} = \begin{bmatrix} \sin-\phi & \cos-\phi \\ -\sin-\phi & \cos-\phi \end{bmatrix} \begin{bmatrix} U' \\ V' \end{bmatrix} \tag{8.10}$$

An additional noteworthy outcome from this alternative approach to setting up the linear system is the squareness in the M matrix of the linear system. Consequently, the solution of the system is not limited to the pseudo inverse; instead, the genuine inverse of the matrix can be used for its solution.
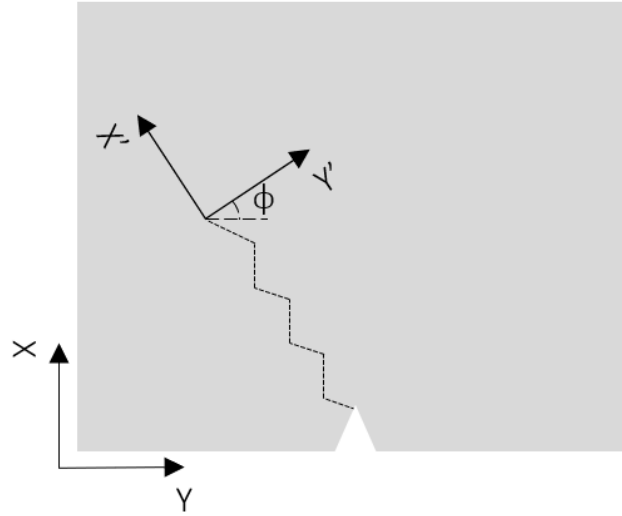

Figure 8.1: Crack orientated axis system

An advantage of employing the two-step approach is that by multiplying the obtained displacement field by the physical pixel size, the conversion into the desired units can be easily made without the need to consider the units of the amplitudes of the special basis on which the field is mapped.

Alternatively, in cases where the special basis is identified as the Williams series solution, the Stress Intensity factor's units correspond to the square root of the pixel number when the shear modulus is excluded from the basis functions. The obtained SIF value is multiplied by the shear modulus and the square root of the pixel size to convert the units to $MPa\sqrt{mm}$.

Of interest is quantifying the error to assess the performance and accuracy of the two-step DIC procedure. The grey-level residual provides a robust and straightforward error evaluation (Eq. 8.11). This error metric is easily obtained in the current procedure due to the iterative nature of the correlation procedure. Specifically, following each iteration, the deformed image is shifted. If this difference is extracted at the convergence of the correlation procedure, this provides the residual error. The camera's dynamic range can be used to normalise this error measurement to facilitate comparisons across experiments.

$$R(x) = |g(x + u(x)) - f(x)| \tag{8.11}$$

Of particular significance is the uncertainty surrounding the amplitudes of the displacement field. Once convergence is achieved, the anticipated outcome is a zero grey-level difference between the deformed and reference images. This residual can be used to calculate the displacement residual, of which the displacement variance follows as the mean of the squared local residuals. Notably, there is no requirement for a Bessel correction factor, as the error field serves as the encompassing population (Dekking et al. 2005).

When determining the resulting variance of the Williams amplitudes in the post-processing, a straightforward inclusion of the variance of the displacement residual into the formulation is inadequate. Instead, variance properties are required to determine the amplitude variance. Considering the variance of a function, which is a random variable (x) multiplied by a non-random constant (C). The resulting variance of the function is equal to the square of the constant, multiplied by the variance of the random variable (Eq. 8.12). This principle extends naturally to a matrix framework (Eq. 8.13), where A represents a non-random matrix, and X is a random vector.

$$Var(Cx) = C^2 \cdot Var(x) \tag{8.12}$$

$$Var(AX) = A(Var(X))A^T \tag{8.13}$$

However, incorporating these characteristics into the mapping process raises an issue due to the complex matrices. The complex conjugate squaring property (Eq. 8.1) is once more employed to address this challenge. This property can be used due to the variance's absolute nature, allowing the covariance matrix's derivation for the Williams amplitudes.

$$M\,a = b \tag{8.14}$$

$$Var(Ma) = M\,Var(a)\,M^T \tag{8.15}$$

$$Var(b) = \Psi^T\,Var(\bar{U})\,\bar{\Psi} + \bar{\Psi}\,Var(U)\,\Psi \tag{8.16}$$

$$Var(b) = (\Psi^T\,\bar{\Psi} + \bar{\Psi}^T\,\Psi)\,Var(U) = M\,Var(U) \tag{8.17}$$

$$Var(a) = (M^T)^{-1}M^{-1}M\,Var(U) = (M^T)^{-1}\,Var(U) \tag{8.18}$$

The diagonal of the resulting square covariance matrix provides the variance of the corresponding amplitude terms. The obtained amplitude variance can be scaled to the relevant SI units according to the variance properties (Eq. 8.12).

8.2. Global one-step approach

Analogous to the FEM-based DIC (Besnard et al. 2006) procedure, in the one-step DIC procedure, displacement estimation relies on utilising a first-order Taylor expansion. It is important to note that this approach is an approximation, taking into account local gradients. Consequently, a multi-scale algorithm is necessary to capture the overall displacements initially before refining them at a lower scale. Therefore, the overall structure of the DIC procedure can be similar to the FEM-based approach.

The general element structure is being kept for the gradient and subpixel procedure. However, a different method is used to ensure continuity. Rather than enforcing continuity through the element nodes, it is achieved by globally defining the shape functions. In this approach, for each designated element, only a portion of the shape function is considered by incorporating the element's global coordinates directly into the shape function, eliminating the need for a local coordinate system.

However, integrating post-processing into a one-step procedure within the DIC code causes a problem that needs to be solved. This problem originates from the utilization of the assumed global field, with its corresponding shape functions, for describing displacements along both the x and y directions. This description involves decomposition into a complex coordinate system. An important consequence of this approach is the introduction of a coupling effect between the x and y displacements. This coupling effect presents a challenge in accurately determining the amplitude of displacements. Incorporating the complex decompositions can lead to complex amplitudes, which significantly complicate the derivation of the cross-correlation procedure. In addition, in certain decompositions, such as the William's solution, complex amplitudes do not provide a real physical interpretation. Therefore, a similar solution as in the two-step procedure can be employed, exploiting the property of the complex conjugate to enforce real amplitudes while allowing for complex shape functions. In contrast, FEM-based DIC allows for the splitting up of the amplitude determination by using different uncoupled shape functions for the y and x directions.

The objective function for the one-step DIC can be derived through the application of the conjugate property. This function can subsequently be minimised by computing the derivative with respect to the amplitudes of the displacement field and setting it equal to zero. This minimisation procedure aims to determine the global optimum within the region of interest, introducing the need for the area integral. This integral can be

effectively approximated using a Riemann sum. Similar to the two-step FEM-based approach, this area corresponds to the element area in order to keep the multi-scale approach. However, in general, it is not limited to this and could, in theory, be the entire region of interest. A linear system can be constructed from here, which can be solved for the sought-after amplitudes. The specific solving procedure, however, depends on the implementation details of the multi-scale algorithm.

$$|z|^2 = z \cdot \overline{z} \tag{8.19}$$

$$\eta^2 = \int\int_\Omega |a\Psi\nabla f + f - g|^2 = \int\int_\Omega (a\Psi\nabla f + f - g)(a\overline{\Psi\nabla f} + f - g) \tag{8.20}$$

$$\frac{\delta\eta^2}{\delta a} = \int\int_\Omega \Psi\nabla f \cdot (a\overline{\Psi\nabla f} + f - g) + \overline{\Psi\nabla f} \cdot (a\Psi\nabla f + f - g) = 0 \tag{8.21}$$

$$a \cdot \int\int_\Omega (\Psi\nabla f \cdot \overline{\Psi\nabla f} + \overline{\Psi\nabla f} \cdot \Psi\nabla f) = \int\int_\Omega (\Psi\nabla f + \overline{\Psi\nabla f}) \cdot (g - f) \tag{8.22}$$

$$\mathbf{Ma} = \mathbf{b} \tag{8.23}$$

Three significant terms are present in the obtained linear system: the displacement field amplitudes, the grey level difference between the reference and deformed image and the inner product of the shape functions and the grey-level gradients. Only the inner product of the gradients and the shape functions is not directly evident due to the introduced coupling of the x and y direction. This product is defined as the superposition of the complex and real direction.

$$\Psi\nabla f = \Re(\Psi) \cdot \nabla f_r + \Im(\Psi) \cdot \nabla f_i \tag{8.24}$$

However, depending on the coordinate system defined by the shape functions, it is important to note that the axes of the complex coordinate system may not necessarily align with the global x-y coordinate system of the analyzed images. Due to the discrete pixel format, the gradients are most conveniently determined in the picture's global system. Therefore, it can become necessary to perform a rotation of the gradients to align them appropriately for further analysis and computation.

$$\begin{bmatrix} \nabla f_r \\ \nabla f_i \end{bmatrix} = \begin{bmatrix} \sin\phi & \cos\phi \\ -\sin\phi & \cos\phi \end{bmatrix} \begin{bmatrix} \nabla f_x \\ \nabla f_y \end{bmatrix} \tag{8.25}$$

$$\begin{bmatrix} U \\ V \end{bmatrix} = \begin{bmatrix} \sin-\phi & \cos-\phi \\ -\sin-\phi & \cos-\phi \end{bmatrix} \begin{bmatrix} U_r \\ V_i \end{bmatrix} \tag{8.26}$$

When the multi-scale approach is used, the linear system is determined on an elemental basis, resulting in the same amount of linear systems as elements. However, because the shape functions are globally determined, their amplitudes are not unique on an elemental basis, unlike the global FEM-based approach, where each element has unique amplitudes corresponding to their nodal displacements. This means that when the global linear system is constructed, it is overdetermined and has a non-square matrix. In order to solve the overdetermined system, a least squares approach is utilized, resulting in the most likely amplitude values. This method has been chosen as it is a relatively quick and robust procedure with an inbuilt function in the Matlab software. The inbuilt function makes use of the QR decomposition (Björck, 1967) in order to solve the system efficiently.

After the system has been successfully solved for the displacement field amplitudes, the next step involves multiplying these amplitudes with the corresponding shape functions to obtain the estimated displacement field. However, due to similar reasons as for the two-step FEM-based procedure, an iterative scheme is necessary. This iterative scheme consists of initially moving the deformed image with the estimated displacement and subsequently recalculating the new estimated displacement. However, it is important to note that simply repeating this procedure would result in an estimation of the displacement between the reference image and the image that has already been displaced once. Consequently, to the b vector, an additional term is added. Specifically, this additional term involves the M matrix multiplied by the previously determined amplitudes, enforcing the solution to account for the total displacement instead. This process is repeated until convergence has been reached.

$$\mathbf{b} = \int\int_\Omega (\Psi\nabla f + \overline{\Psi\nabla f}) \cdot (g - f) + \mathbf{a}_{-1} \cdot \int\int_\Omega (\Psi\nabla f \cdot \overline{\Psi\nabla f} + \overline{\Psi\nabla f} \cdot \Psi\nabla f) \tag{8.27}$$

As a result of employing the multi-scale algorithm, mesh refinement becomes necessary once convergence is achieved at a specific scale. In the two-step FEM-based approach, this refinement is accomplished by refining the mesh and defining displacements on the newly created nodes through interpolation facilitated by their corresponding shape functions. Consequently, this newly enlarged node set serves as the initial guess for amplitudes at the refined scale.

Similarly, this refinement process is kept in the one-step procedure to establish an initial displacement estimate. However, in this case, the initial amplitude guess does not change since the number of amplitudes does not vary with scale. The difference is that the amplitudes must be multiplied by the appropriate scaling factor. This adjustment is necessary because there are more superpixels at a finer scale; consequently, the same displacement at this scale corresponds to a greater number of pixels (Which is the unit of the displacement), necessitating the application of the scaling factor to maintain similarity. This process can then be repeated until convergence at the lowest scale is reached, where a superpixel is the size of an actual image pixel.

Similar to the two-step approach, a measurement of the error is of interest. The grey-level residual can similarly be used as an initial measurement.

$$R(x) = |g(x + u(x)) - f(x)| \tag{8.28}$$

However, the Williams term amplitude variance is of particular interest to evaluate if an accuracy improvement is reached compared to the two-step approach. Due to the global definition of the correlation procedure, a displacement residual can not be obtained. Instead, the grey-level variance (σ^2) is computed by calculating the mean of the squared grey-level residuals.

To determine the resulting variance of the amplitudes, the variance properties (Eq. 8.12 and Eq. 8.13) are effectively applied within the linear system employed for amplitude determination. In order to achieve this, the system of equations is formulated at an elemental level, eliminating the need for integration as values are directly substituted for each pixel. This substitution leads to a Riemann sum realized through matrix multiplication. Moreover, to enhance visualization, a matrix q is introduced as a substitution (Eq. 8.29).

$$q = \Psi \nabla f \tag{8.29}$$

$$a\, 2q^T q = 2q(g - f) \tag{8.30}$$

$$Var(f - g) = \sigma^2 \tag{8.31}$$

$$Var(2q(g - f)) = q^T \sigma^2 q \tag{8.32}$$

$$Var(a\, 2q^T q) = (q^T q)^T\, Var(a)\, q^T q \tag{8.33}$$

$$Var(a) = \sigma^2 ((q^T q)^T)^{-1} (q^T q)^{-1} (q^T q) \tag{8.34}$$

$$Var(a) = \sigma^2 ((q^T q)^T)^{-1} = \sigma^2 ((\mathbf{M})^T)^{-1} \tag{8.35}$$

It can be observed that through the matrices' assembly, the linear system's right side (the **b** matrix) no longer appears in the covariance matrix formulation, significantly simplifying the formulation.

However, the system is presented on an element scale, whilst due to the multi-scale algorithm, the variance calculation requires an assembly of a global matrix. The least squares method is employed to resolve this global system because the total covariance matrix is not square but constituted from the elemental matrices. The use of which provides a most likely estimate of the amplitude variance. Furthermore, the scaling of the amplitudes to obtain them in the proper SI units is considered in the scaling of the variance (Eq. 8.12).

Additionally, the variance of the crack tip misalignment is of interest. However, this variable is a function of two amplitudes, which are random variables divided. No closed-form solution exists to calculate the variance for the division of two random variables. Instead, the variance could be approximated by series solutions. However, these require knowledge about the distribution and only small perturbations around the expected mean. For this reason, the determination of the variance of the crack-tip misalignment is out of this research's scope. Secondly, it is out of this research's scope because the remaining crack-tip misalignment at convergence is seen as an error estimate in its own right, as it provides a residual error of the crack-tip location.

A practical implementation consideration in the one-step DIC procedure is making use of the series

properties. Incorporating these properties is beneficial in the context of the one-step approach. However, it also introduces a practical concern: when analysing an extensive series of high-resolution images, the amount of data involved becomes significant. In the two-step approach, pictures can also be studied consecutively; however, in such cases, the series of images is generally loaded in one go and stored as a three-dimensional matrix in the working memory. This matrix approach is typically beneficial for computational speed. However, it is no longer possible when the series becomes too large. In the two-step approach, however, this can readily be overcome by performing the first step of the analysis in discrete batches and only in the post-processing step collectively considering the images and enforcing the series properties.

Within the context of the one-step approach, the solution is obtained by changing the data handling procedure of the DIC algorithm. An overarching program can execute the process that loads the reference and deformed pictures of a particular stage and sets the masking according to the mask defined in the first stage. Following, the correlation procedure can take place determining the displacement fields and the crack tip. The obtained displacements field can be stored in a distinct file. Furthermore, as an advantage of the one-step procedure, only the amplitudes and the crack tip location must be held in the working memory. These essential variables can then be taken to the subsequent evaluation of the series, allowing for continuous analyses without any memory problems. In the current implementation, a disadvantage is that the reference image must be loaded every single time; however, compared to the overall analysis time, this is an insignificant amount of time. In addition, this implementation also allows for the evaluation of the displacement field based on the previous image instead of the reference image if so desired.

8.2.1. Far-field region

Depending on the region of interest, a different procedure should be implemented in order to calculate the shape function amplitudes and the displacement field. In the case of the far-field region, the linear airy stress function should be used as the special basis (Section 3.4.2). Although the shape functions are globally defined, they are exploited on an element level in the multi-scale algorithm. The implementation of the multi-scale algorithm follows the same structure as outlined in section 3.3.7.

For the far-field region, the coordinates for each so-called element are determined by the centre location of these elements. However, when determining amplitudes for a global field, these amplitudes might be of interest in further uses. Therefore, a global shift is included in order to allow for the transfer of these coordinates from the location in the picture to a coordinate system of interest, for example, one of the corners of the region of interest (ROI).

Based on the determined element midpoint coordinates, a mesh is constructed to correspond with the pixel or superpixel locations encompassed by the element. Subsequently, by inserting this coordinate mesh into the shape functions, the corresponding values of the shape functions can be determined for each individual pixel within the element. A three-dimensional tensor is obtained by iterating this process for each shape function, capturing all the shape function values at each pixel within the element. This tensor can be reshaped into a two-dimensional matrix to allow for incorporation within the established linear system. This transformation defines the coordinates as a single-column vector while representing each shape function as a distinct column. Once the linear system has been solved and the amplitudes have been determined, the displacement field needs to be constructed in order to determine the element shift for the following iteration. The shape function values are computed similarly to those at the element level. However, a key difference is that these values are only determined at the elemental nodes to keep in line with the two-step FEM-based procedure. Once the two-dimensional matrix is constructed, it is multiplied with the amplitude vector, resulting in the global displacement vector. This vector is then reshaped to form a field representation of the displacement.

8.2.2. Notch region

Compared to the far field region, the main difference is the presence of a notch with a possible crack. This presence necessitates the use of different special basis functions, as discussed in section 3.4.2. In this research, the cracked configuration is of interest, and therefore the William's asymptotic series solution is chosen as the special basis.

When analysing the notch region with the one-step approach, accurately determining the location of the crack tip is essential, both as an important outcome in its own right and for correctly determining the displacement field. The residual method (6.1.3) is less effective due to multiple required converged solutions. Therefore, the implementation with the first singular term method is employed 6.2.3. Initially, the crack tip location is set to the notch, effectively assuming it to be zero. Furthermore, it is constrained along the x-axis, which is aligned with the crack path, as this method does not allow for simple determination of the crack tip

location in the direction normal to the crack propagation direction. Subsequently, an iterative procedure commences, wherein the crack tip assumption is adjusted by the calculated misalignment at each iteration at each scale level. This process continues until a converged solution is obtained at the pixel scale level. It should be noted that as long as the positive real axis is aligned with the crack propagation direction, the crack tip misalignment is also defined as positive in the crack growth direction.

For subsequent images in the series, the previous crack size serves as the new initial value and lower bound, ensuring consistency in the crack growth analysis.

However, when dealing with the largest cracks, the convergence of the one-step procedure may suffer due to large displacements, especially in the absence of an initial amplitude guess. Hence, starting the analysis from the smallest crack facilitates easier convergence. Subsequently, the final amplitudes obtained from this initial crack can serve as an initial guess for the amplitudes in the subsequent picture, leading to more stable results. It is important to note that the size of subsequent cracks is uncertain, which necessitates setting the mask to be as large as the maximum expected crack size from the start.

The determination of the crack-tip location introduces some complexities in implementing the shape functions within the one-step procedure. Firstly, the origin needs to be aligned with the crack tip. In the case of the far-field procedure, a general shift in the coordinate system was adequate to align the origin with the point of interest. However, according to the described procedure, analysing a series of crack growth images introduces a shift that can vary at each iteration.

Furthermore, aligning the crack propagation direction with the positive real axis requires using a rotation matrix at the element level. This step is needed to obtain an appropriate description of the shape functions. Furthermore, after determining the amplitudes, the rotation matrix is used twice: once to construct the shape function in the appropriate reference frame to multiply with the obtained amplitudes (8.9) and once again to rotate the obtained displacement field back into the global image reference frame (8.10).

The introduction of the Williams solution (3.37) presents an additional numerical concern when assessing the notch region, particularly concerning the higher-order terms. As the radius value at each point is raised to a high order, it can lead to exceedingly large values when the point is distant from the notch. Consequently, such values may result in overflow problems, reducing the accuracy or rendering the correlation procedure ineffective.

Each Williams term is appropriately normalized by r_0, preventing potential overflows (Eq: 8.37, 8.39). The normalization factor r_0 is determined as the maximum radius, which results in the radius domain being normalized to the interval [0,1]. However, this normalization leads to a deviation in the amplitudes, requiring a correction (Eq: 8.38, 8.40) post-correlation to obtain the correct Stress Intensity Factor (SIF). However, this correction is already essential during the procedure. When calculating the crack tip misalignment, the normalization alters the relative sizes of different amplitudes, which would result in an incorrect crack tip misalignment estimation.

$$r_0 = \max(r) \tag{8.36}$$

$$\Omega'_n = \frac{\Omega_n}{r_0^{n/2}} \tag{8.37}$$

$$\omega_n = \frac{\omega'_n}{r_0^{n/2}} \tag{8.38}$$

$$\Upsilon'_n = \frac{\Upsilon_n}{r_0^{n/2}} \tag{8.39}$$

$$v_n = \frac{v'_n}{r_0^{n/2}} \tag{8.40}$$

9. Total life model validation

The goal underlying the formulation of the global one-step Digital Image Correlation (DIC) procedure is to leverage its capabilities for the purpose of validating the Total-life model. This chapter discusses the remaining required modelling to perform this validation. First, further post-processing is discussed, which is still required after the one-step DIC approach, in order to obtain comparable crack growth data. Secondly, it is discussed how the data obtained from crack growth or failure data can be used to obtain the required material parameters of the total life model.

9.1. Crack growth behaviour

By utilizing the one-step DIC procedure, as discussed in the previous chapter, the crack size can be determined for each image within a series. Since the cycle interval between these images is known, it becomes possible to correlate the crack size with the number of cycles. The derivative of this relationship yields the sought-after da/dn data. However, due to the small interval between images and inherent inaccuracies, calculating the derivative of this discrete data often produces unsatisfactory results. Hence, the application of a smoothing function becomes important. The Savitzky-Golay finite impulse response (FIR) algorithm is excellent for this as it effectively smooths the data without losing distinct local features and is able to fit the steep slopes inherent in exponential behaviour.

The Savitzky-Golay FIR filter uses local polynomial regression within a moving window. At each data point, a window of a specified length is selected with an odd number of points in order to maintain symmetry. Within this window, a polynomial of a chosen degree is fitted to the data points. The polynomial coefficients are calculated using the least squares method. From there, the polynomial is evaluated at the centre point of the window, providing the value for that specific point. This is repeated for each data point, resulting in a smoothing of the data (Schafer, 2011). It is important to consider the inputs and limitations of this method. The selection of an appropriate window size and polynomial degree is crucial. A larger window size captures more information but may result in a slower response to changes in the data resulting in the loss of local features. Similarly, higher polynomial degrees give more flexibility in fitting, but can lead to over-fitting.
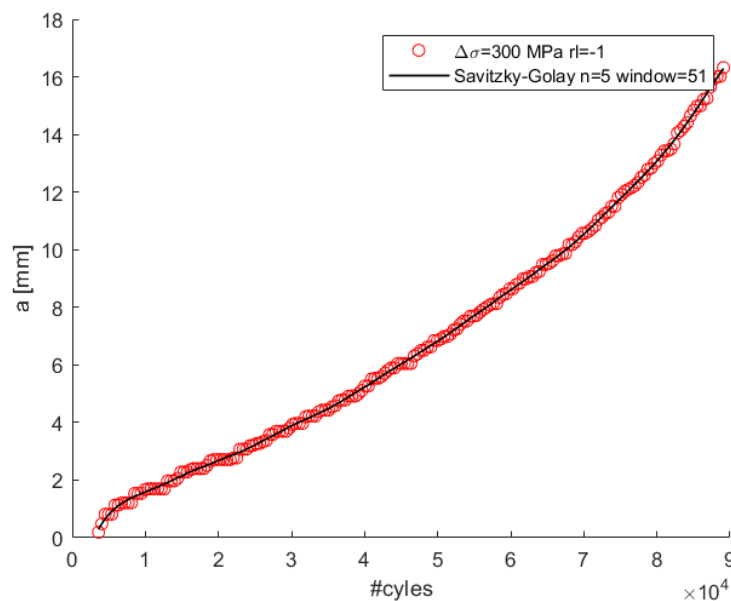

Figure 9.1: One-step DIC obtained crack size data.

From the crack growth data, it can be observed that some stepped behaviour does occur. Which is caused by a lower bound in the crack size variation, the algorithm can observe. Furthermore, it can be seen that although a window size of half the amount of data points is used, local features are still recognisable. For example, the

initial monotonic behaviour in Fig. 9.1, which is important for the conducted research as this initial stage behaviour is of interest. Compared to the fitting of an exponential function for which the inclusion of such features is significantly more challenging to achieve due to the globally prescribed nature of such a method.

The approximate gradient at each data point can be calculated by employing the central difference theorem to calculate the gradient of the function and using the cycle spacing between images as the spacing in the gradient calculation. The choice is made not to calculate a continuous gradient, which would be possible for the Savitsky-Golay fit is made because the crack growth data is generally presented as a function of the SIF, and these values are only known as discrete points as they followed from the one-step DIC as well. As can be observed in Fig. 9.2, the resulting crack growth behaviour shows a clear pattern and is not distorted by subsequent images with the same crack tip location, which would result in crack growth values of zero.
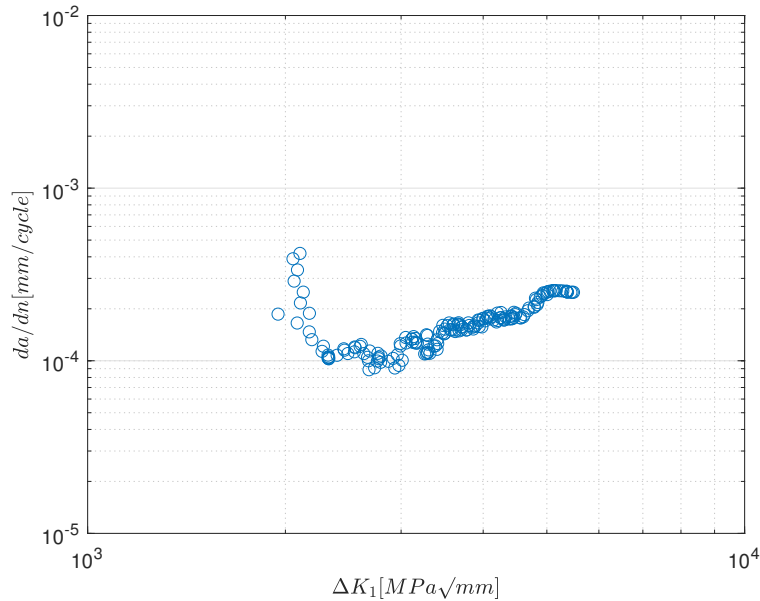
Figure 9.2: Crack growth data obtained from filtered crack size data.

9.2. Parameter estimates

The evaluation of the total life model necessitates the determination of multiple material-based parameters. These parameters are determined through a process of data fitting. While various methodologies exist for this purpose, the non-linearity of the total life formulation requires the employment of a non-linear solver. Furthermore, it is noteworthy that fatigue data can conform to either a Weibull or normal distribution, partly dependent upon the model description and if it is mid or high-cycle fatigue. Consequently, selecting an approach that affords flexibility in distribution choice is advantageous. Additionally, fatigue failure data can include run-outs, which can skew the fitting if not accounted for. In this context, the maximum likelihood estimate (MLE) procedure emerges as the preferred choice, accommodating the diverse challenges of fitting fatigue data.

The total life model can be fitted in either crack growth or specimen failure form. Fitting the model as a crack growth model offers some advantages, as it allows for direct fitting of the initial crack growth stage, which may exhibit non-monotonic behaviour. Furthermore, this approach offers higher resolution, potentially leading to increased parameter confidence. However, the crack growth data required for this method must be obtained, which can be accomplished using techniques such as Digital Image Correlation (DIC), as demonstrated in this report, or through the utilization of Potential Drop (Palkar, not Published). It is important to note that acquiring crack growth data entails additional effort and imposes limitations on the available datasets, as this data is not widely accessible.

Moreover, the inclusion of an extra processing step introduces the possibility of introducing additional errors. Alternatively, the more commonly employed approach involves fitting crack failure data directly derived from experiments. This more widely available data also allows for the consideration of welded data in contrast to the non-welded CT data utilized by Palkar, not Published.

The data set could also include run-outs in case of determination based on failure data. This requires the elaborated likelihood formulation, which includes the cumulative probability (f) function and the probability density function (F) (Qin et al. 2021).

$$\mathscr{L}(\theta; N|S) = \sum_{j=1}^{n} \mathscr{L}_j(\theta; N_j|S_j) \tag{9.1}$$

$$\mathscr{L}_j(\theta; N_j|S_j) = \delta_j \ln\{f(N_j|S_j;\theta)\} + (1 - \delta_j)\ln\{1 - F(N_j|S_j;\theta)\} \tag{9.2}$$

$$\delta_j = 1 \ \text{for a failure} \tag{9.3}$$

$$\delta_j = 0 \ \text{for a run-out} \tag{9.4}$$

$$\tag{9.5}$$

The failure data or crack growth data has a deviation from its expected value, for which a distribution must be assumed to determine the maximum likelihood parameters. Typically, a normal distribution is employed when dealing with randomly distributed events. However, a Weibull distribution might offer a more suitable fit in situations characterised by monotonic behaviour (Qin et al. 2021). Therefore, it is essential to investigate both distributions to asses which best fits the dataset. Because, the log-likelihood formulation is used the distributions should be presented in the natural logarithm form, and not in base 10 log. Furthermore in the distribution formulations x is the dependent variable and μ its expected value with a standard deviation σ. Resulting in the formulations underneath in the case of a normal distribution.

$$f_N(x; \mu, \sigma) = \frac{1}{\sqrt{2\pi}\sigma} \cdot \exp\left[-\frac{(\ln(x) - \mu)^2}{2\sigma^2}\right] \tag{9.6}$$

$$F_N(x; \mu, \sigma) = \frac{1}{2}\left[1 + \text{erf}\left(\frac{(\ln(x) - \mu)}{2\sigma}\right)\right] \tag{9.7}$$

Similar formulations can be obtained for the Weibull distribution.

$$f_w(x; \mu, \sigma) = \frac{1}{\sigma} \cdot \exp\left[\frac{(\ln(x) - \mu)}{\sigma} - \exp\left[\frac{(\ln(x) - \mu)}{\sigma}\right]\right] \tag{9.8}$$

$$F_w(x; \mu, \sigma) = 1 - \exp\left[-\exp\left[\frac{(\ln(x) - \mu)}{\sigma}\right]\right] \tag{9.9}$$

Depending on the type of fitting, the dependent variable will differ. In the case of fitting failure data, the dependent variable is the number of cycles, and its expected value can be determined by a Basquin-type relation in which the adjusted total stress parameter can be inserted.

$$\mu = \ln(C) - m \cdot \ln\left[\frac{\Delta\sigma_s}{(1 - r_{lr})^{1-\gamma} \cdot t_p^{\frac{2-m}{2m}} \cdot I_n^{\frac{1}{m}}}\right] \tag{9.10}$$

$$I_n = \int_{a_f/t_p}^{a_i/t_p} \left(\frac{1}{(Y_n(\frac{a}{tp}) + n_1 \cdot Y_n(\frac{a}{tp})^{n_2 \cdot (1-r_{lr})^{n_3} \cdot (\frac{\sigma_{max}}{\sigma_y})^{n_4}}) \cdot Y_f(\frac{a}{tp}) \cdot \sqrt{\pi\frac{a}{tp}}}\right)^m d(\frac{a}{tp}) \tag{9.11}$$

In the case of fitting crack growth data, the crack growth becomes the dependent variable, and its expected value can be determined with the two-stage crack growth formulation from the total life model. In addition it should be noted that crack growth data does inherently not have run-outs and therefore only the probability density function is required.

$$\mu = \ln\left(\frac{1}{C}\right) + m \cdot \ln\left[\frac{(Y_n + n_1 \cdot Y_n^{n_2 \cdot (1-r_{lr})^{n_3} \cdot (\frac{\sigma_{max}}{\sigma_y})^{n_4}}) \cdot Y_f \cdot (\Delta\sigma_s \sqrt{\pi a} - \Delta K_{th})}{(1 - r_{lr})^{1-\gamma}}\right] \tag{9.12}$$

Additionally, both models can incorporate a bias correction; however, when the sample size is big enough, this is not necessary. Though, independent of sample size, the Weibull distribution needs an additional correction

because otherwise, it is biased towards the 63rd percentile (Qin et al. 2021). Leading to an expected value residual equal to the euler constant (γ), and a standard deviation residual of $\frac{\pi}{\sqrt{6}}$ instead of one.

$$f_w(x; \mu, \sigma) \rightarrow f_w(x; \mu + \gamma \cdot \frac{\sqrt{6}}{\pi} \cdot \sigma, \frac{\sqrt{6}}{\pi} \cdot \sigma) \tag{9.13}$$

$$F_w(x; \mu, \sigma) \rightarrow F_w(x; \mu + \gamma \cdot \frac{\sqrt{6}}{\pi} \cdot \sigma, \frac{\sqrt{6}}{\pi} \cdot \sigma) \tag{9.14}$$

The notch and far-field factors are the remaining inputs to be determined for the parameter research. The notch factor can be obtained using the equilibrium part of the through-thickness stress distribution as described in Sec. 2.3. For the CT specimens, specifically, a crack configuration was adopted (Palkar, not published). This crack configuration results in $2\alpha = 2\pi$ for which no solution to the eigenvalue problem can be found. For this reason, the asymptotic solution needs to be adopted (9.15), where five terms have shown to provide a good fit to the FEM results (Qin et al. 2021; Palkar not published). These terms are defined by the asymptotic eigenvalues (λ_i) and their corresponding coefficients (χ_i).

$$\sigma_n \approx \sum_{i=1}^{5} \left(\left(\frac{r}{tp} \right)^{\lambda_i - 1} \mu_i \lambda_i (\lambda_i + 1)(1 - \chi_i) \right) \tag{9.15}$$

$$\lambda_i = \frac{n}{2} \quad , \quad n = 1, 3, 5, 7, 9, \dots \tag{9.16}$$

$$\chi_i = \frac{\lambda + 1}{\lambda - 1} \tag{9.17}$$

In contrast to the non-asymptotic solution, the determination of stress field amplitudes (μ_i) cannot be solely achieved by employing force and moment equilibrium (boundary) conditions in a weak form (den Besten, 2015). Instead, the Finite Element Method (FEM) is employed to derive the boundary conditions at various locations along the thickness of the material. Subsequently, a system of equations is established to solve for the stress field amplitudes (den Besten, 2015; Palkar, not published).

$$\begin{bmatrix} C_{11} & \cdots & C_{15} \\ \vdots & \ddots & \vdots \\ C_{15} & \cdots & C_{55} \end{bmatrix} \begin{bmatrix} \mu_1 \\ \vdots \\ \mu_5 \end{bmatrix} = \begin{bmatrix} F_1 \\ \vdots \\ F_5 \end{bmatrix} \tag{9.18}$$

$$C_{1i} = (\lambda_i + 1)(1 - \chi_i) \quad , \quad F_1 = 1 - r_s \tag{9.19}$$

$$C_{2i} = \lambda_i (1 - \chi_i) \quad , \quad F_1 = \frac{1 - r_s}{2} - \frac{r_s}{6} \tag{9.20}$$

$$C_{3i} = \lambda_i (\lambda_i + 1)(1 - \chi_i)(\frac{r_1}{tp})^{\lambda_i - 1} \quad , \quad F_1 = \frac{\sigma_{n1}}{\sigma_s} \tag{9.21}$$

$$C_{4i} = \lambda_i (\lambda_i + 1)(1 - \chi_i)(\frac{r_2}{tp})^{\lambda_i - 1} \quad , \quad F_2 = \frac{\sigma_{n2}}{\sigma_s} \tag{9.22}$$

$$C_{5i} = \lambda_i (\lambda_i + 1)(1 - \chi_i)(\frac{r_3}{tp})^{\lambda_i - 1} \quad , \quad F_3 = \frac{\sigma_{n3}}{\sigma_s} \tag{9.23}$$

Handbook solutions are used to determine the far-field distribution of the CT specimen. The exact formulation differs based on a sharp or a blunt notch geometry (ASTM, 2016).

$$Y_f = 0.8348 + 2.5215 \cdot \frac{a}{tp} - 0.8534 \cdot (\frac{a}{tp})^2 - 4.8182 \cdot (\frac{a}{tp})^3 + 12.1970 \cdot (\frac{a}{tp})^4 \quad \text{sharp notch} \tag{9.24}$$

$$Y_f = 0.8938 + 0.7712 \cdot \frac{a}{tp} + 9.9068 \cdot (\frac{a}{tp})^2 - 28.4867 \cdot (\frac{a}{tp})^3 + 29.577 \cdot (\frac{a}{tp})^4 \quad \text{blunt notch} \tag{9.25}$$

It should be noted that when the crack growth data ($\frac{da}{dn}$) is set out against the stress intensity factor range (ΔK_I). This stress intensity factor range is defined following the standard definition without the plasticity correction factors (Eq: 2.6) in order to keep the values comparable to different approaches.

10. Case study

A case study is performed to evaluate the application of the total life model in engineering practice. Bureau Veritas presented a case that revolved around a vessel 140 meters in length, wherein the appearance of cracks had become a serious concern. A through-thickness crack with a width of approximately 40 cm was particularly important, forming within ten years, which is significantly sooner than is expected in these types of maritime structures with a design life between 25 and 35 years. The crack is situated in the ship's bottom plate, at a hole located in the corner of a non-watertight bulkhead (Fig.10.5), classifying it as a type A hotspot. Given the presence of a significant crack formed within a relatively short period of ten years, it is probable that the crack failure can be classified as medium cycle fatigue. Additionally, considering the likelihood of small weld defects occurring within ship welds, it is reasonable to conclude that the failure process is primarily dominated by crack growth rather than crack initiation. Motivating, the choice to asses this failure with a crack-based assessment concept.

Determining the expected lifetime concerning fatigue-based failure modes consists of a two-sided analysis that considers both the fatigue resistance of the structure and the applied loading conditions. It is important to account for uncertainties within both aspects of this analysis. Generally, a conservative approach is adopted in a design process to ensure the structure remains intact and does not fail under the expected operating conditions, with quite a margin. However, when assessing failures retrospectively, the focus shifts towards ensuring the analysis matches the occurred events as closely as possible.

10.1. Loading

Understanding the ship's loading conditions is essential to determine the forces acting upon a hotspot. In a maritime context, a vessel's loading primarily follows from its weight, buoyancy, and the influence of waves. In the present case study, the design cargo load of the ship was known, as well as the two predominant cargoes transported over its operational history. These cargoes, involving bulk transportation, resulted in similar loading outcomes. The remaining loading component is the waves, which are determined in two ways. Given the constraints of this research, a detailed loading analysis was out of the scope of this research. Consequently, four rule-based wave loading cases were initially used, which can be extrapolated to describe the entire spectrum of encountered conditions. Secondly, a wave spectrum is applied with linear superposition to capture the different wave-induced effects. Both of these approaches utilized the identical assumption of the vessel being fully loaded, as it predominantly navigated from one location to another under full capacity.

10.1.1. Rule based wave loading

Detailed loading analysis was out of the scope of this research. Therefore initially, BV rules were used (Bureau Veritas, 2022). These rules provide four loading conditions: A, B, C and D, which have both a max and min state allowing for the determination of a stress range. Load case A and B represent a upright conditions, whilst load case C and D represent inclined conditions. The wave loading for the different conditions is presented in Fig. 10.1 till 10.3.
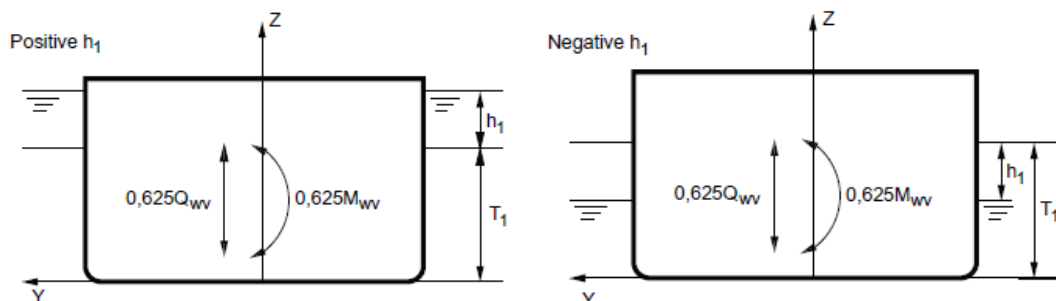

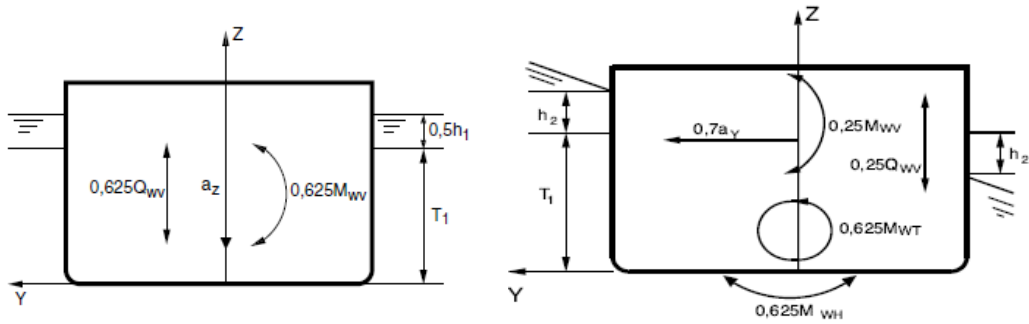Figure 10.1: Wave loading of load case A.

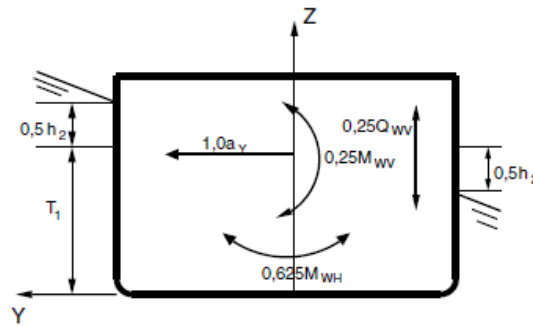Figure 10.2: Wave loading load case B (left) and C (right)

Figure 10.3: Wave loading load case D.

In these loading conditions h_1 represents the relative motion of the ship. This value varies over the length of the ship in order to capture the wave effect. Its maximum value is taken midships effectively providing the wave amplitude. The midship value follows from the wave parameter C, which is purely dependent on the ships length. The h_1 coefficient is further dependent upon the ships block coefficient ($C_b = 0.75$) and the navigation coefficient n, which for unrestricted navigation is 1, providing a h_1 of 5.5 meter. For the inclined ship conditions h_1 is combined with the roll amplitude to obtain the relative motion (h_2) in inclined condition.

$$C = 10.75 - \left(\frac{300 - L}{100}\right)^{1.5} \tag{10.1}$$

$$h_1 = 0.42 \cdot n \cdot C \cdot (C_B + 0.7) \tag{10.2}$$

The wave loading conditions are further defined by the vertical wave bending moment M_{wv}, the horizontal wave bending moment M_{wh}, the wave torque M_t, the vertical wave shear force Q_{wv}, the ships accelerations a and the draught T_1. The moments and torques follow from a midship calculation and the accelerations are defined according to wave parameters and the ships length.

These loading conditions were applied on a provided cargo hold model modelled with plate elements. The resulting stresses are applied to the boundaries of a detailed model to obtain the through-thickness stress distribution at the weld. The detailed model consists of a combination of plate and solid elements. For time performance reasons, only the bottom plating around the hotspot, the weld itself and part of the connected bulkhead are modelled as solid elements. After processing, it is validated through observation that the area of solids is large enough for the hotspot stress effects to be smoothed out before the transition to plate elements occurs.

At this transition, an additional problem exists because a node in a solid element has three DOFs, namely the translational displacement components. Whilst the plate element nodes have six degrees of freedom: the translations and rotations. Therefore, the plate could rotate freely in reference to the solid when only connected to one node, and no rotation can be transmitted. Additional techniques are therefore required to resolve this problem.

A simple solution to resolve the plate rotation on the solid mesh is to extend the plate elements into the solid for at least two nodes. However, further extension can provide better results, and therefore, the plate is extended three nodes into the solid in the used model. This allows the transmission of both translational and rotation deformation between the plate and solid elements. The drawback of this simple method is the additional mass introduced near the joint area, which may affect the dynamic analysis results. However, only static modelling is required in this research.
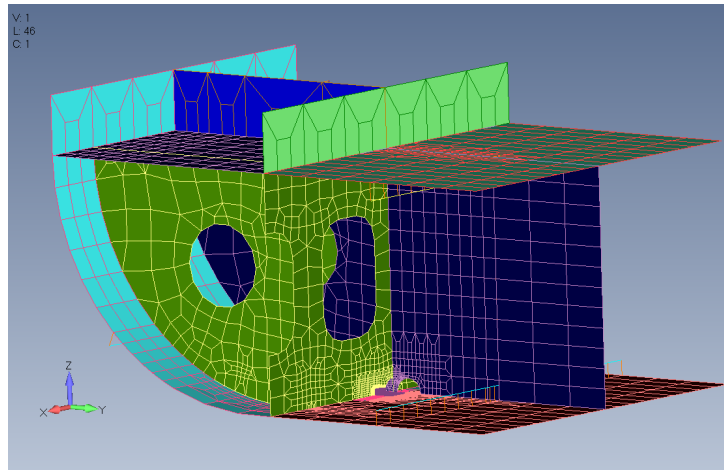
Figure 10.4: Overview of the detailed model with plate and solid elements.
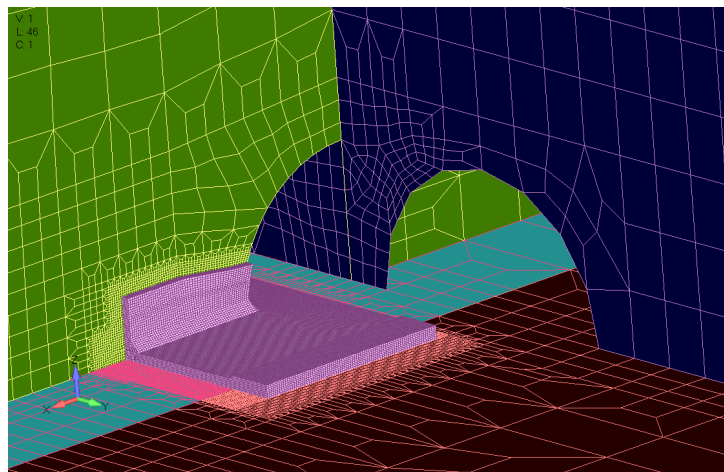
Figure 10.5: Overview of the solid elements within the detailed model.

The loading conditions provided by Bureau Veritas include global loading and local water pressure, considering a single representative sea state. However, it is important to note that this single sea state is compensated for at the fatigue resistance side. This compensation is performed through linear superposition, where a gamma function is used to account for the entire sea spectrum (Eq. **??**). Furthermore, the probability of exceedance is incorporated into this combination, ensuring a conservative evaluation of the fatigue resistance.

10.1.2. Wave spectrum loading
To fully make use of the total life concept, the current loading determination approach based upon the Bureau Veritas rule cases needs to be revised. The assumption of linearity between sea states is invalidated due to the presence of non-monotonic behaviour, which can vary based on factors such as the loading ratio and mean stress. Therefore, it is necessary to determine the loading conditions at various sea states, and the linear superposition only comes into play subsequently when combining the damages from different sea states into

a total damage value. This approach also offers more flexibility in the considered sea states, which can be effectively used retroactively assessing the damage if the ship's sailing routes are known.

From AIS data obtained by Bureau Veritas, it is known where the ship sailed during its lifetime. It sailed approximately a third of the time in the Baltic, a third in the North Sea and a third in the Atlantic Ocean. Therefore, the scatter diagrams of the respective sea states can be taken and superpositioned in order to obtain a sea spectrum representative for the ship of concern. These individual sea states were then inserted as loads upon the full ship model in the in-house hydro-structural solver from Bureau Veritas (Homer) to obtain the loads around the weld detail. This in-house solver integrates a hydrostatic solver (Hydrostar) with a finite element solver (Nastran) to achieve a coupled analysis. Within the scope of this study, the coupling is specifically confined to linear hydro-structural interactions. This results in the vessel being treated as a rigid body while still responding to the wave dynamics. Consequently, the model assumes a scenario without hydro-elastic effects, a deliberate simplification made in the context of the research's defined boundaries and objectives. For each defined case, the solver provides a time series solution. From this solution, the displacements and forces upon the model, including the local water pressures, can be obtained at specific moments in time.

These loads can be applied to the weld detail FEM model in order to obtain the through-thickness stress distribution. However, Because the stress range needs to be obtained, each sea state's maximum and minimum loading conditions are required. Three points in the time analysis are evaluated for each sea state in order to achieve a sinusoidal description of the loading. From this description, each sea state's amplitude, mean loading and phase shift can be obtained.

This procedure means that the number of calculations increases rapidly with increasing sea-state. For that reason, the obtained linear superposition of the three sea spectra was reduced to a reduced spectrum in which the values of surrounding sea states were combined into a single sea state.

Moreover, given the evaluation of a free-floating model, the wave's orientation becomes a significant factor. The decision was made to reduce the directional spectrum and only assess the front quartering waves from both directions. Analysing the response amplitude operators at a local level revealed that these orientations are representative of the entire directional range, except for the beam waves. Nevertheless, it is unlikely for any ship's captain to position the vessel in such an alignment with the waves due to the inherent discomfort from the corresponding ship movements. The difference in response between waves reflected symmetrically across the waterline is attributed to the localised response amplitude operator (RAO) characteristics.

The two evaluated waves' damage results are averaged to obtain a representative value for each sea state. An accuracy improvement could be made by employing a directional spectrum. However, this would require a significant increase in the evaluated states and knowledge of the general heading courses to determine the ship's position relative to the spectrum at times, significantly increasing the required amount of data and complexity of the evaluation.

Hs [m]/Tz [s]	4.5	7.5	10.5	13.5
2.5	294.0	310.6	31.0	1.2
5.5	7.6	53.2	19.6	1.4
8.5	0	2.4	3.0	0.4

Table 10.1: Reduced representative sea spectrum for the ship of concern.

10.2. Fatigue resistance

The other side of fatigue analysis is investigating fatigue resistance and determining the total stress parameter to estimate the lifetime under cyclic loading conditions. The analytical through-thickness stress distribution must be determined to establish the total stress parameter. For this purpose, a Finite Element Method (FEM) model is employed to determine the stress distribution at the weld under specific loading conditions. Given that the weld is a V-shaped notch, its corresponding analytical formulation is applied to describe the stress distribution. It is noteworthy that, in contrast to the CT specimens, the asymptotic solution is not employed in this case. This choice is made to maintain consistency with the parameter determination process. Although the CT specimen data is fitted according to the asymptotic solution, the welded data is not. Because the analysed detail is also welded, it is considered more appropriate to keep similarity with its determination.

Moreover, particularly at the initial stage, when cracks are small, the stress distribution is likely to be predominantly influenced by the presence of the notch. Consequently, achieving a good fit with the FEM model in an un-craked state would not be reached.

The weld toe notch stress distribution is given in the Eq. 10.3. In order to obtain the far-field factor (Eq. 2.7), it is essential to exclude the far-field bending factor $(-2 \cdot r_s \cdot \frac{r}{tp})$, in order to exclude far-field behaviour from the notch factor.

$$\sigma_n\left(\frac{r}{tp}\right) = \sigma_s \cdot \left[\left(\frac{r}{tp}\right)^{\lambda_s - 1} \mu_s \lambda_s (\lambda_s + 1)[\cos([\lambda_s + 1]\beta) - \chi_s \cos([\lambda_s - 1]\beta)] + \right.$$

$$\left. \left(\frac{r}{tp}\right)^{\lambda_a - 1} \mu_a \lambda_a (\lambda_a + 1)[\sin([\lambda_a + 1]\beta) - \chi_a \sin([\lambda_a - 1]\beta)) + C_{bw}(2 \cdot \frac{r}{tp} - 1) - 2 \cdot r_s \cdot \frac{r}{tp} \right] \quad (10.3)$$

Subsequently, the eigenvalue problem must be solved to obtain the analytical solution (Eq. 10.4). In order to calculate this, the notch angle (2α) needs to be inserted. In the present context, where the weld in question is a 45-degree weld, the notch angle is 225 degrees. Resulting from the eigenvalue problem also come the respective eigenvalue coefficients (Eq. 10.5).

$$\left. \begin{array}{l} \lambda \sin(2\alpha) + \sin(\lambda 2\alpha) = 0 \\ \\ \\ \lambda \sin(2\alpha) - \sin(\lambda 2\alpha) = 0 \end{array} \right\} \quad \forall (\lambda > 1, \lambda \neq 1) \quad (10.4)$$

$$\chi_s = \frac{\cos[(\lambda_s + 1)\alpha]}{\cos[(\lambda_s - 1)\alpha]}, \quad \chi_a = \frac{\sin[(\lambda_s + 1)\alpha]}{\sin[(\lambda_s - 1)\alpha]} \quad (10.5)$$

These eigenvalues and their coefficients are separated based on the symmetric (cos(.)) and anti-symmetric (sin(.)) part. Besides the eigenvalues and coefficients, these parts also have an amplitude (μ_s, μ_a) similar to the asymptotic solution. These amplitudes can be determined analytically by employing force and moment equilibrium in the weak form (den Besten, 2015).

$$\mu_s = \frac{C_{bw}(\lambda_a + 1) + 3(\lambda_a - 1)}{6(\lambda_a - \lambda_s)(\cos((\lambda_s + 1)\beta) - \chi_s \cos((\lambda_s - 1)\beta))} \quad (10.6)$$

$$\mu_a = \frac{-(C_{bw}(\lambda_s + 1) + 3(\lambda_s - 1)}{6 \cdot (\lambda_a - \lambda_s) * (sin((\lambda_a + 1)\beta) - \chi_a \sin((\lambda_a - 1)\beta)))} \quad (10.7)$$

Determining structural stress in the base plate is performed by extracting nodal forces (Eq. 2.4,2.5) from the Finite Element Method (FEM) model throughout its thickness. In FEMAP, this is done by creating a Free body of the elements at the weld location, which allows for the extraction of external forces acting on that specific free body. It is important, however, to ensure that the nodes used for force extraction do not lay on the corners of such a free body. Because in these cases, the forces are halved as the nodal force for that node, corresponding to the adjacent element, is not taken into account.
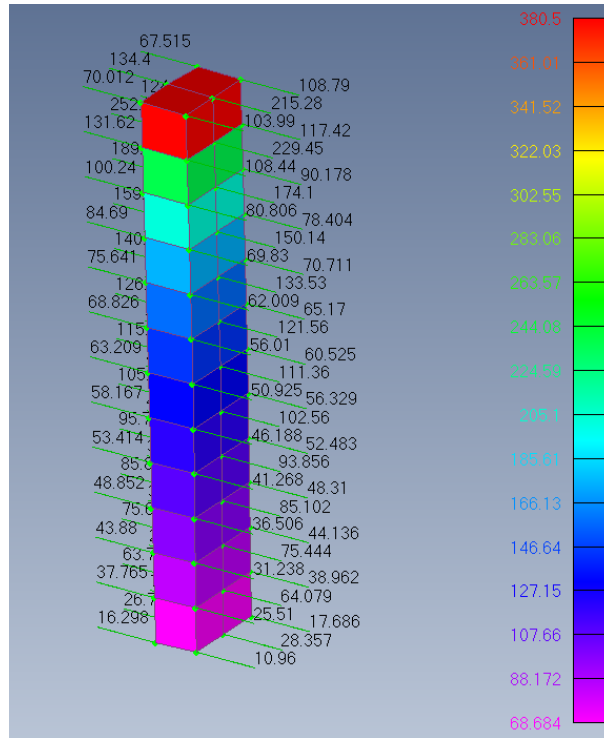
Figure 10.6: Nodal Forces obtained trough free body in Femap.

The only remaining parameter to be determined is the weld load-carrying stress coefficient (C_{bw}), which can be derived through empirical functions established through experimental investigations (Qin et al. 2021). However, given the limited number of distributions under consideration, it is also possible to individually fit each distribution's coefficient.

Once the analytical stress distribution is determined, the notch factor can be calculated as a function of the self-equilibrating stress component of the stress distribution (Eq.2.7). However, the far-field factor must be determined using the handbook solution (Tada et al. 2000). In the case of a hotspot of type A, the standard far-field solution corresponds to the elliptical crack solution. However, this solution requires knowledge of the elliptical ratio, which is difficult to determine. Estimations could be made based on different criteria; however, these have a high level of uncertainty.

$$\Phi = \frac{\pi}{2} * (1 - \frac{1}{4} * (1 - (\frac{a}{c})^2) - \frac{3}{64} * (1 - (\frac{a}{c})^2)^2 - \frac{5}{1024} * (1 - (\frac{a}{c})^2)^3 - \frac{175}{65536} * (1 - (\frac{a}{c})^2)^4) \tag{10.8}$$

$$M_1 = 1.13 - 0.09 * \frac{a}{c} \tag{10.9}$$

$$M_2 = -0.54 + \frac{0.89}{0.2 + \frac{a}{c}} \tag{10.10}$$

$$M_3 = 0.5 - \frac{1.0}{0.65 + \frac{a}{c}} + 14 * (1.0 - \frac{a}{c})^{24} \tag{10.11}$$

$$Y_{fm} = \frac{M_1 + M_2 * (\frac{a}{tp})^2 + M_3 * (\frac{a}{tp})^4}{\Phi} \tag{10.12}$$

$$G_1 = -1.22 - 0.12 * \frac{a}{c} \tag{10.13}$$

$$G_2 = 0.55 - 1.05 * (\frac{a}{c})^{0.75} + 0.47 * (\frac{a}{c})^{1.5} \tag{10.14}$$

$$Y_{fb} = \left((M_1 + M_2 * (\frac{a}{tp})^2 + M_3. * (\frac{a}{tp})^4 \right) * \frac{1 + G_1 * \frac{a}{tp} + G_2 * (\frac{a}{tp})^2}{\Phi} \tag{10.15}$$

Alternatively, an edge crack solution could be employed, although these solutions are typically meant for hotspot types B and C. However, upon examining the FEM results (Fig. 10.7), it can be seen that the stress

distribution remains relatively constant along the weld end, implying limited three-dimensional effects. Consequently, the adoption of an edge crack solution is justifiable. Moreover, the edge crack configuration generally yields a larger far-field factor; thus, adopting it as an approach leads to a more conservative estimation.

$$Y_{fm} = \sqrt{\frac{2}{\pi} * \tan(\frac{\pi}{2} * \frac{a}{tp})} * \frac{0.752 + 2.020 * \frac{a}{tp} + 0.37 * (1 - \sin(\frac{\pi}{2} * \frac{a}{tp}))^3}{(\sqrt{\frac{a}{tp}} * cos(\frac{\pi}{2} * \frac{a}{tp})} \tag{10.16}$$

$$Y_{fb} = \sqrt{\frac{2}{\pi} * \tan(\frac{\pi}{2} * \frac{a}{tp})} * \frac{0.923 + 0.199 * (1 - \sin(\frac{\pi}{2} * \frac{a}{tp}))^4}{\sqrt{\frac{a}{tp}} * cos(\frac{\pi}{2} * \frac{a}{tp})} \tag{10.17}$$
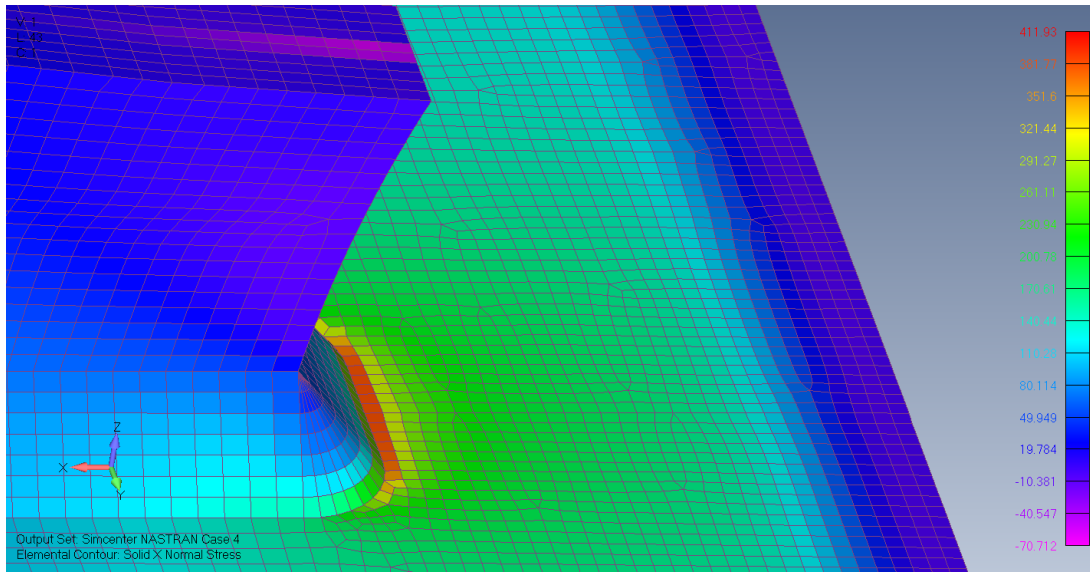
Figure 10.7: Stress distribution at the weld

Once Yn and Yf are determined, the crack growth model can be established, provided that the fitting parameters from the total life model have also been determined. Integration across the entire thickness enables the estimation of the structural detail's lifetime. In these integration procedures, the Simpson's method is commonly employed. However, it is worth noting that in the vicinity of singularities, the Simpson's method may exhibit slightly reduced performance. Therefore, Gauss-Kronrod quadrature integration has been employed as well as it could improve accuracy and efficiency, as it generally demonstrates superior behaviour and faster convergence. When comparing the two integration methods, the Gauss-Kronrod quadrature showed faster computational performance but no significant difference in outcome was observed. The lower bound of the integration (a_i) is taken as 10^{-3}, and the upper bound is taken as the full plate thickness of eleven millimetres.

Once the total stress parameter has been determined, the expected cycles of fatigue resistance can be determined according to the single slope Basquin type relation.

$$N = \frac{1}{C} \cdot St^{-m} \tag{10.18}$$

The obtained lifetime in terms of cycles (N_{if}) must subsequently be converted into an anticipated lifetime in chronological units. The expected lifetime in cycles is obtained based on an assumed loading condition, which the ship is expected to encounter a certain number of times within a specified time frame. Consequently, these encounters result in an expected number of cycles (n_i).

Subsequently, the estimation of the damage caused during the specific time frame related to the specified loading condition is determined by employing Palmgren-Miner's linear damage accumulation model. The extrapolation of the damage accumulation from this particular loading condition to encompass the entire

load spectrum, or the application of linear superposition to account for different loads, enables the determination of the cumulative damage that has occurred during the specified time frame. The total expected lifetime can be determined through extrapolation from the damage sustained within this time frame.

$$\sum D_i = \sum \frac{n_i}{N_{if}} \tag{10.19}$$

Palmgren-Miner's linear damage accumulation model does not consider the loading sequence, resulting in the potential loss of certain advantages offered by the employed total life model. The model's incorporation of both monotonic and non-monotonic behaviour introduces sequential effects, as the initial crack growth could be rapid under non-monotonic conditions, followed by steady growth under loads that in the short crack growth stage only cause minor damage due to monotonic behaviour. In such a case, this would imply that the lifetime would diminish compared to the scenario where the loading order was reversed.
However, integrating sequential information would require an elaborate loading profile, which is typically unavailable during the ship's design stage, as well as for the ship under consideration. Consequently, it can be concluded that employing this concept does not lead to the loss of any significant information.

The Bureau Veritas rules (Bureau Veritas, 2020) provide a method for extrapolating induced fatigue damage from a single loading condition to a spectrum. This is achieved by assuming that the applied stress ranges follow a Weibull distribution (with shape parameter $\zeta = 1$). Additionally, the scaling parameter can be defined based on the stress range of the analysed loading condition and its derived probability of exceedance (p_r). The probability of exceedence corresponding to the defined loadcases A till D is defined according to the BV rules as 10^{-5}.
To describe the damage spectrum, the single slope Basquin relationship and the Palmgren-Miner's linear damage accumulation model are incorporated, enabling the determination of the damage distribution. The spectral mean can be calculated from this, resulting in the total yearly accumulated damage.

$$D = \frac{N_y}{1/C} \cdot \frac{(\Delta S_t)^m}{-(\ln(p_r))^{\frac{m}{\zeta}}} \Gamma_c \left[\frac{m}{\zeta} + 1 \right] \tag{10.20}$$

$$N_y = \frac{365 \cdot 24 \cdot 3600}{T_s} \tag{10.21}$$

$$T_s = 4 \log_{10}(L) \tag{10.22}$$

III

Results

11. Reference specimen DIC

The one-step and two-step DIC procedures described in Chapter 8 were initially developed to analyse certain reference specimens. This chapter presents the results of the developed approaches applied to these reference specimens. The analysis of the reference specimens is performed in order to evaluate the developed procedures. With the simultaneously obtained crack size and SIF from the one-step approach, the first aim of this thesis is achieved. The first set of analysed images originate from Roux and Hild, 2006. The reference and deformed images analysed in this paper provided a baseline to confirm the displacement fields around an angled crack from the two-step and the one-step approach. Second, a series of images from den Besten, 2015 is used to evaluate the far-field procedure and the crack growth evaluation of a series of images.

11.1. Local two-step FEM-based approach

Initial investigation into two-step DIC was performed using a series of images from den Besten, 2015. The two-step FEM-based method (Q4 DIC) (Roux & Hild, 2006) was employed on the far field of this series. The obtained discrete displacement field from the FEM-based approach showed behaviour consistent with the expected distribution in a far-field location. The special basis derived from the linear airy stress function (Eq. 3.26) was mapped upon the discrete field in the following post-processing step. The far-field structural stress could also be obtained from this field, which aligned with the values obtained by den Besten, 2015. The research from den Besten, 2015 uses a commercial local subset-based DIC algorithm (Istra4D, Dantec Dynamics).
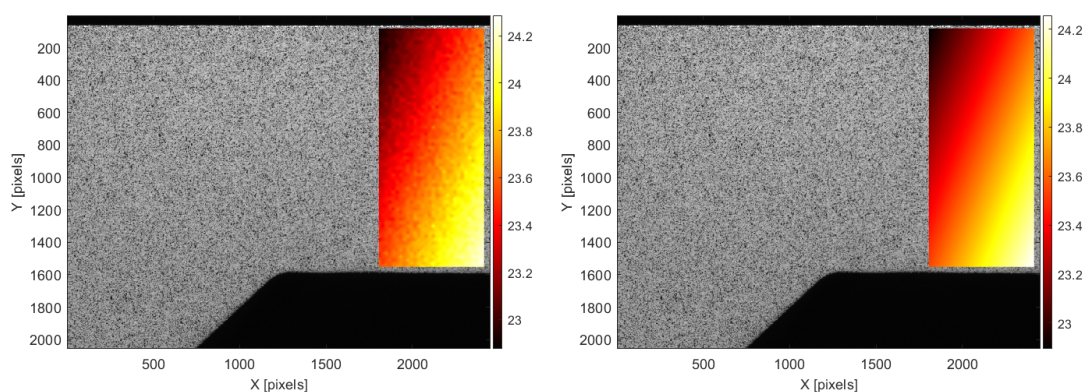

Figure 11.1: Discrete Q4 (left) and post-processed (right) displacement field obtained by two-step FEM-based DIC.

In order to further investigate the two-step FEM-based DIC (Besnard et al. 2006) procedure in the notch region, the approach was used to obtain the discrete displacement around a crack. The image presented in Roux and Hild, 2006 was evaluated because it can also provide insights for the one-step DIC procedure. Following texture quality results and the size reported in Roux and Hild, 2006, an element size of 8 by 8 pixels was employed.
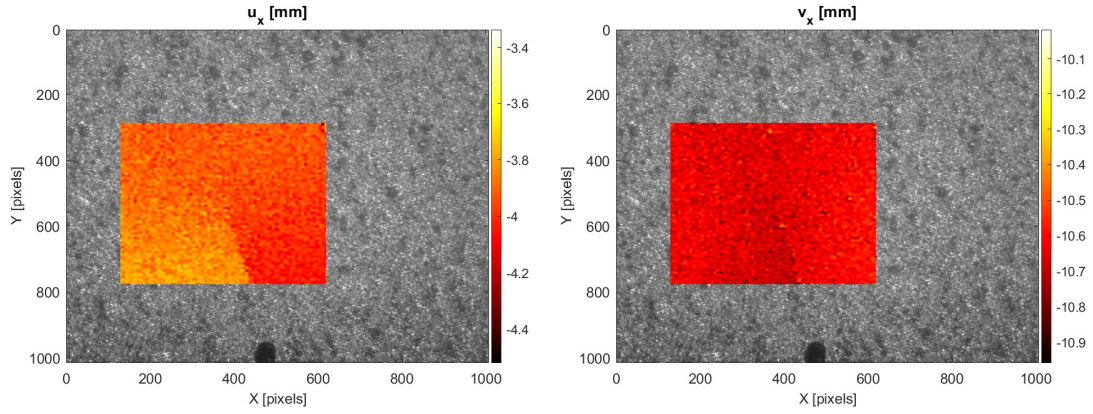
Figure 11.2: Displacement field obtained by two-step FEM-based DIC before post-processing.

The obtained displacement fields showed no observable difference to those obtained by Roux and Hild, 2006. Which is expected as the same correlation procedure (Besnard et al. 2006) was employed to obtain the displacement field. In addition, the residual error field has been obtained from this procedure. The error is presented as the average grey level residual for each of the evaluated elements. This means that on a pixel scale the local residual can be higher that reported in the presented image.
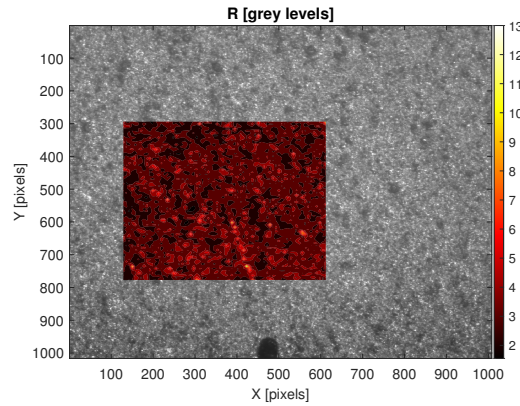
Figure 11.3: Grey level error field at element level from two-step FEM-based DIC

Upon determining the discrete displacement fields, the post-processing procedure step of the two-step approach is executed. The precise location of the crack tip is established by employing the residual method, as outlined by Roux and Hild, 2006. Specifically, the x-coordinate of the crack tip is located at 373 pixels from the left edge of the presented image, while the y-coordinate is positioned at 534 pixels from the image's top edge. In addition to these parameters, the angle of orientation is required, as aligning the positive x-axis with the direction of crack propagation is necessitated for the applied special basis functions. This angle is derived through the residual method, which manipulates the crack tip position to determine the angle's value. The resultant angle is determined to be 105.1 degrees, from which 90 degrees reflects the axis orientation definition.

Notably, the assumed special basis is a modified version of the Williams series solution (Roux & Hild, 2006). This formulation does not include the singular term which is generally included to account for the plastic behaviour. This formulation is chosen to keep similarity with the original research. However, this has as a side effect that the singular term can not be employed to estimate the crack-tip location.

The material in the analysed image is a silicon based metal and has a Young's modulus of $410 GPa$ and a poison ratio of 0.15. The shear modulus can be determined from these parameters assuming isotropic material behaviour ($G = \frac{E}{2*(1+\mu)}$).
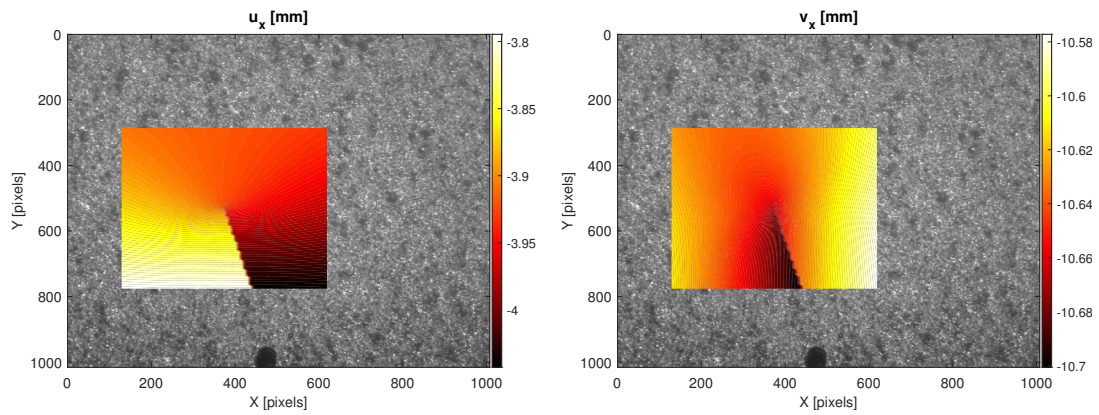
Figure 11.4: Displacement-field obtained after post-processing in two-step FEM-based DIC.

When observing the fields, a clear distinction can be noted compared to the results obtained by Roux and Hild, 2006. First, the obtained crack path is significantly less smooth; however, this is argued to be due to a difference in representation, As the field above is shown as the post-processed results mapped on the FEM-based DIC grid. However, the obtained amplitudes can present the field on a finer grid or as a continuous function. However, besides the resolution, the obtained fields have no observable differences.
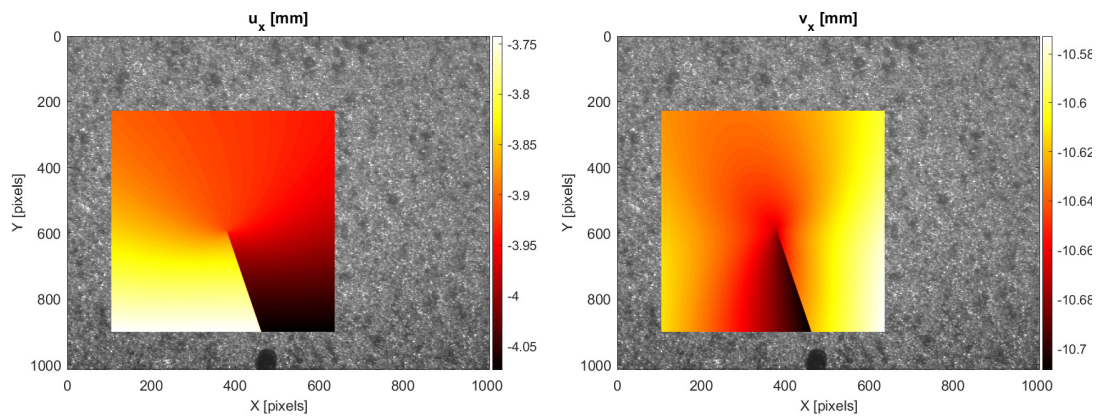
Figure 11.5: The two-step FEM-based displacement fields represented on a 1 pixel size grid.

The post-processing procedure introduces an inherent error due to disparities between the acquired global displacement fields and the ones they are mapped on obtained by FEM-based DIC. This error can be represented as a residual error field. Notably, in contrast to the error field derived for the FEM-based DIC, this residual is expressed in pixels, reflecting the input.
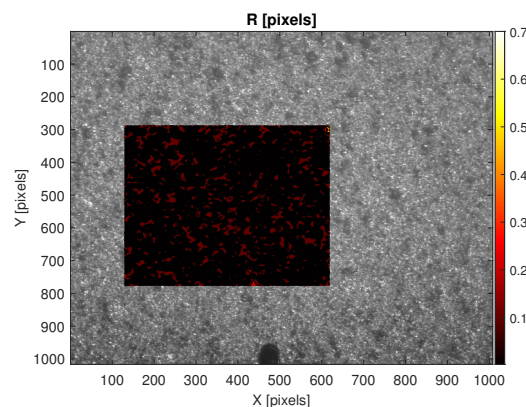

Figure 11.6: Residual displacement in pixels after postprocessing

The Stress Intensity factors can be determined with the amplitudes from the obtained displacement field. Because the employed shape functions do not directly correspond to the William's solution, the fifth and sixth amplitude must be corrected by the factor $G \cdot \sqrt{2\pi} \cdot 4$ to obtain the stress intensity factors and converted from $\sqrt{mm}$ to $\sqrt{m}$. The resulting Stress Intensity Factors (SIFs) are $K_1 = 2.396, \text{MPa}\sqrt{\text{m}}$ and $K_2 = 0.044, \text{MPa}\sqrt{\text{m}}$. These values are observed to be slightly larger than those obtained by Roux and Hild, 2006. However, they fall within the presented confidence interval, which is based on slightly differing crack tip-locations. Additionally the crack angle could differ slightly explaining small deviations.

11.2. Global one-step approach

Because Roux and Hild, 2006 also presented the outcomes from the implementation of a global one-step approach, these outcomes and those of the two-step approach can be compared to the procedure developed in this research. For the one-step approach, the same shape function is used as in the post-processing step (second step of two step approach) for similarity. However, two distinct differences in the method have been observed. Firstly, the method from Roux and Hild, 2006 does not employ the multi-scale algorithm but instead corrects immediately for the mean displacement, eliminating iterations. However, later implementations of the procedure incorporate the calculation of the mean displacement. An additional difference follows from the noise formulations where the **M** matrix (Eq. 8.23) is square, pointing towards the use of a single element, which is in line with not using a multi-scale algorithm.
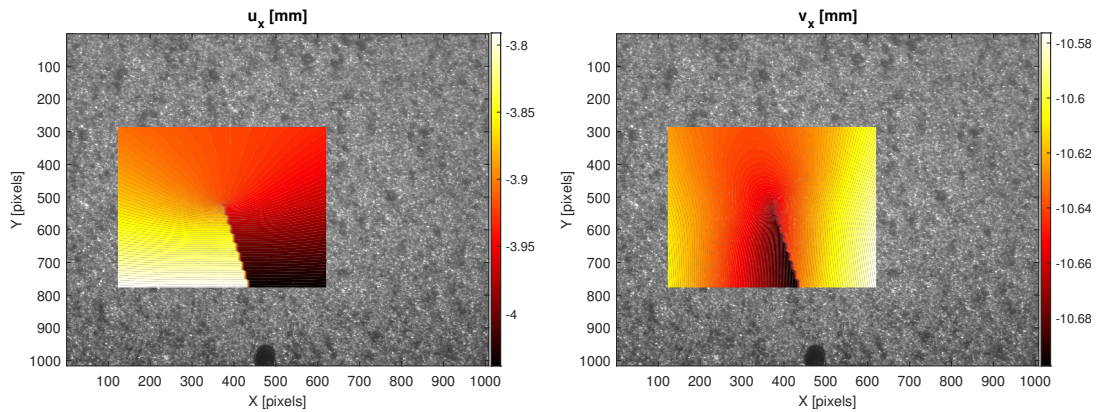

Figure 11.7: Displacement field obtained by one-step global DIC.

A slight difference of the displacement fields can be observed in contrast to to the two-step FEM based approach. However, the results seem to perfectly align with the fields obtained by Roux and Hild, 2006. Following, the identical correction factor as in the post-processing step the SIFs can be determined. The resulting values are $K_1 = 2.354 \, \text{MPa}\sqrt{\text{m}}$ and $K_2 = 0.089 \, \text{MPa}\sqrt{\text{m}}$, which similar to the two-step approach prove to be slightly greater that the values obtained by Roux and Hild, 2006. Which, can indicate a difference in on of the underlying assumptions.

For the one-step approach the residual error field can also be determined. The error field below is presented on element and pixel level.
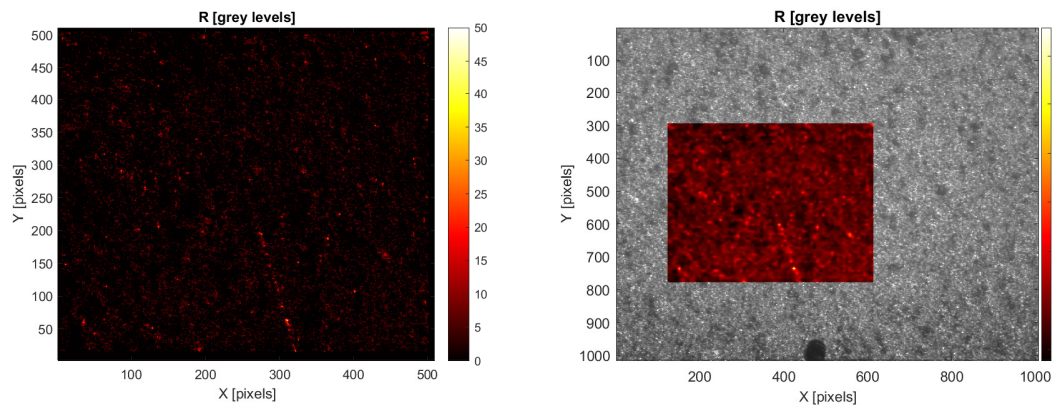
Figure 11.8: Grey level residual obtained by one-step global DIC, at element level (left), and pixel level (right).

The Obtained error field was not completely in line with the one presented in Roux and Hild, 2006 as the maximum local error on a pixel level was 50 grey levels instead of 30, and the obtained mean residual was 3.5 instead of 1.5 grey levels. It is currently unknown where this discrepancy comes from, but a possibility is a difference in the determination of the displacement. In the implementation presented in this study, the Fourier shifting property was used in order to sub-pixel shift the image to the determined location.

However, compared to the mean error value of the two-step FEM-based approach, the value aligns with the expectations. The obtained mean error value was 3.43 grey levels in that case, and due to the increased enforcement of continuity, the error is expected to be higher than the one resulting from the first step in the two-step approach. However, the gain is expected to be made by eliminating the post-processing step, which adds a mean error of 0.079 pixels in displacement.

In order to investigate the crack-tip estimation based on the first singular term in a one-step algorithm, a series from den Besten, 2015 was investigated. With a 50 pixel wide masking along the crack path, the x-coordinate of the crack is set at the notch and an angle of 90 degrees to align the x-axis with the propagation direction. Similar to the two-step approach from den Besten, 2015 five, William's terms were used to map the displacement field.
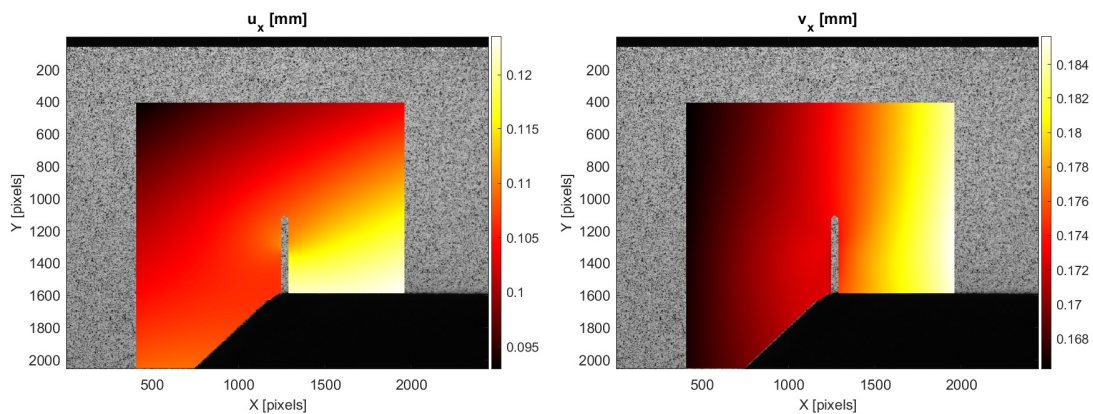

Figure 11.9: Displacement fields obtained by one-step global DIC.

As observed from the displacement field, the applied mask is relatively large. This masking size is used because the same mask is applied on every image in the series, requiring the largest size crack to be encapsulated by the masking region. Because the cracks evaluated within this procedure are relatively small, it is chosen to start the evaluation with the largest crack in the series. This procedure can help provide a better initial guess for the smallest specimens where the correlation procedure might have difficulties. In addition, this allows for a procedure where the height of the masking along the crack path can be decreased after determining the crack location of each subsequent image. This allows for more of the notch-affected region to be considered, increasing the accuracy of the one-step DIC procedure. For this same reason, the width of the

masking was kept small as well. However, for larger crack sizes, the widening of the crack can become larger than the masking width, causing instabilities in the correlation procedure. Due to these instabilities, the six images with the largest crack size in the series were excluded. However, they could be added by performing a separate evaluation with an adapted mask.
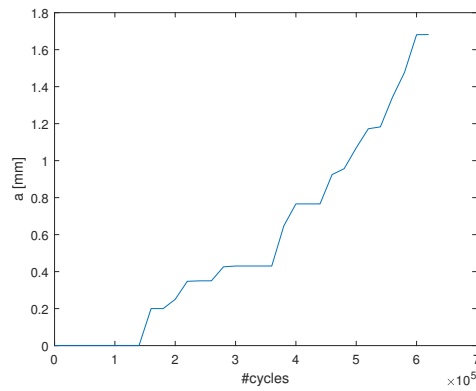

Figure 11.10: Crack growth obtained one-step DIC

From the obtained crack sizes a clear series behaviour can be seen. In addition, the general size of the obtained cracks was in line with previous findings (den Besten, 2015). However, the smoothness of the function was worse than the obtained findings with the two-step FEM based approach. From this investigation it was concluded that the general principle works, but the masking should be further investigated as well as the number of William's terms.

12. Compact tension specimen DIC

The first aim of this thesis was to introduce the one-step DIC approach for the simultaneous determination of crack tip and field data, as demonstrated in the previous chapter on reference specimens. This chapter conducts DIC analysis on CT specimens previously subjected to potential drop measurements and used to establish the total life model. These results can be used to reach the second aim of validating the total life model.

Firstly, the applied loading on these specimens is examined to assess its alignment with the results derived from the DIC methodologies. Subsequently, the texture quality is evaluated to determine the initialisation parameters for the DIC procedure. Following this, the Stress Intensity Factor (SIF) and crack size results are obtained from which the crack growth relationships are established. The results are compared to the analytical and potential drop estimates.

Three DIC approaches are employed to determine the accuracy of the obtained SIF values. The two-step and one-step approaches are initially utilised, employing the Williams formulation to derive the SIF. A convergence study is employed to determine the required amount of Williams terms in the analysis. The third is an adapted two-step approach, using a path-independent integral method applied to the FEM-based DIC field to derive a Williams-independent SIF formulation. Lastly, error estimates are presented to compare the two-step and one-step approaches.

12.1. Loading

For the purpose of validating the Total life concept, the pictures taken during five different experiments have been analysed with the one-step DIC procedure. Due to time constraints, it was only possible to analyse part of the data set. Therefore, a selection was made based on spreading the loading ratios and expected monotonic and non-monotonic behaviour. The respective loading parameters of these five sets are presented in Tab. 12.1.

	$\Delta\sigma_s$ [MPa]	r_{lr}
Serie 1	300	0.1
Serie 2	300	0.1
Serie 3	120	0.4
Serie 4	300	-1
Serie 5	200	-1

Table 12.1: Loading parameters analysed experiments

Further measures have been employed to validate the applied load on the specimen. Initially, a straightforward analytical calculation procedure was conducted. Involving computing the moment of inertia based on the specimen's thickness of 8 mm and the uncracked length at the precise notch location of 54 mm. Subsequently, a structural stress value is obtained at the notch site within the uncracked configuration by combining this moment of inertia with principles of moment and force equilibrium.

$$I = \frac{1}{12} \cdot tp \cdot (W - a_n)^3 \tag{12.1}$$

$$M = -F \cdot (a_n + \frac{W - a_n}{2}) \tag{12.2}$$

$$\sigma_b = -\frac{\frac{W - a_n}{2} \cdot M}{I} \tag{12.3}$$

$$A = tp \cdot (W - a_n) \tag{12.4}$$

$$\sigma_m = \frac{F}{A} \tag{12.5}$$

$$\sigma_s = \sigma_m + \sigma_b \tag{12.6}$$

The forces required to compute the structural stress are extracted from the registration files sourced from the exciter. Notably, the experimental setup employed an INSTRON force-controlled exciter to impart the forces during the experiments. It has been observed that the applied forces required about 15 cycles to stabilize. After which fluctuations were limited to $0.1 kN$, leading to the reported forces underneath.

	F [kN]	I [cm^4]	A [mm^2]	M [$\frac{kN}{mm}$]	$\sigma_m[MPa]$	$\sigma_b[MPa]$	$\sigma_s[MPa]$	$\Delta\sigma_s[MPa]$	r_{lr}
Serie$_{1-2,max}$	25.00	10.498	432	-1075	57.9	276.5	334.4	-	-
Serie$_{1-2,min}$	2.55	10.498	432	-110	5.9	28.2	34.1	300.3	0.1
Serie$_{3,max}$	14.98	10.498	432	-644	34.7	165.7	200.3	-	-
Serie$_{3,min}$	6.00	10.498	432	-258	13.9	66.4	80.2	120.1	0.4
Serie$_{4,max}$	11.20	10.498	432	-482	25.9	123.9	149.8	-	-
Serie$_{4,min}$	-11.20	10.498	432	482	-25.9	-123.9	-149.8	299.6	-1.0
Serie$_{5,max}$	7.45	10.498	432	-320	17.2	82.4	99.6	-	-
Serie$_{5,min}$	-7.45	10.498	432	320	-17.2	-82.4	-99.6	199.3	-1.0

Table 12.2: Load confirmation based on exciter registration.

The majority of the picture analysis is conducted in the pixel domain. The region of interest is defined as starting at the notch (c_x). However, this location differs for the different series due to slight differences in the relative position of the specimen relative to the camera. In addition, the crack path is constrained to the defined x-axis requiring the specification of the y coordinate of crack (c_y) and the angle under which it propagates. The angle is obtained by looking at later images in the series with a large visible crack and is defined according to the axis system in 8.1. Furthermore, pixel size is required to translate the obtained results into their relevant SI units. This size can be determined by the number of pixels between the notch and the end of the specimen ($c_x - end$), because this distance is defined for the CT specimens as 54 mm ($W - a_n$). All these properties as used in the analysis of the CT specimen series are presented in table 12.3.

	c_x [pixel]	c_y [pixel]	end [pixel]	pixel size [mm]	angle [degrees]
Serie 1	1030	2870	8430	7.30E-03	6.4
Serie 2	1018	2870	8440	7.28E-03	6.3
Serie 3	1055	2955	8456	7.30E-03	-3.8
Serie 4	1150	2790	8602	7.25E-03	0
Serie 5	990	2572	8632	7.07E-03	-2.3

Table 12.3: Image specific parameters.

In an additional effort to confirm the loading condition, it was also tried to obtain the structural stress from the DIC results. A few possibilities were investigated in this regard. First of all, from mapping the special basis function in the two-step or one-step approach, the stress field amplitudes are directly obtained. If a linear far-field stress distribution is used, these amplitudes directly relate to the structural stress, which method works when a far-field is analyzed. However, in the case of the CT specimen, the region of interest is notch affected, meaning a linear far-field distribution will not be able to describe the stress field. Therefore a different method is required. The second proposed method was to use the two-step FEM-based DIC. The obtained displacement field is similar to FEM due to the nature of its procedure. The nodal forces should follow by establishing the stiffness matrix and multiplying these with the DIC-obtained nodal displacements. From that point, the procedure is analogous to FEM and can be used to determine the structural stress. However, a few issues have to be considered. First, the evaluated field should only cover a single side of the field. Otherwise,

the sum of the Forces should constitute zero, as $K * u$ provides only provides the external forces. Secondly, rigid body motions should not be taken into account as these would not cause any stress in the material. In a FEM model, these movements would be constrained. However, due to the possible movement of the camera with respect to the specimen, it is not eliminated during a FEM procedure. This effect is prevented by evaluating a substantial region and removing the mean of the displacements.

The stiffness matrix can be described on a local element level, and because the elements are defined as a square grid, no iso-parametric mapping (Zienkiewicz & Taylor, 2000) is necessary.

$$K_e = tp \cdot \int \int \mathbf{B}^T \mathbf{D} \mathbf{B} dA \tag{12.7}$$

The elasticity matrix (Zienkiewicz & Taylor, 2000) is defined according to the assumed plane stress condition, following from DIC being a surface measurement tool.

$$\mathbf{D} = \frac{E}{1 - \mu^2} \cdot \begin{bmatrix} 1 & \mu & 0 \\ \mu & 1 & 0 \\ 0 & 0 & \frac{1-\mu^2}{2(1+\mu)} \end{bmatrix} \tag{12.8}$$

Furthermore, the strain–displacement matrix (Zienkiewicz & Taylor, 2000) can be readily defined by considering the derivatives of the shape function with respect to the local x and y directions. It should be noted that the nodal order of the shape function derivatives is essential in this step, as it should correspond to the displacement vector in order to obtain the proper nodal forces.

$$\mathbf{B} = \begin{bmatrix} -\frac{1}{4}(1-y) & 0 & \frac{1}{4}(1-y) & 0 & \frac{1}{4}(1+y) & 0 & -\frac{1}{4}(1+y) & 0 \\ 0 & -\frac{1}{4}(1-x) & 0 & -\frac{1}{4}(1+x) & 0 & \frac{1}{4}(1+x) & 0 & \frac{1}{4}(1-x) \\ -\frac{1}{4}(1-x) & -\frac{1}{4}(1-y) & -\frac{1}{4}(1+x) & \frac{1}{4}(1-y) & \frac{1}{4}(1+x) & \frac{1}{4}(1+y) & \frac{1}{4}(1-x) & -\frac{1}{4}(1-y) \end{bmatrix} \tag{12.9}$$

The local stiffness matrix has been integrated following the two by two Gauss method. Were the integration is performed by calculating the values at the points: $(x = -\frac{1}{\sqrt{3}}, y = -\frac{1}{\sqrt{3}})$, $(x = -\frac{1}{\sqrt{3}}, y = \frac{1}{\sqrt{3}})$, $(x = \frac{1}{\sqrt{3}}, y = -\frac{1}{\sqrt{3}})$, $(x = \frac{1}{\sqrt{3}}, y = \frac{1}{\sqrt{3}})$, and calculating its sum with the weights of 1. Furthermore, a correction is required for the element size, as the element has a size of 2 by 2 in the normalized local reference frame, however in actuality the element size is 32 by 32 pixels which is a certain size in mm dependent on the series pixel size. This correction can be performed through a pre multiplication.

Following the global system can be established. Following the indexing from the FEM-based DIC, a sparse global K matrix can be established, and by multiplying the displacements the nodal forces are determined. However, afeter employing this method it was observed that the nodal forces remained to fluctuate around zero as can be seen in Fig. 12.1, Whilst at the zero y coordinate a large force is expected due to the notch effect.
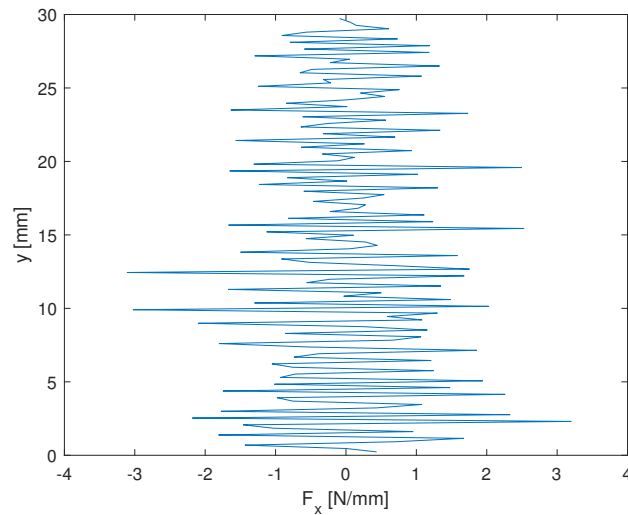
Figure 12.1: Nodal Forces obtained from Serie 5 by a FEM-based DIC displacement field.

Because, the nodal force method did not provide satisfactory results further investigation was conducted. Instead of a calculation from the nodal forces a calculation from the stresses could also be conducted. The strains can be obtained from by determining the gradients of the displacement field. When the one-step fem based approach is used the gradients show a large amount of variation over the thickness (Fig. 12.2). These variations are caused by the fact that linear shape functions are used. Meaning the displacement field is only C^0 continuous.
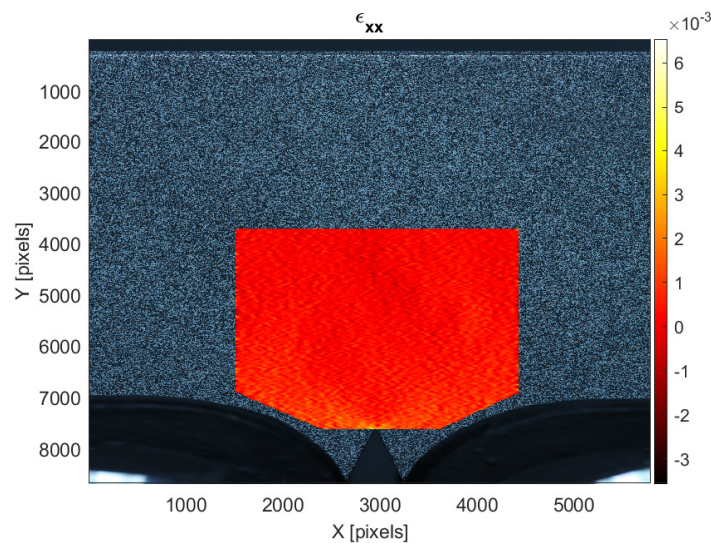
Figure 12.2: The strain in horizontal direction from the first image of Serie 3 obtained by FEM-based DIC.

Because the strains are not continuous and and the stresses follow from a matrix multiplication with the elasticity matrix the stress are also not continuous as can be seen in Fig. 12.3.
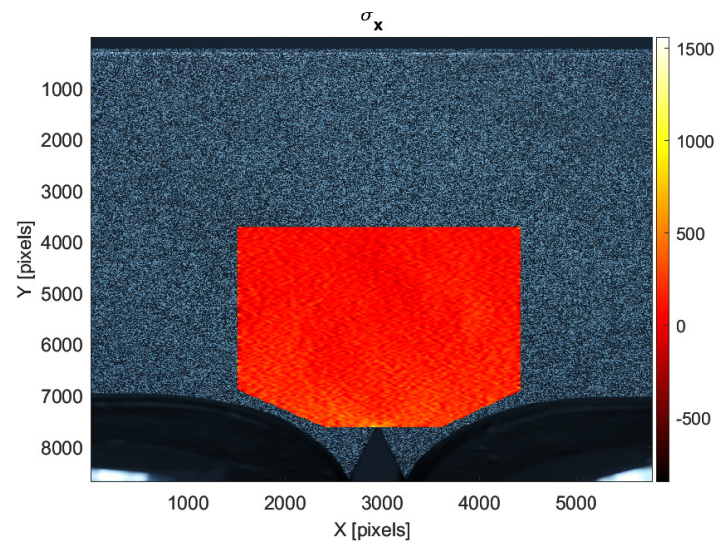
Figure 12.3: The stress in horizontal direction from the first image of Serie 3 obtained by FEM-based DIC.

The Effect of these variations can be better observed when looking at the trough-thickness distribution up from the notch. In Fig. 12.4 a high peak stress at the notch can clearly be observed and a general bending contributions can be observed. However, calculating the structural stress based on this distribution might be less accurate due to these fluctuations. Therefore it was chosen to analyse the structural stress based on the one-step DIC procedure. Because this procedure enforces a global basis function ensuring a higher order of continuity.
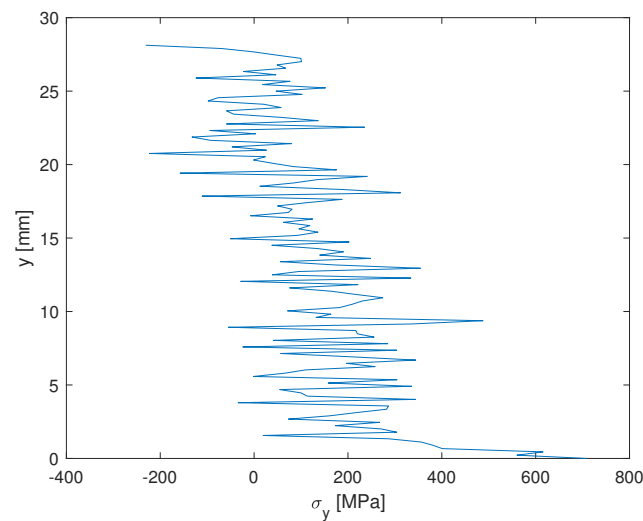
Figure 12.4: The stress along the crack path from the first image of Serie 3 obtained by FEM-based DIC.

When employing the gradients based on the one-step, the higher order of continuity can be clearly observed (Fig 12.5). Additionally, a notch effect becomes apparent, leading to a reduction in the overall visibility of the stress field, primarily attributable to the high peak values.
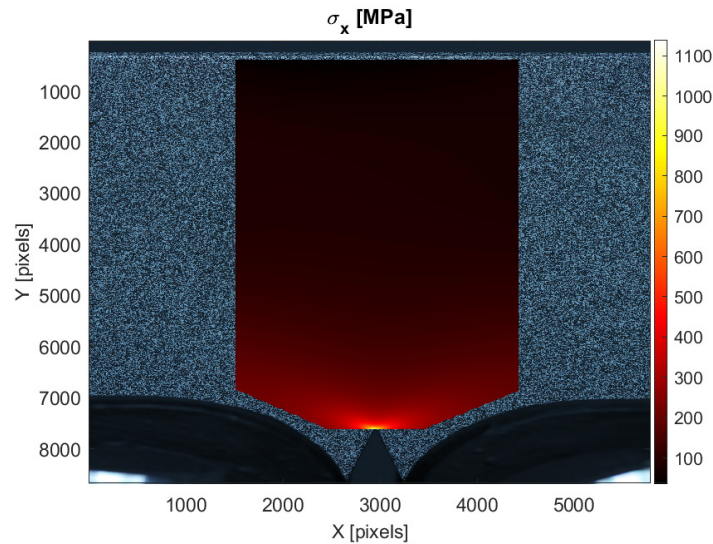
Figure 12.5: The stress in horizontal direction from the first image of Serie 3 obtained by one-step DIC.

Extracting the stress along the crack path allows for the determination of the structural stress following the procedure from section 2.2. With the obtained membrane and stress component, the fictitious far-field stress distribution is obtained (Fig. 12.7). Comparing the two distributions, a clear notch affected region can be observed, as well as a self-equilibrating part.
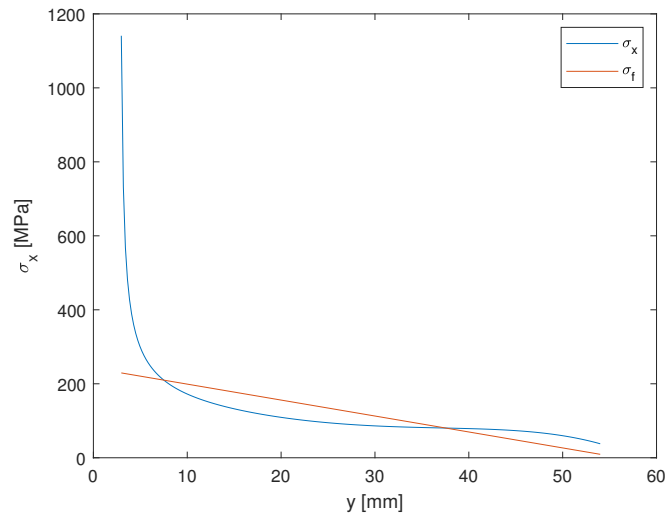

Figure 12.6: The stress along the crack path from the first image of Serie 3 obtained by one-step DIC.

This procedure can be repeated for all five series. The first image is taken each time with the crack size set to zero and 13 William's terms starting at -1. In Tab. 12.4, it can be seen that the structural stress for each of the evaluated cases is higher than the expected outcome from the calculation following force and moment equilibrium. A slight difference could be expected as the assumed Young's modulus of 210 GPa and Poisson ratio of 0.3 could differ slightly. However, this is not expected to cause such a large discrepancy. An additional concern is the plane stress assumption, which is assumed to be valid for the DIC as it is a surface measurement. However, combined with some subsurface effects, it could cause some differences. Lastly, the Williams solution is generally employed to describe the notch region. Although the self-equilibrating stress seems to be captured, it possibly induces some discrepancies outside the notch region.

	σ_m	σ_b	σ_s	$\sigma_{s,expected}$
Serie 1	104	318	423	334
Serie 2	161	275	437	334
Serie 3	116	113	229	200
Serie 4	92	114	207	150
Serie 5	87	72	159	100

Table 12.4: Structural stresses obtained from one-step DIC

In order to confirm that the problem is not caused by the Williams terms, not being able to capture the far-field region properly, the residual error plot was investigated. No clear increase in error away from the notch is observed with the 13 considered terms.
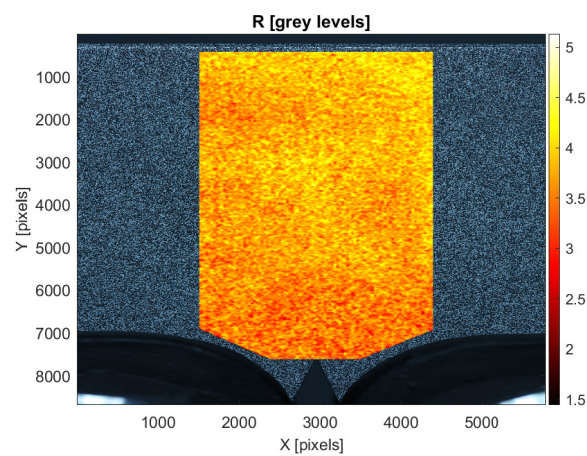
Figure 12.7: The grey level residual of the one-step DIC for the first image of Serie 3

12.2. Texture quality

When employing the one-step approach, the texture quality of the image remains essential. First, the grey scale levels of the reference images of the different tests have been evaluated. It should be noted that only the region of interest is considered, meaning that any peak at the low end of the grey scale is entirely due to the dark points of the specimen and not the result of the dark background.
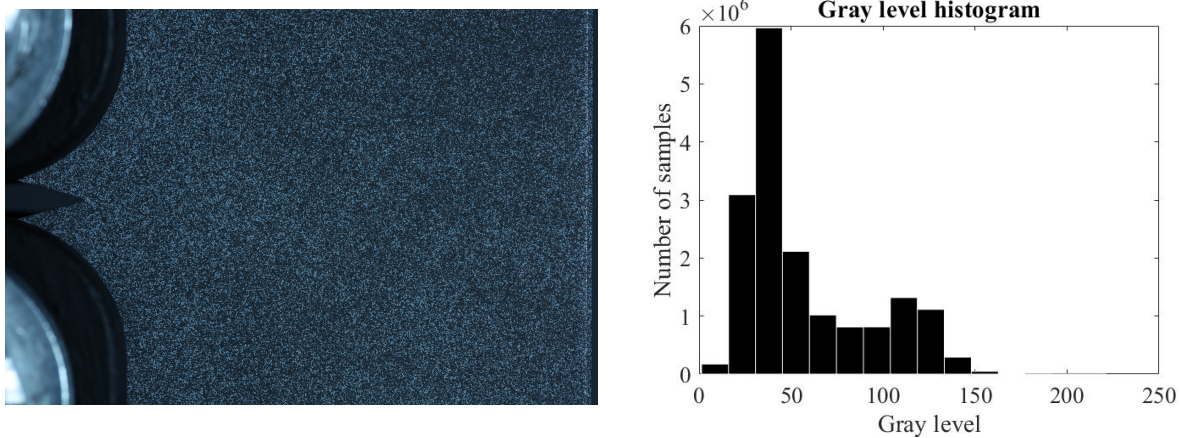

Figure 12.8: Serie 5 reference image (left) and grey-level distribution (right)
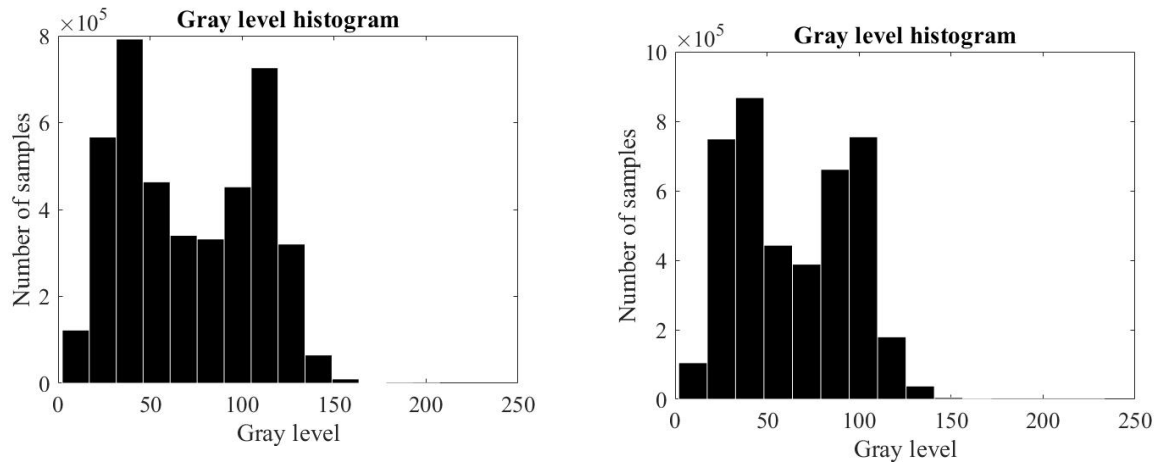
Figure 12.9: Grey-level distribution Serie 1 (left) and grey-level distribution Serie 2 (right)
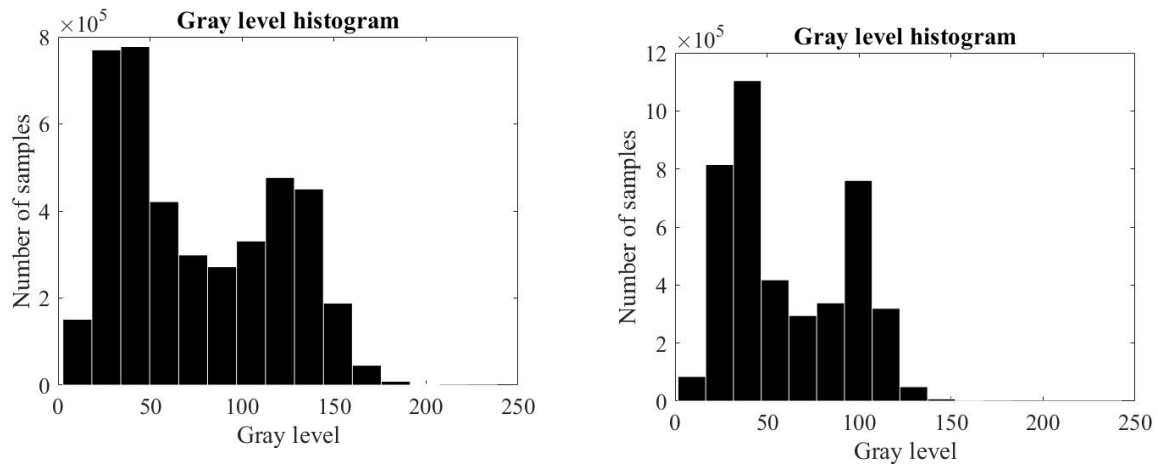

Figure 12.10: Grey-level distribution Serie 3 (left) and grey-level distribution Serie 6 (right)

From all the grey-level images, it can be seen that only part of the camera's full dynamic range is used. This partial use is most likely caused by the metal clamping, which is very reflective, causing a large part of the dynamic range to be consumed by this part of the image. Furthermore, it can be observed that there are two general peaks in the grey-scale level. This is expected as the applied speckle pattern consists of two opposite pigments with a normal distribution around them. However, for Serie 5, the distribution does not seem to be nicely distributed. This could cause problems during the correlation procedure, as the best result is reached with a wide, normally distributed grey-scale, which ensures uniqueness.

Secondly, because the multi-scale algorithm employs an element scheme in order to determine gradients, it is crucial to determine the element size at which accurate determination takes place. The same procedures used in the two-step FEM-based method can be utilized. By doing so, the correlation radi and the fluctuation criteria can be obtained, which are essential in the assessment process. Compared to the two-step approach, a notable advantage is that enlarging the element size within the Zone of Interest (ZOI) does not lead to a loss of resolution because the amplitudes are utilized to describe the global field effectively.
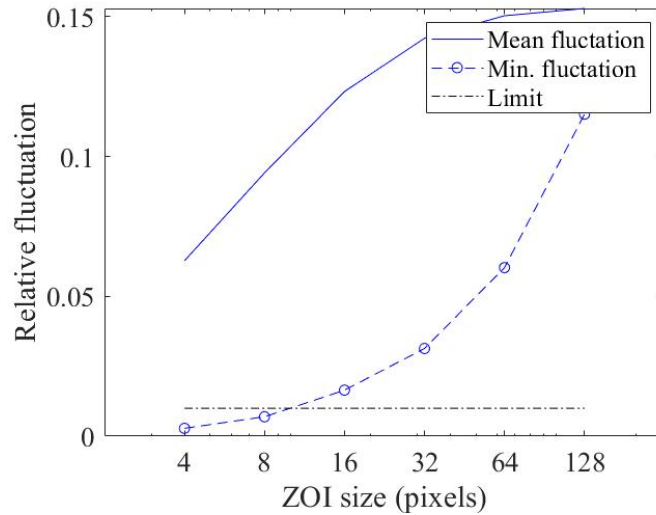
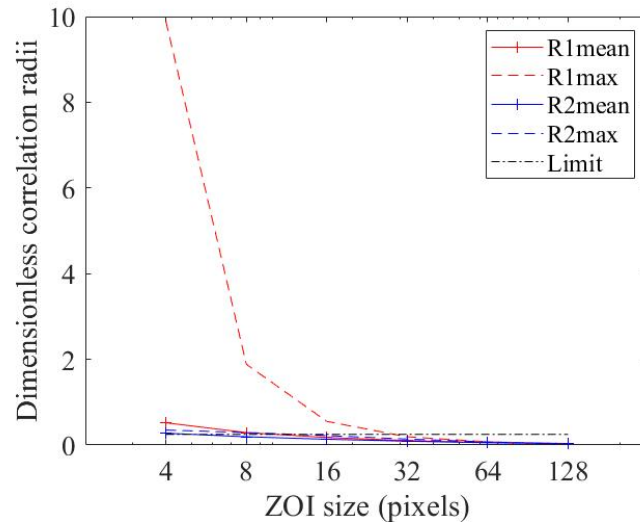Figure 12.11: Representative fluctuation for all series

Figure 12.12: Representative correlation radii for all series

The images for all the different series have been analysed, resulting in indistinguishable results. Therefore, the same element size can be used for all the series. Based on the analysis of fluctuation criteria, it becomes evident that the element size should be no less than 16 by 16 pixels. However, when examining the correlation radii, the situation is more nuanced. While the mean correlation radii are adequate at 16 by 16 pixels in size, the maximum radii in the R1 direction (which corresponds to the direction normal to the crack propagation) only meet the requirements at a size of 32 by 32 pixels.

Since resolution plays a relatively minor role in this application, the larger size of 32 by 32 pixels is chosen to ensure sufficiency. This size ensures that the algorithm performs optimally, capturing the necessary details for the crack propagation analysis.

12.3. Local two-step FEM-Based approach
Similar to the Reference specimen, the CT specimen can be analysed with the two-step FEM-based approach. Following the texture analysis, an element size of 32 by 32 pixels is chosen. Initially, no masking was employed. However, this presented stability issues in the case of the crack tip determination procedure, resulting in a mask being introduced.
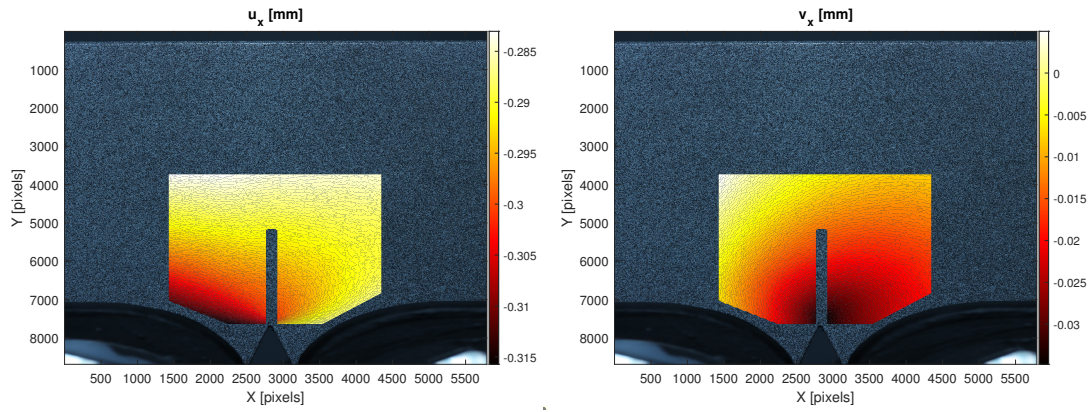
Figure 12.13: Horizontal (left) and vertical (right) displacement field, from first image of Serie 1. Obtained by FEM-based DIC.

In the post-processing step of the two-step approach, William's series formulation in polar coordinates is employed as the special basis function (Eq. 3.37). The lowest included term was the singular -1 term, and in total, 13 terms were used (n=13).
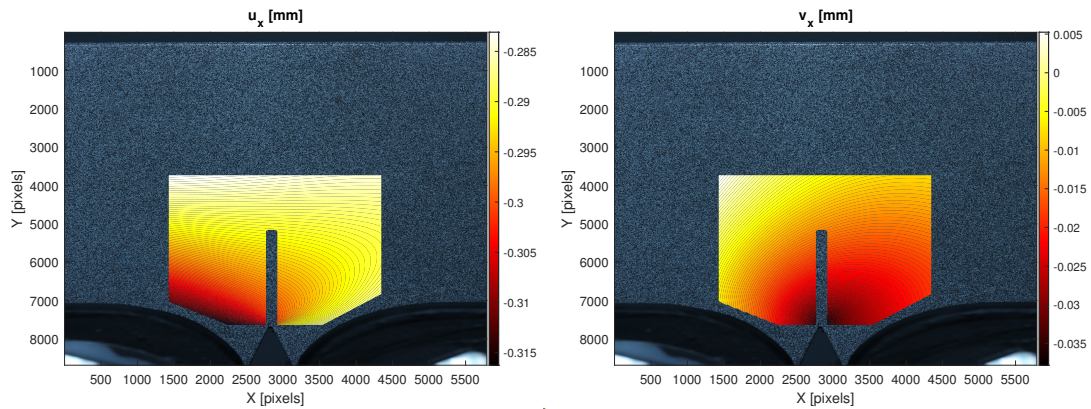

Figure 12.14: Post-processed horizontal (left) and vertical (right) displacement field, from first image of Serie 1.

The obtained continuous fields show good correspondence with the discrete field. A crack growth relation can be established when analysing the entire series of images and using the singular amplitude method to determine the crack-tip locations.
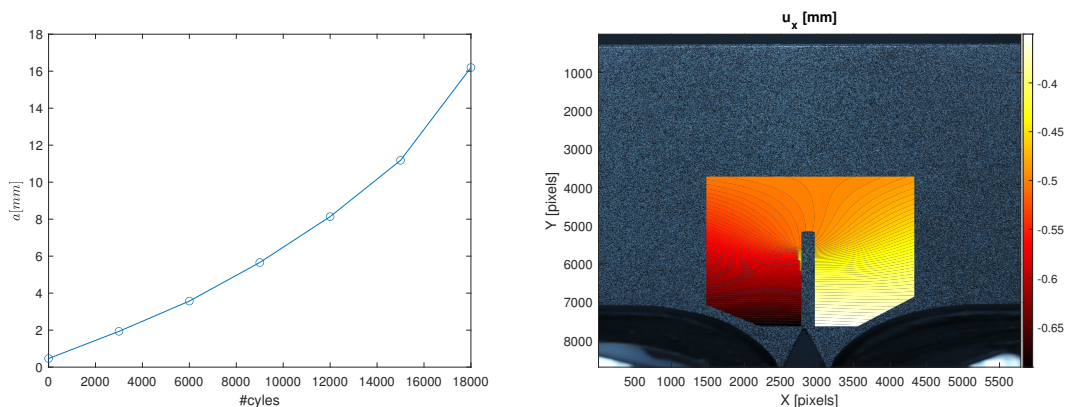

Figure 12.15: Displacement field of last image of Serie 1 (left) and Serie 1 crack growth relation (right).

The obtained crack growth relation for Serie 1 shows the expected exponential growth behaviour. However, from the field obtained for the last image in the series, it can be seen that the crack falls outside the masked

region. Considering the decrease in stability, which has been observed when the crack tip is not masked, this could decrease the determination's accuracy. Therefore, the masking in the one-step global DIC approach will be angled to align with the crack propagation.

Besides the crack tip location, the Stress Intensity Factor (SIF) can also be determined from the amplitudes of the obtained displacement field. In total, 26 amplitudes have been obtained because each of the 13 William's terms has a corresponding mode 1 and 2 contribution. The fifth amplitude, corresponding to the first-order term, multiplied by the shear modulus, provides the mode 1 SIF. Furthermore, to obtain the SIF range, the value can be corrected with the remote mechanical loading ratio ($\Delta K_1 = K_1 \cdot (1 - r_{lr})$). In the case of Serie 1, this corresponds to a correction factor of 0.9.
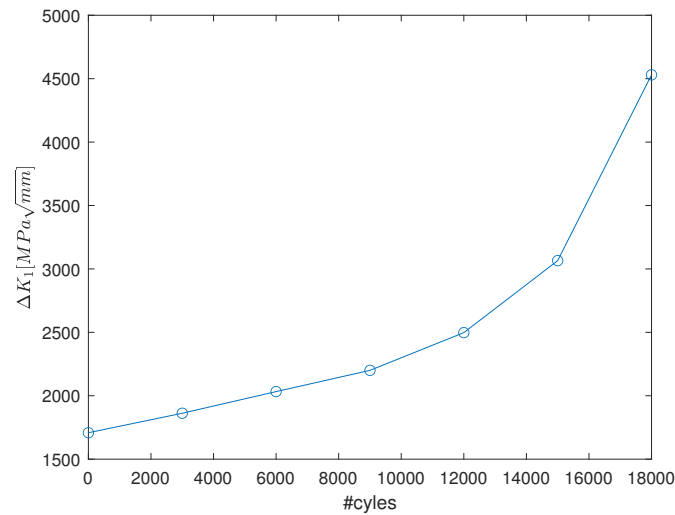

Figure 12.16: Mode 1 SIF of Serie 1 obtained with two-step FEM based DIC.

12.4. Global one-step approach

The Global one-step DIC approach was established for the different series. In order to compare the displacement fields with those obtained from the two-step FEM-based approach, the obtained displacement fields from the first image of Serie 1 are presented. The presented displacement fields were obtained with the same 13 William's terms as employed in the two-step approach.
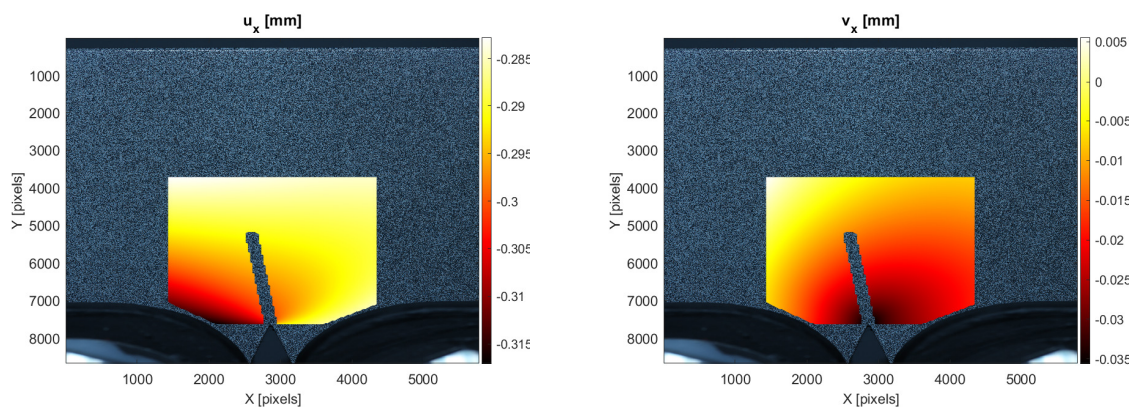

Figure 12.17: Horizontal (left) and vertical (right) displacement field, from first image of Serie 1. Obtained with one-step DIC

The obtained fields clearly correspond to those obtained with the two-step FEM-based approach.

12.4.1. Convergence study

When employing the William's solution, an additional concern is the amount of series terms which have to be taken into account in the analysis. An increased number of terms could increase accuracy by providing a more complete displacement field description. However, an increasing amount of terms increases the computational time. Additionally, the number of unknowns in the linear system provides an upper bound for the number of terms which can be included, which might be considered significant due to the generally high pixel resolution. However, the amount of unknowns is defined by the number of elements, and when employing a multi-scale algorithm, this criterion has to be satisfied at the largest employed scale, significantly reducing the system's size. Alternatively, arbitrarily enlarging the region of interest does not generally overcome this issue. Because a larger region of interest typically increases the number of terms required to describe the field. In addition, it results in an even greater computational time increase.

However, by starting at the smallest crack and making use of the results of previous images in a series, the amount of multi-scale terms can be reduced. Due to the initial guess, which mitigates large displacement issues requiring the multi-scale procedure.

In order to determine the required amount of terms, a convergence study has been conducted. For all experiments, a region of interest extending 1500 pixels to either side of the notch and 4000 pixels in length was evaluated. A mask of 150 pixels in width and 3500 pixels in length was employed, angeled in line with the crack propagation direction. One in every ten available pictures in the series has been analysed to reduce the computational load while keeping the general overall series behaviour.

Two different parameters have been investigated in the convergence study. The crack-tip location and the first mode-related SIF parameters were chosen as these variables, combined with the known amount of cycles, completely define the crack growth relation, which has to be validated. The figures presented below show these parameters for different amounts of Williams term; the lowest term for all analysis is the singular -1 term, and the varying parameter n defines the total amount of terms. The analysis requires at least three terms to define the crack tip location and the SIF. However, a stable analysis was only reached at five terms and is, therefore, the lowest number of included terms in the convergence study. The instabilities at the lower amount of terms can be explained due to the exclusion of the T-stresses, which are non-vanishing stresses and argued to represent the constraint of the crack tip (Bouledroua et al. 2016), and the relatively large size of the analysed notch region.
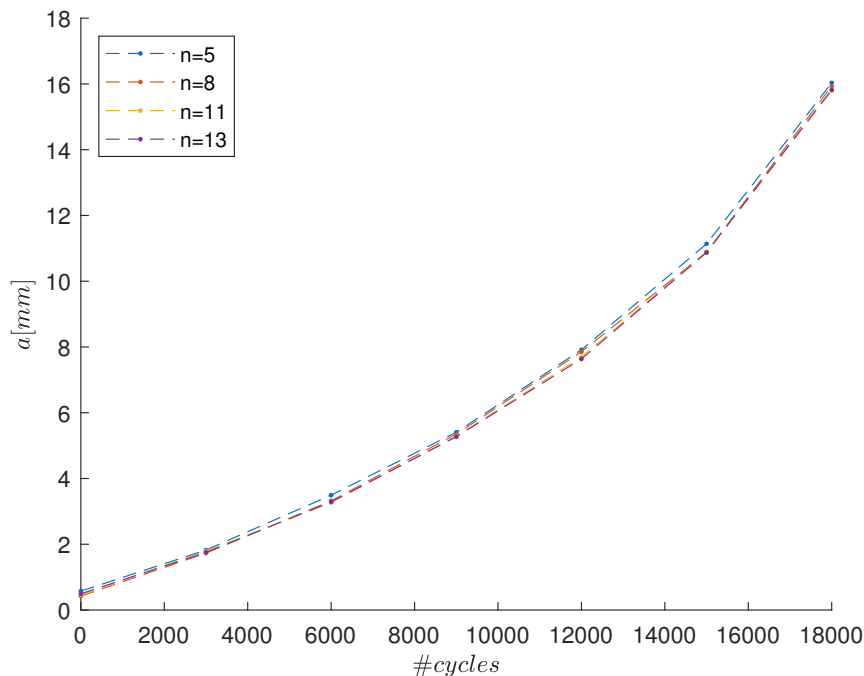

Figure 12.18: Convergence of crack size dependent on amount of William's terms of Serie 1.
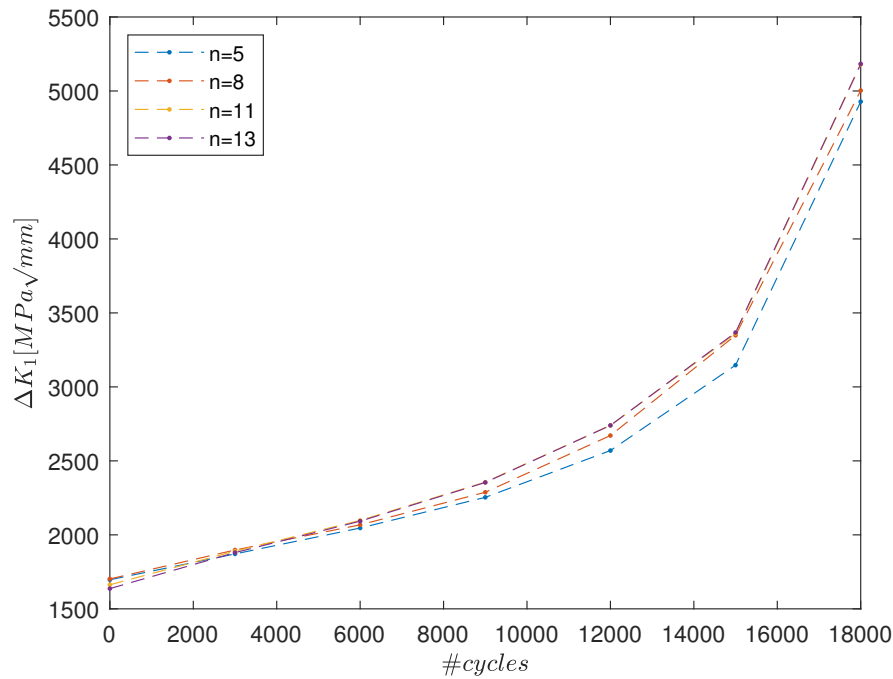
Figure 12.19: Convergence of mode 1 SIF dependent on amount of William's terms of Serie 1.

For Serie 1, it can be observed that the crack-tip location does not vary significantly based on the amount of William's terms. Convergence is already reached at $n = 8$. However, when observing the mode 1 SIF, a larger deviation can be observed when comparing different amounts of included terms. Especially at the larger crack sizes, a lower amount of terms seems to underestimate the SIF. With eleven terms, the SIF is slightly underestimated for the first image, but for subsequent images, it perfectly overlaps with the result at thirteen terms.

Additionally, the results of Serie 1 can be compared to those obtained from the two-step FEM-based approach (Fig.12.15, 12.16). The results align in general reasonably well. However, only the final SIF value of the series is significantly smaller in the post-processing approach. However, this could be explained due to the crack tip exiting the masked region.

Figure 12.20: Convergence of crack size dependent on amount of William's terms of Serie 2.

Figure 12.21: Convergence of mode 1 SIF dependent on amount of William's terms of Serie 2.

The convergence behaviour of Serie 2 can be observed to be similar to the Serie 1, which is expected as the applied loading in both cases was the same.
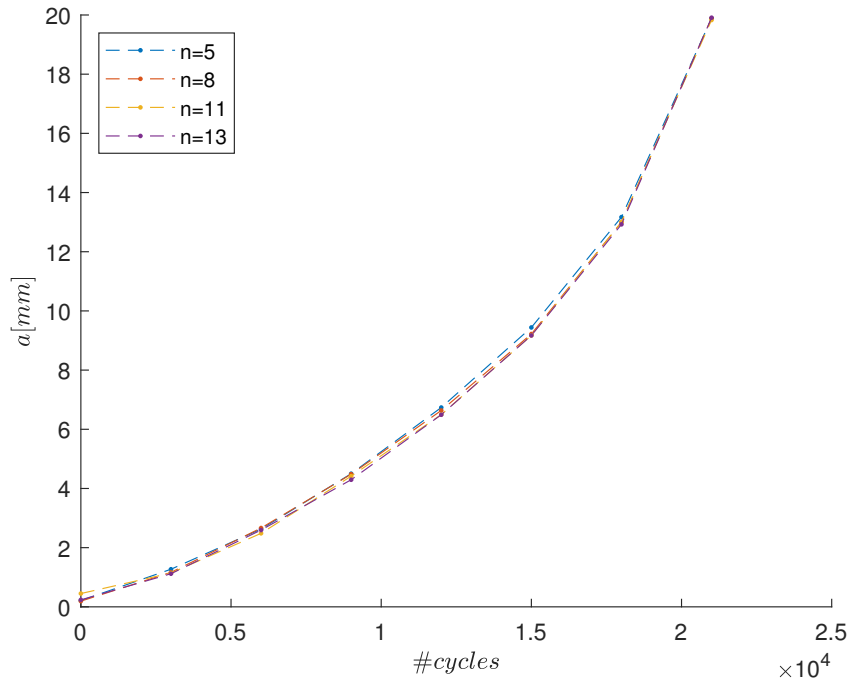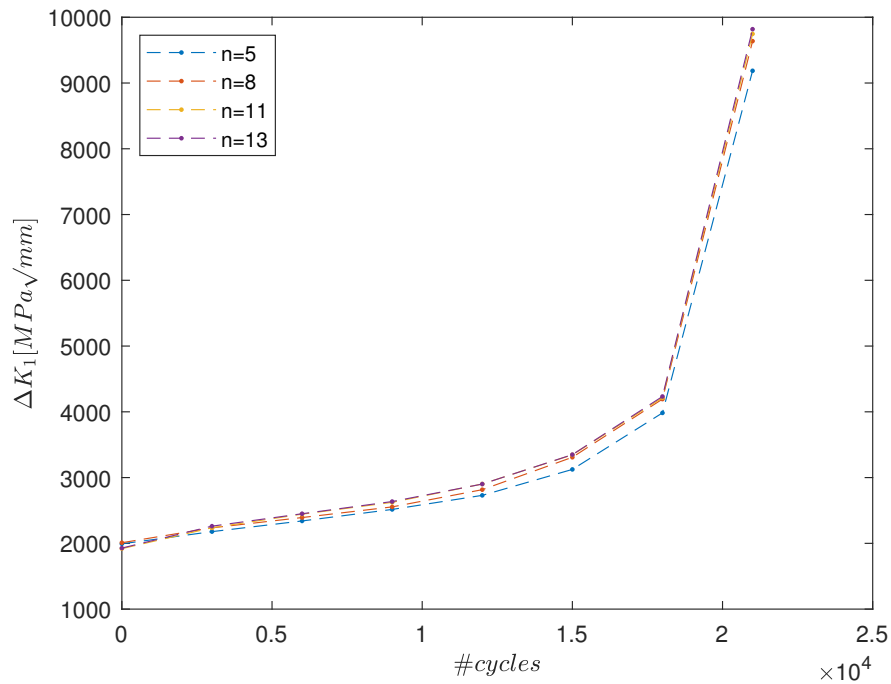
Figure 12.22: Convergence of crack size dependent on amount of William's terms of Serie 3.
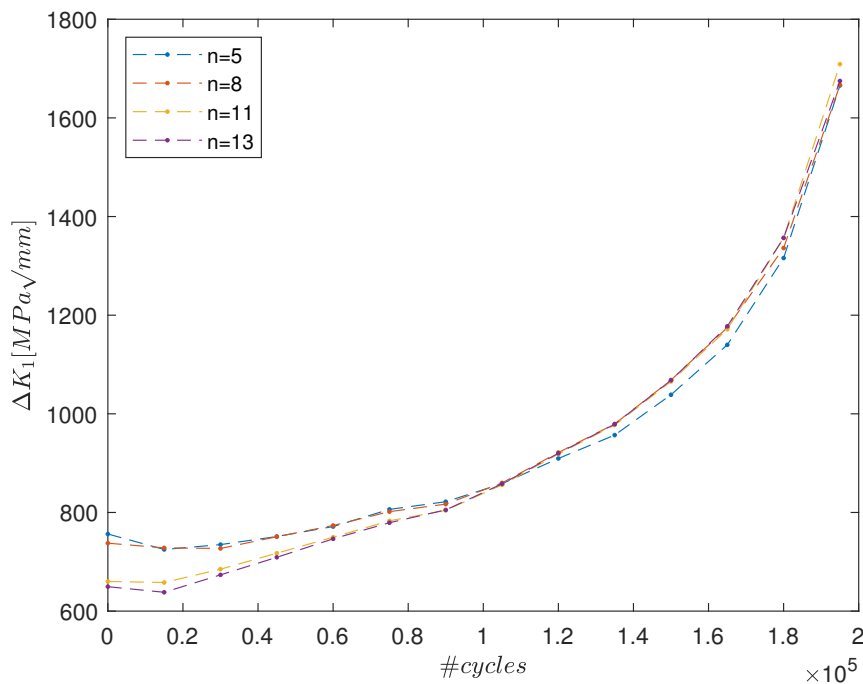
Figure 12.23: Convergence of mode 1 SIF dependent on amount of William's terms of Serie 3.

Similar to Serie 1 and 2, the crack tip location showed a minimal difference between the different amounts of included terms. However, a different behaviour can be observed when analyzing the SIF. Firstly, the general values are significantly lower compared to the previous series. However, this is expected, as the applied stress range is significantly lower. Additionally, it can be well observed that the lower amount of terms initially

overestimates the SIF and, at larger crack sizes, underestimates the SIF value. Furthermore, a larger difference between eleven and thirteen terms can be seen compared to the previous series, although the absolute difference is smaller due to the lower SIF.
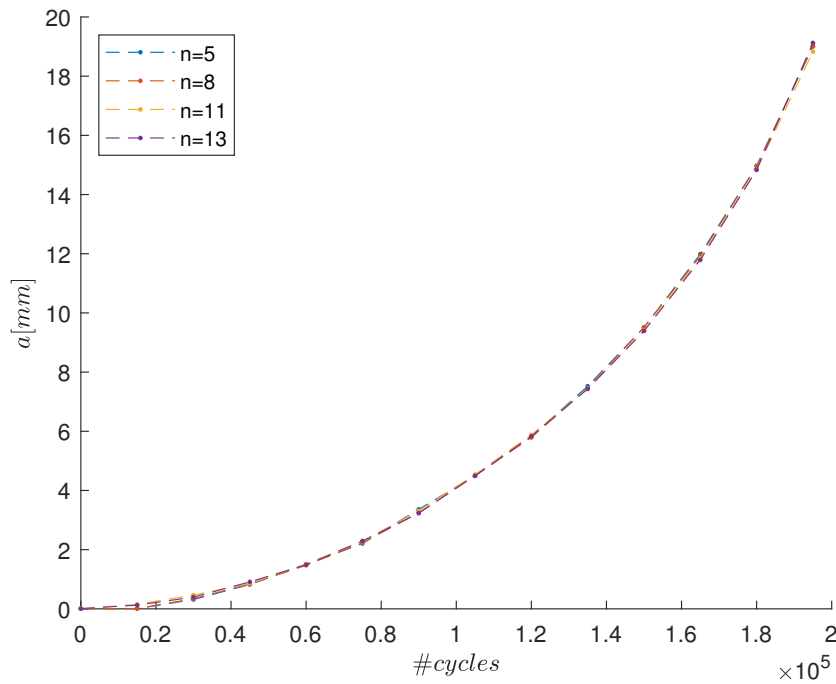

Figure 12.24: Convergence of crack size dependent on amount of William's terms of Serie 4.
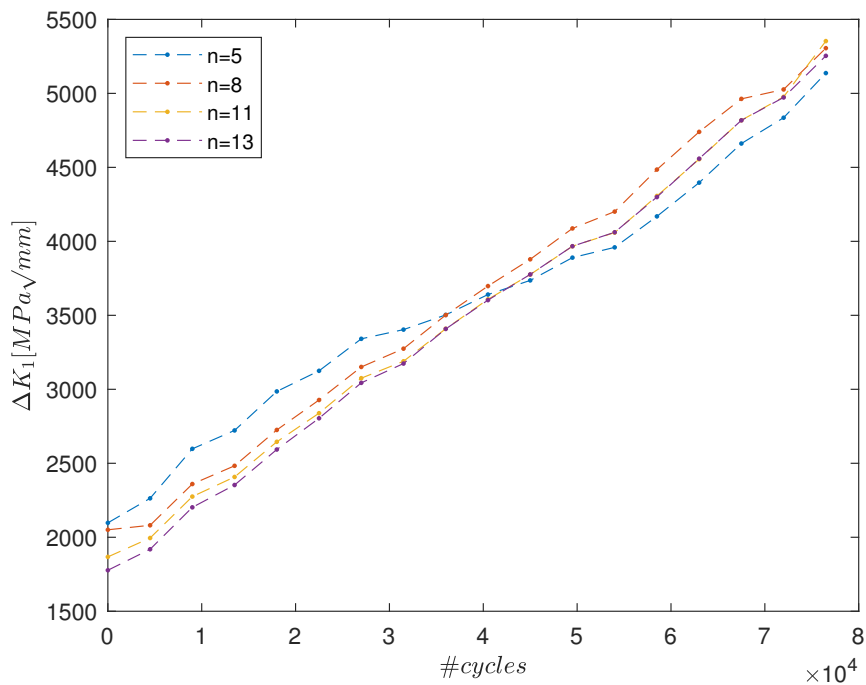
Figure 12.25: Convergence of mode 1 SIF dependent on amount of William's terms of Serie 4.

In contrast to the previous series, Serie 4 exhibits worse convergence in both crack-tip behaviour and SIF

analysis, requiring 13 terms to achieve convergence. Another observation that can be made is caused by the mechanical load ratio. Given that the stress range remains consistent with the first two series, a comparison can be made. It becomes evident that the initial SIF range remains nearly identical, an expected outcome considering its dependency on stress range. However, in subsequent images, a gradual increase in offset with those series can be observed, which can be attributed to the decelerated crack growth at a negative load ratio.
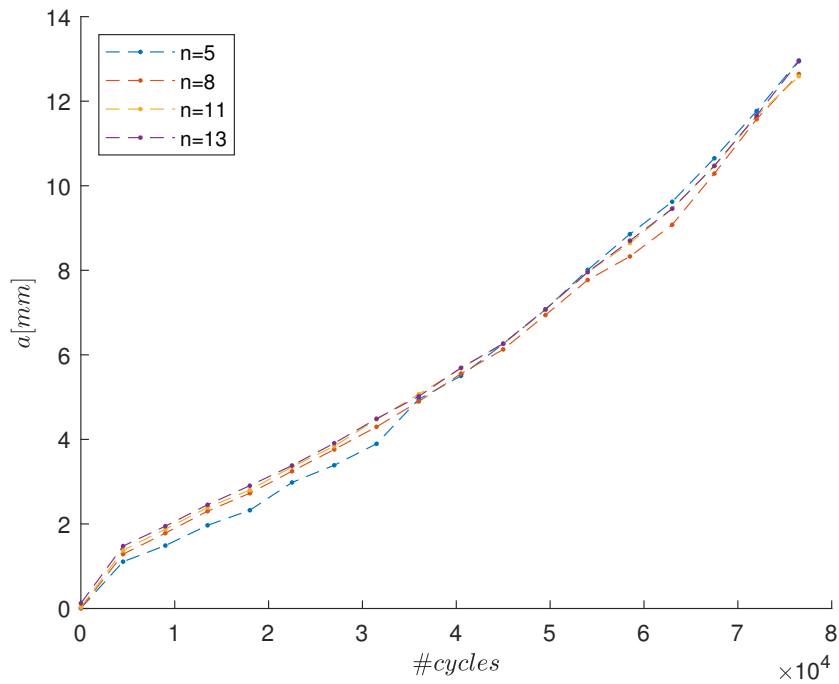

Figure 12.26: Convergence of crack size dependent on amount of William's terms of Serie 5.

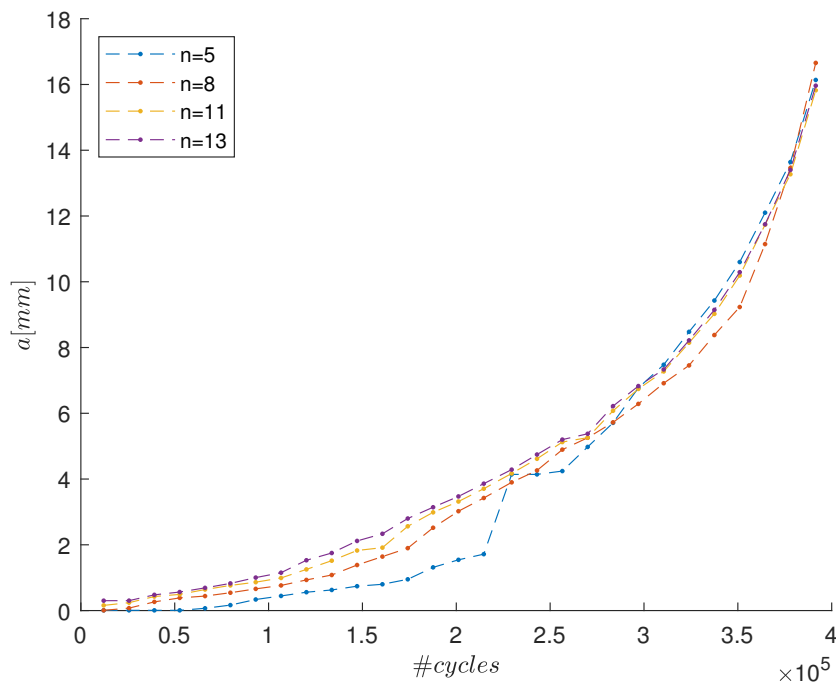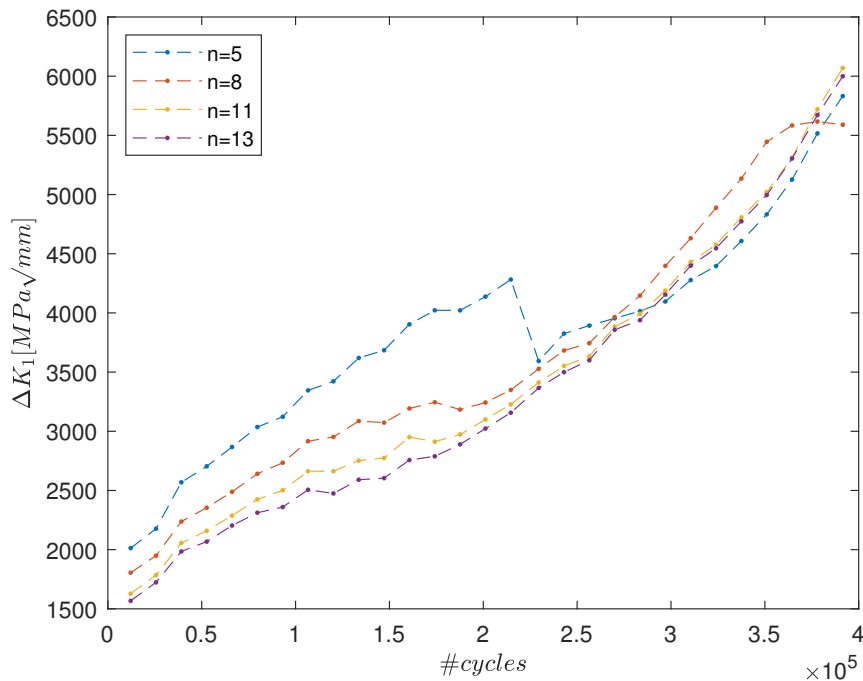Figure 12.27: Convergence of mode 1 SIF dependent on amount of William's terms of Serie 5.

Serie 5 shows overall the same convergence behaviour as Serie 4. However, it also shows some interesting behaviour at lower truncations. With a considerable overestimation for the lower amount of terms, with only five included terms, and the flattening of the SIF at the end of the series with eight terms. Additionally, it reinforces the idea that 13 terms are required in order to achieve convergence

From the combined convergence studies, it can be concluded that the crack-tip location is generally significantly less affected by the amount of William's series taken into account than the SIF. This difference is possibly caused by the crack tip estimate being determined by the ratio of two amplitudes. Because when fewer terms are taken into account, the residuals of these terms affect both terms, which their division possibly cancels out. In addition, even if this is not entirely the case, rudimentary, even at a lower amount of terms, the actual crack-tip location should still provide the best fit to minimise the singular term, which is the purpose of the applied crack-tip determination method. Taking into account fewer terms would, in such cases, increase uncertainty and therefore spread around the expected location. Whilst for a single amplitude value, taking fewer terms could result in compensation behaviour, resulting in off-sets in the amplitude value.

12.4.2. Potential drop measurement comparison
The data obtained with the Global one-step DIC procedure can be compared to the results obtained through the potential drop measurements. However, the potential drop measurements do not provide stress field data. Therefore, in order to compare the crack growth data in the format where it is set out against the SIF range, the SIF needs to be determined according to the analytical formulations, similar to the parameter determination (Sec. 9.2). Based on the results of the convergence study, it was chosen to take the values at 13 Williams terms for all the series. Due to computational time and time constraints, the same amount of images are analysed as in the convergence study. This reduced number of data points resulted in the window of the Savitsky-Golay filter needing to be decreased compared to the procedure described in section 9.1, in order to align with the amount of data points. In addition, it was observed that more than five terms in the filter resulted in overfitting, resulting in the choice of 4 terms.

Crack size
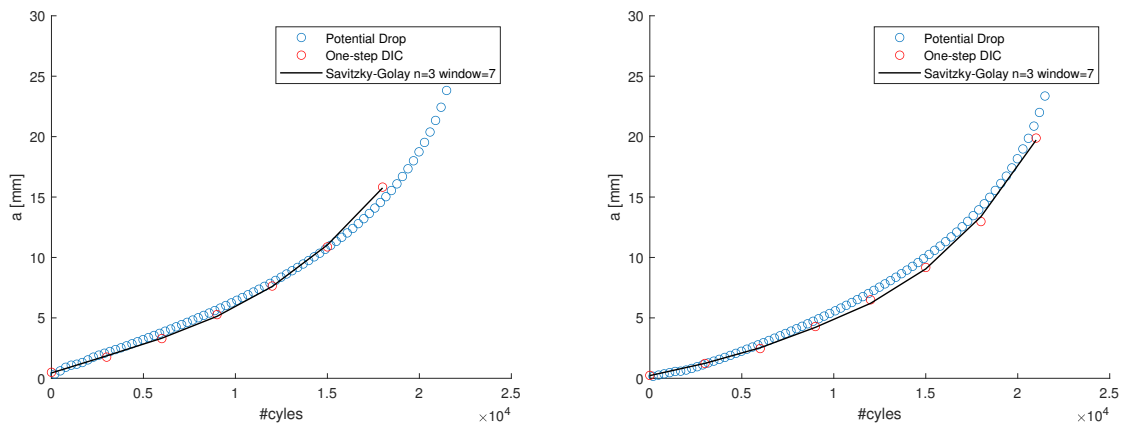
Figure 12.28: Comparison between the one-step DIC (n=13) and Potential drop obtained crack size, Serie 1 (left) and Serie 2 (right).
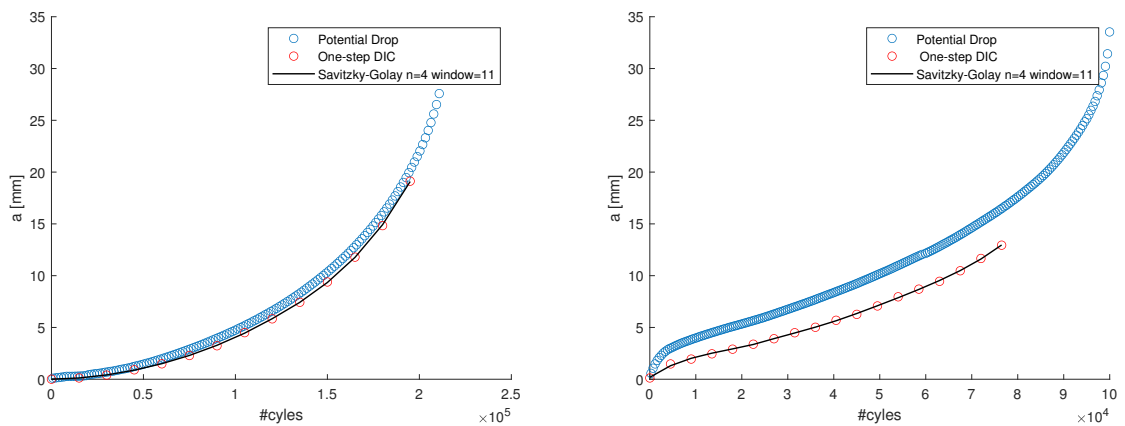
Figure 12.29: Comparison between the one-step DIC (n=13) and Potential drop obtained crack size, Serie 3 (left) and Serie 4 (right).
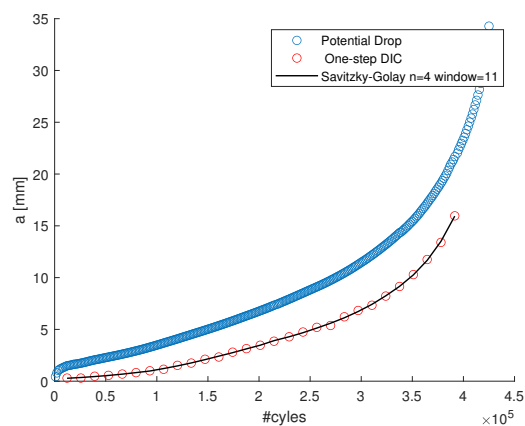
Figure 12.30: Comparison between the one-step DIC (n=13) and Potential drop obtained crack size, Serie 5.

The comparison shows that the crack sizes obtained by global one-step DIC aligned well with the potential drop results for the first three series. However, the crack size obtained with Potential drop is significantly larger

for the last two series with a load ratio of -1. The main difference observed in the initial growth stage is that the potential drop-based crack grows quicker before settling in. Besides the initial stage, the DIC data shows the same growth pattern, resulting in a general offset for the rest of its lifetime.

Crack growth

Following the procedure as outlined in section 9.1, the crack growth relation can be compared with the potential drop results. Notably, the last two series could exhibit alignment with the potential drop data within the context of crack growth. This difference would be explained due to crack growth not being a cumulative value and, therefore, not being affected by the disparity observed in the initial growth stage.
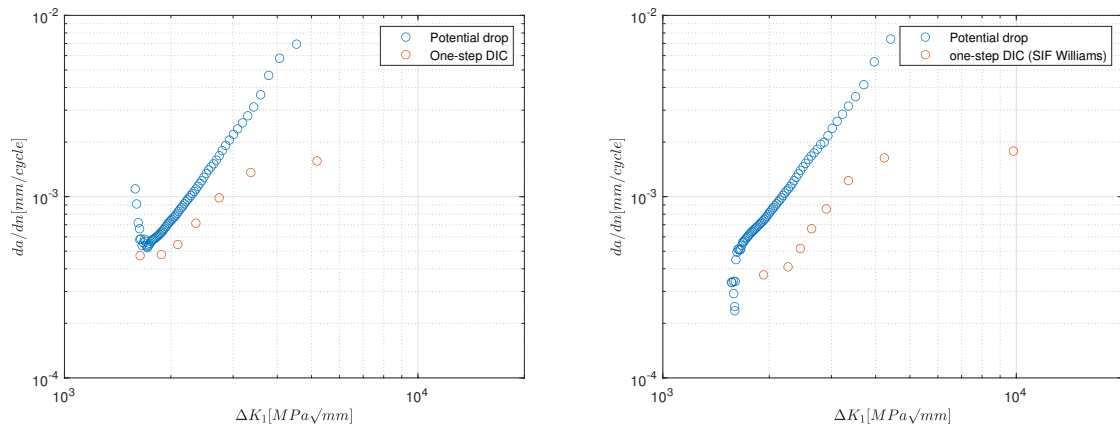

Figure 12.31: Comparison between the one-step DIC (n=13) and Potential drop obtained crack growth, Serie 1 (left) and Serie 2 (right).
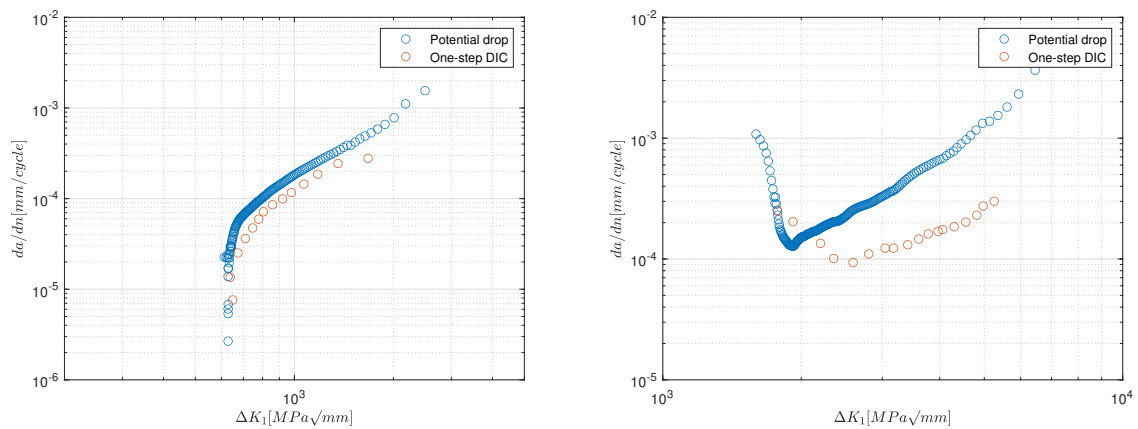

Figure 12.32: Comparison between the one-step DIC (n=13) and Potential drop obtained crack growth, Serie 3 (left) and Serie 4 (right).
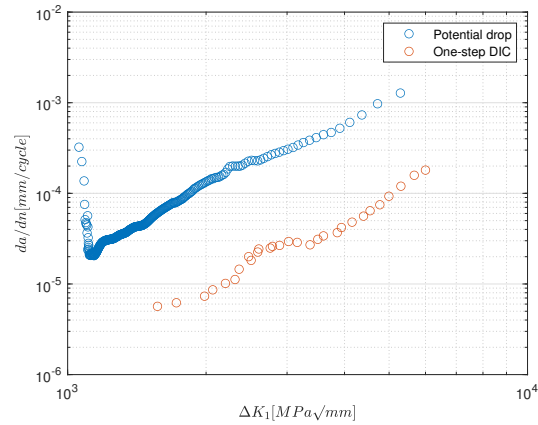
Figure 12.33: Comparison between the one-step DIC (n=13) and Potential drop obtained crack growth, Serie 5.

Interestingly, it can be observed that four of the five series seem to have been shifted to the right. This shift means the SIF range obtained by DIC is greater than expected following the analytical calculations. The difference in crack growth cannot explain this behaviour for series 4 and 5 because the starting SIF is expected to be of similar value in such a case. The results are, however, in line with the obtained structural stresses, as they were all higher than expected. In addition, Series 3 was closest to the expected value when looking at the structural stress. This alignment is also the case for the stress intensity factor data, as it is the only one aligning with the expected values.

Because of computational time, only a limited amount of points images were evaluated. However, when the amount of images is increased, the results do not change significantly, but an increase in resolution is achieved. In Fig. 12.34, it can be seen that a clear increase in detail is achieved, and the monotonic behaviour can be well observed. In Fig. 12.34, an overestimation of the SIF can be seen, but in this specific case for series three, it follows from the convergence study that this is due to the lower amount of Willliam's terms (n=8) taken into account.
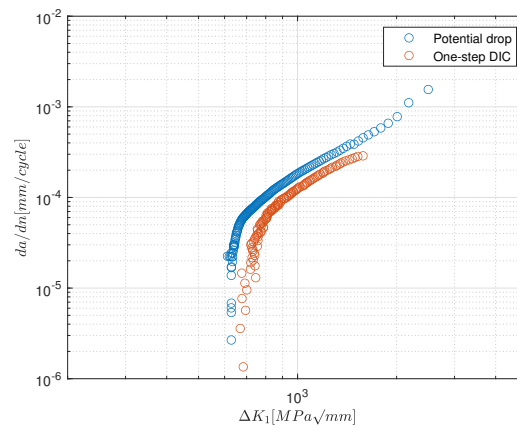
Figure 12.34: Comparison between the one-step DIC (n=8) and Potential drop obtained crack growth, Serie 3.

In an effort to explain the shift of the SIF obtained with the one-step DIC method, its results are compared to different methods. First of all, the one-step and two-step procedure can be compared. Furthermore, empirical formulations have been established for compact tension specimens following the ASTM standard (Eq. 12.11). However, the CT specimens in this research do not completely follow these specifications as they have a thickness of 8 mm instead of the 35 mm standard for the specimen's length. (Bower, 2009). Lastly, the SIF can also be determined following the Energy release rate method (Sec: 6.1.2; Eq. 6.2,6.3). Lastly, the calculation of the Stress Intensity Factor (SIF) is conducted employing the Energy Release Rate method (Section 6.1.2 and Eq. 6.2 and Eq. 6.3). The SIF is calculated based on the assessment of energy release rate, which is calculated as a contour integral. Notably, the contour integral may encompass any path encircling the crack tip; however,

following the crack interface is not required, and the crack widening should be excluded from the contour.
In the context of both the one-step and two-step Digital Image Correlation (DIC) methodologies, the displacement and stress fields are discretized grid-like. This discretization facilitates the reduction of the contour integral's complexity to a configuration of four linear segments aligned with the global coordinate system. This alignment significantly simplifies the mathematical expression through the contour normals. The strain energy density is obtained from the stress field in conjunction with the infinitesimal strain.

$$W = \frac{1}{2} \sum_i \sum_j \sigma_{ij} \epsilon_{ij} \tag{12.10}$$

In determining the loading on the specimen, these fields proved to be discontinuous, resulting in a proper structural stress definition. However, these discontinuities are smoothed out due to the contour integral, alleviating this problem.
The one-step DIC approach introduces a problem with respect to determining the SIF in this manner. The masking is in this approach applied from the start of the analysis. This masking means the contour integral does not reach the crack front. This problem does not exist when using the two-step approach, as the masking is applied between the two steps.

$$K_{1,ASTM} = (1 - r_{lr}) \cdot \frac{P}{B} \cdot \sqrt{\frac{\pi}{W}} \cdot (16.7 \cdot \frac{a}{W}^{\frac{1}{2}} - 104.7 \cdot \frac{a}{W}^{\frac{3}{2}} + 369.9 \cdot \frac{a}{W}^{\frac{5}{2}} - 537.8 \cdot \frac{a}{W}^{\frac{7}{2}} + 360.5 \cdot \frac{a}{W}^{\frac{9}{2}}) \tag{12.11}$$
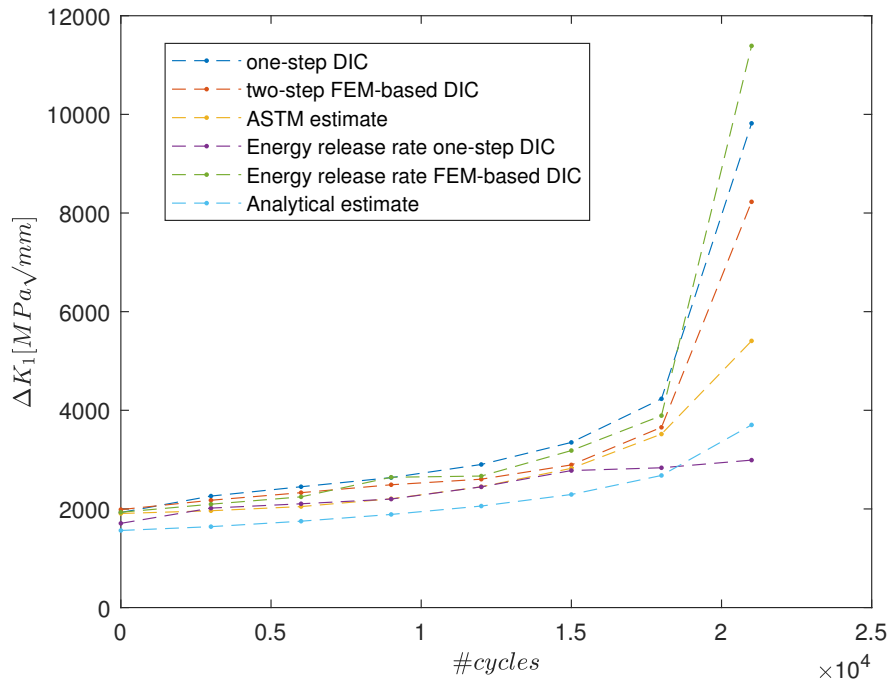
Figure 12.35: Comparison between the different methods to obtain the mode 1 SIF, for Serie 2.

The different SIF determination methods show that the analytical estimate provides the smallest mode 1 SIF values. Furthermore, it can be seen that the energy release rate provided by the two-step approach lies in between the values Williams-based values obtained by the one-step and two-step approach, providing confidence in the obtained results. The incomplete contour can explain the lower values obtained by the one-step DIC approach. In addition, the difference in the ASTM definition can be explained through empirical scatter and the difference in thickness of the specimen compared to the standard definition.

The SIF comparison can be extended to the crack growth relationship. In this relation, the crack sizes obtained by the one-step procedure are set out against the SIF obtained by the Williams terms in the one-step solution

and the SIF obtained by the energy-release rate from the two-step procedure. The SIF obtained from the two-step approach could also be set out against the crack size obtained by the two-step approach. However, due to the energy release rate formulation, the SIF obtained in this manner is not affected by the crack tip location. Additionally, it can be observed that the crack size difference between the two methods is minimal.
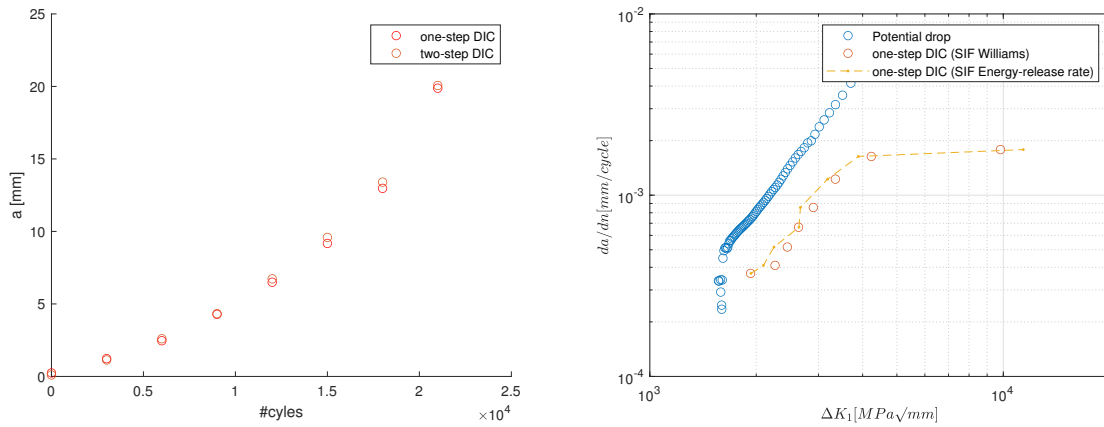
Figure 12.36: Crack size comparison one-step and two-step method (left). Comparison crack growth relation (right) Serie 2.

12.4.3. Error estimate
In order to evaluate the SIF estimate, its uncertainty can be investigated. Following the procedure described in section 8.2, the variance of the SIF range can be determined. The variance can be used to rule out an additional possible cause of the observed SIF discrepancy.
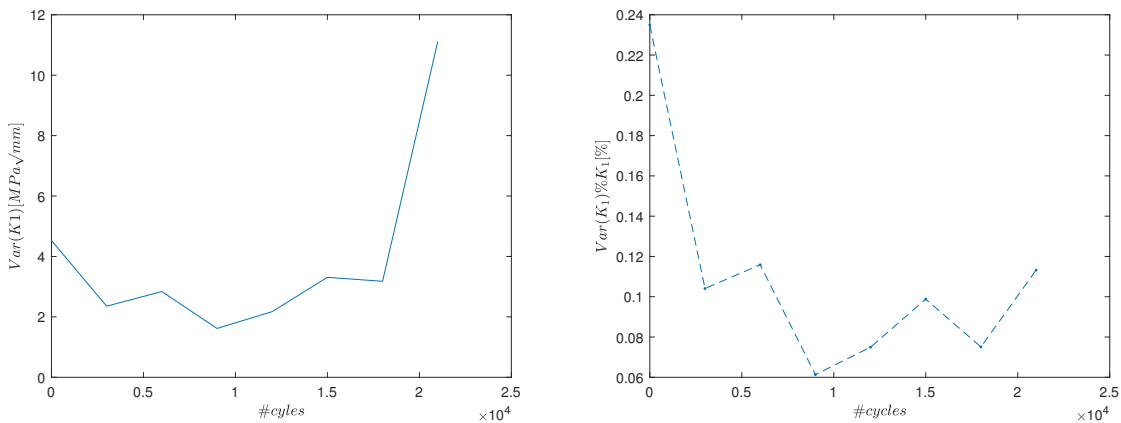
Figure 12.37: Variance of the mode 1 SIF (left) and the Variance expressed as a percentage of the SIF (right), for Serie 2.

The obtained variance of Series 2, which showed a significant difference in the SIF from the estimated value, is relatively small. This becomes especially apparent when expressing the variance as a percentage of the obtained SIF range. Indicating this uncertainty can not be used to explain the observed SIF discrepancy. Notably, the variance expressed as a percentage also shows that although the absolute value of the variance increases at a larger crack size, the relative value decreases due to the large increase of the SIF at larger crack sizes. The grey-level residual is an input of the variance determination, which can be evaluated as a more rudimentary error measure.
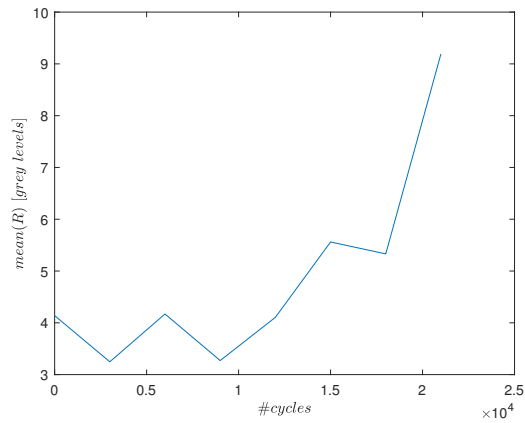
Figure 12.38: Mean grey level residual one-step approach of Series 2.

The average grey-level residual within Serie 2 demonstrates an upward trend in tandem with the expansion of the crack size. This phenomenon has been previously documented Vargas et al. 2016,Vargas et al. 2018). This pattern can also be expected, especially during crack widening, given that the asymptotic Williams solution assumes a closed crack configuration. Consequently, the mask is required to conceal the crack opening effectively. Notably, this behaviour increases as cracks increase in size, yielding a larger deviation from the Williams solution and, therefore, a larger residual value. Furthermore, in the last images, the crack tip approaches the mask's boundary, causing a part of the plasticity-affected region to extend beyond the masks. This could additionally increase the observed residual; however, adjusting the mask during the correlation procedure could minimise this.

Given the variance from the two-step approach (Fig.12.39, left), it becomes feasible to assess the enhanced accuracy of the one-step approach. It is important to note that a direct comparison between the grey-level residuals of both approaches is not possible, primarily due to the units of the displacement residual introduced in the two-step approach.

Compelling behaviour supporting the research hypothesis emerges when comparing the variances (Fig12.39, right), where a significant reduction in uncertainty is observed upon adopting the one-step approach.
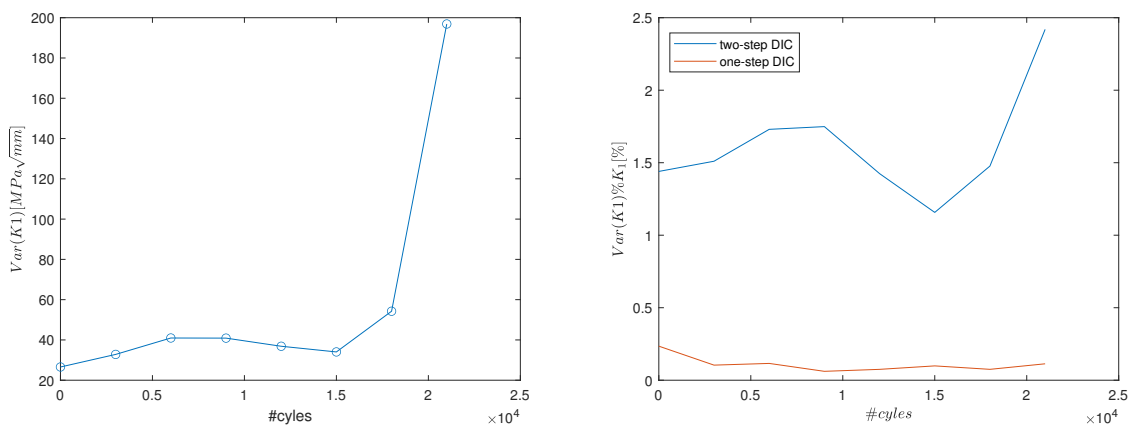
Figure 12.39: Variance of the mode 1 SIF two-step (left) and the Variance as a percentage of the SIF comparing two-step and one-step DIC (right), for Serie 2.

13. Total life parameter estimates

The material parameters must be determined to validate and apply the total life criterion. This chapter presents the parameters resulting from the maximum likelihood estimation and investigates which distribution best provides the best data fit. Additionally, the maximum likelihood estimators are presented to provide an uncertainty comparison.

The determination of the parameters for the total life concept has been performed in two distinct methods discussed in section 9.2. First, the parameters were established by leveraging failure data from welded specimens, while the second approach involved crack-growth data in non-welded specimens. The threshold stress was deliberately excluded in the parameter determination for the Welded dataset. This exclusion followed because the threshold stress is an additional random variable within the two-stage crack growth model, preventing straightforward integration into the lifetime model (Eq. 13.1-13.3). Alternatively, the single-slope Basquin model (Eq. 13.1) could be adapted into a dual-slope model to accommodate the threshold effect. However, incorporating this adjustment was deemed beyond the intended scope of this study. Additionally, it is noteworthy that the analysis is limited to mid-cycle fatigue data, meaning that the dual-slope behaviour should be limited.

$$\log(N) = \log(C^{-1}) - m \cdot \log(S_T) \tag{13.1}$$

$$S_T = \frac{\Delta\sigma_s}{(1 - r_{lr})^{1-\gamma} \cdot t_p^{\frac{2-m}{2m}} \cdot I_n^{\frac{1}{m}}} \tag{13.2}$$

$$I_n = \int_{a_f/t_p}^{a_i/t_p} \left(\frac{1}{(Y_n(\frac{a}{tp}) + n_1 \cdot Y_n(\frac{a}{tp})^{n_2 \cdot (1-r_{lr})^{n_3} \cdot (\frac{\sigma max}{\sigma_y})^{n_4}}) \cdot Y_f(\frac{a}{tp}) \cdot \sqrt{\pi\frac{a}{tp}}} \right)^m d(\frac{a}{t_p}) \tag{13.3}$$

The analyzed welded data originated from literature collected by Qin et al. 2021. The scope of the analysis was further limited to failures occurring at the weld toe, a choice supported by the application of the parameters in the context of the case study, which also revolves around weld toe failures.

The bounds of the parameters are important in the Maximum Likelihood Estimation (MLE), as outlined in Tab. 13.1. These bounds were generally defined within a relatively narrow interval and, where needed, expanded if a parameter approached a boundary. It is important to note that an exception was made for parameter γ, which is bounded to the range of 0 to 1 following the formulation of the total life model.

	lower bound	upper bound
$\ln(C)$	7	40
m	1	5
γ	0.01	1
σ	0.01	20
n_1	0.01	5
n_2	0.01	5
n_3	0.01	5
n_4	-1	5

Table 13.1: Welded Failure data MLE bounds

MLE	$\log_{10}(C)$	m	γ	σ	n_1	n_2	n_3	n_4	AIC
Normal	14.06	3.12	0.80	0.22	0.46	0.73	2.74	-0.08	2.874E+03
Weibull	14.20	3.21	0.83	0.29	1.35	2.42	-0.07	0.49	3.265E+03

Table 13.2: The MLE obtained by welded crackgrowth data.

The fatigue resistance curve can be determined by utilizing the Maximum Likelihood Estimation (MLE) parameters. In addition to the curve based on the maximum likelihood values, the 95 per cent confidence bound curves are presented. While the MLE values are important for estimating post-failure lifetime, adopting a more conservative approach when designing a structure is essential. Therefore, it is advisable to employ the lower bound for design considerations to prevent premature failure.

MLE's: $log_{10}(C) = 14.06$, $m = 3.12$, $n_1 = 0.46$, $\gamma = 0.80$, $\sigma = 0.22$, $n_2 = 0.73$, $n_3 = 2.74$, $n_4 = -0.08$; $T_S = 1{:}1.53$
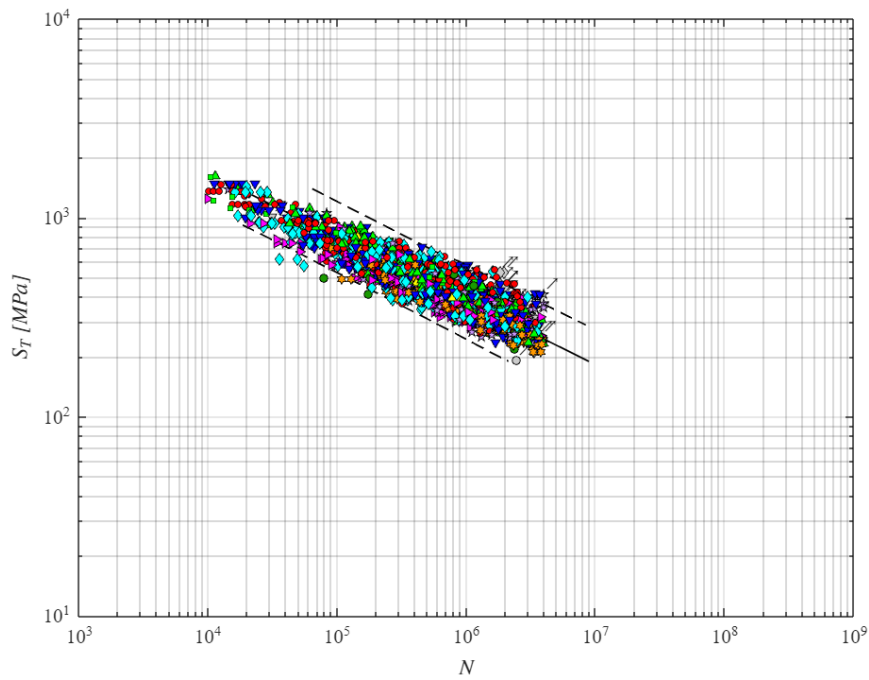
Figure 13.1: Total life parameter fitting welded data normal distribution

MLE's: $log_{10}(C) = 14.20$, $m = 3.21$, $n_1 = 0.26$, $\gamma = 0.83$, $\sigma = 0.29$, $n_2 = 1.35$, $n_3 = 2.42$, $n_4 = -0.07$; $T_S = 1:1.66$
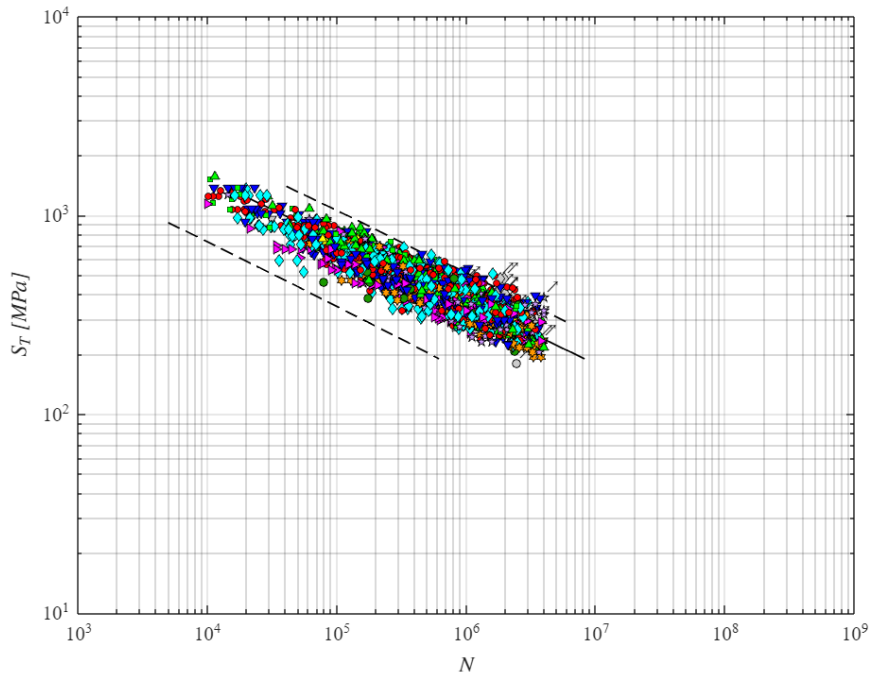
Figure 13.2: Total life parameter fitting welded data weibull distribution

The parameter determination shows that the uncertainty is significantly larger when assuming a Weibull distribution. This uncertainty could partially be explained by the fact that only mid-cycle fatigue data is analysed. Because when analysing high-cycle fatigue data, the threshold stresses are more likely to cause an extreme value distribution, which is not the case for mid-cycle fatigue.

The maximum likelihood estimate has been obtained using the MATLAB fmincon optimisation algorithm, a robust non-linear constrained multi-variable solver. There are multiple algorithms this function can employ. The active-set and the SQP (Sequential Quadratic Programming) could both be considered for the parameter determination of concern. Both methods generally operate the same way; however, the SQP algorithm has two advantages relative to the analysis of concern. Firstly, it entirely confines the parameters and the infinitesimal steps within the bounds, and secondly, it is able to recover from Infinite results. These properties help reach a solution even if the bounds are not perfectly defined. Especially in the total life model, with the addition of these four exponents, such problems could occur.

The parameter fitting can be performed based on the structural hotspot concept to determine the increase in accuracy obtained compared to more generally used assessment methods. In this concept, the fatigue resistance parameter is simply defined as the structural stress at the weld. Applying this concept significantly reduces the number of parameters to be determined.

MLE's: $\log10(C) = 10.75$, $m = 2.22$, $\sigma = 0.31$; $T_S = 1:2.27$
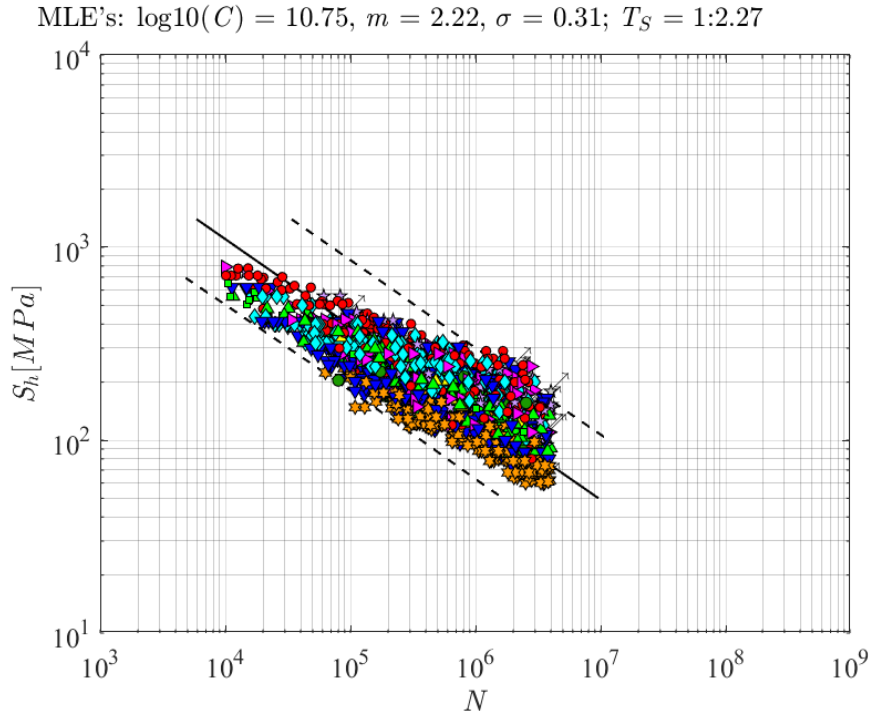
Figure 13.3: Hotspot structural stress parameter fitting welded data normal distribution

From the structural hot spot fitting, it is observed that the uncertainty, expressed in the standard deviation σ and scatter parameter T_S, is significantly larger compared to the Total life concept. These parameters indicate the benefit of the Total life concept compared to common engineering practice.

The maximum likelihood analysis has also been performed on the potential drop data obtained by Palkar (Palkar, not published). The main difference is that in this analysis, the dependent parameter is the crack growth value ($\frac{da}{dn}$) (Eq.13.4). Additionally, the threshold stress was included in this analysis; however, to limit the scope, it was only considered as an additional constant parameter instead of an additional randomly distributed parameter. But, similar to the welded data, the crack growth was analysed based on a normal and Weibull distribution. The Weibull distribution has also been corrected for bias (Eq. 9.13).

$$\log(\frac{da}{dn}) = \log(C) + m \cdot \log\left[\frac{(Y_n + n_1 \cdot Y_n^{n_2 \cdot (1 - r_{lr})^{n_3} \cdot (\frac{\sigma max}{\sigma_y})^{n_4}}) \cdot Y_f \cdot (\Delta\sigma_s\sqrt{\pi a} - \Delta K_{th})}{(1 - r_{lr})^{1-\gamma}}\right] \tag{13.4}$$

The potential drop experiments were conducted on sharp and blunt notch specimens. In the rest of this research, only five sharp-notch series were investigated with DIC. Because of the limited amount of series, the parameter determination was performed upon this larger data set. For the crack growth data analysis, the bounds (Tab. 13.3) proved more critical than in the case of the failure data set. Setting the upper bound of the elasticity parameters larger than three resulted in infinite values in the calculation. With this adjustment, the active-set algorithm can be used to obtain the maximum likelihood parameters.

	lower bound	upper bound
ln(C)	0	40
m	1	4
K_{th}	0.1	30
γ	0.01	1
σ	0.01	10
n_1	0.01	3
n_2	0.01	3
n_3	-1	3
n_4	-1	3

Table 13.3: Non-welded crack growth data MLE bounds

As can be seen in the bounds and in the MLE results, the base ten logarithmic value of the parameter C is similar to that obtained from the failure data. This similarity has been enforced by defining the logarithmic crack growth relation with the constant $\frac{1}{C}$ for parameter comparison.

MLE	$\log_{10}(C)$	m	K_{th}	γ	σ	n_1	n_2	n_3	n_4	AIC
Normal	12.2645	2.69	17.83	0.74	0.88	0.24	1.95	0.95	0.53	1.3425e+04
Weibull	12.5	2.75	16.86	0.86	0.48	0.23	2.86	0.76	0.49	4.98E+03

Table 13.4: The MLE obtained by non-welded crackgrowth data.

Contrary to the welded data, the Weibull distribution seems to provide a better fit according to the lower Akaike Information Criterion (AIC). This difference could be due to the fact that the crack growth is differently distributed than the failure data. Additionally, the inclusion of the threshold stress could cause the shift towards an extreme value distribution.

The crack growth curves derived from the parameters obtained through maximum likelihood fitting are presented with the potential drop data on which the fitting process was performed. While all series are utilized for parameter determination, a division into sharp and blunt notches is employed for visualization purposes.
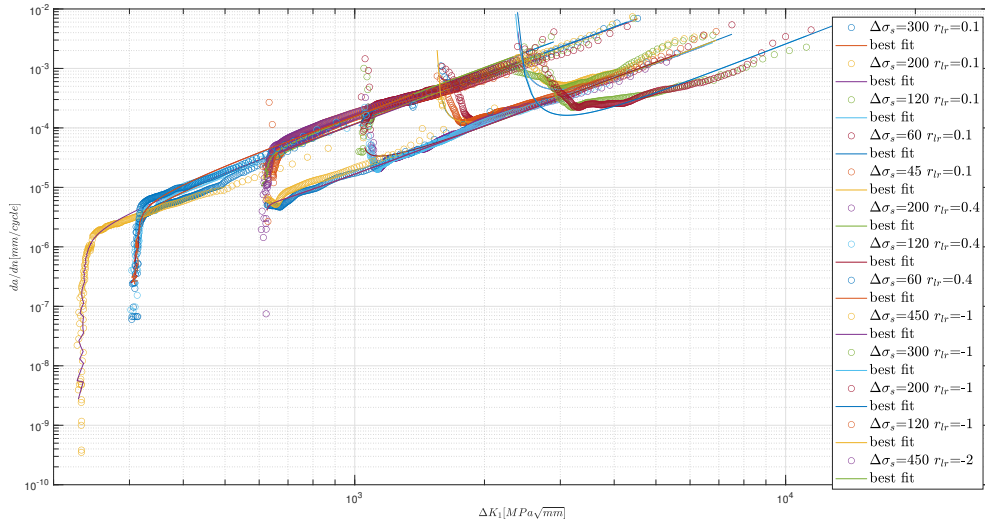
Figure 13.4: Normal distribution maximum likelihood fit crack growth data for sharp notch.
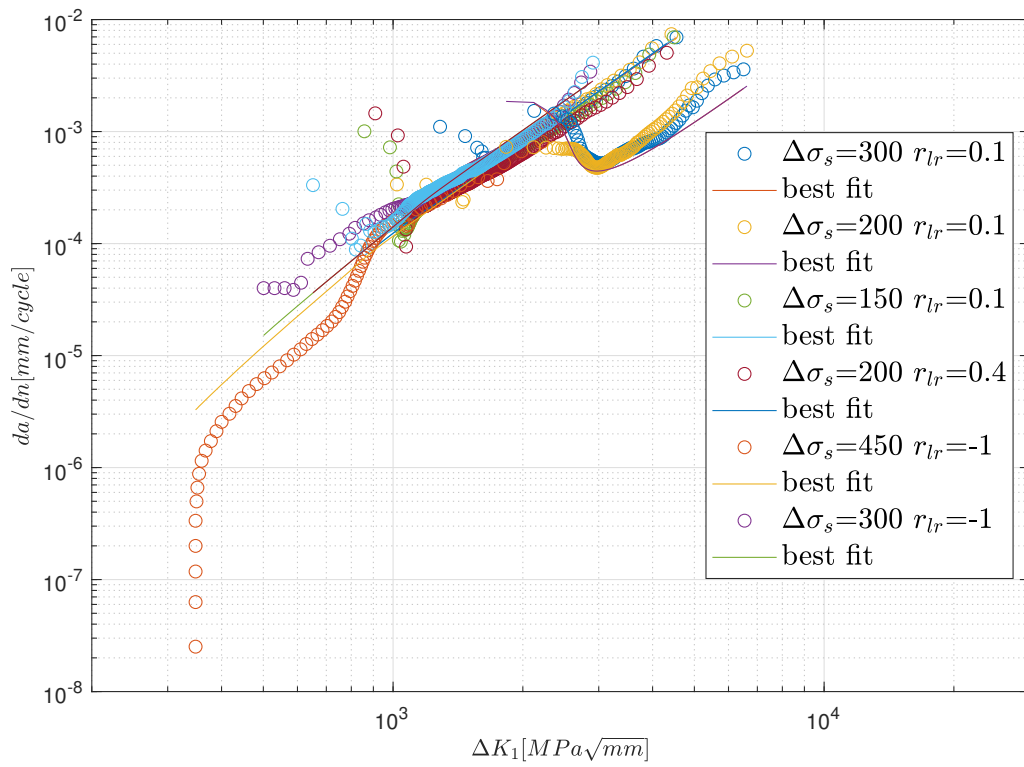
Figure 13.5: Normal distribution maximum likelihood fit crack growth data for blunt notch.
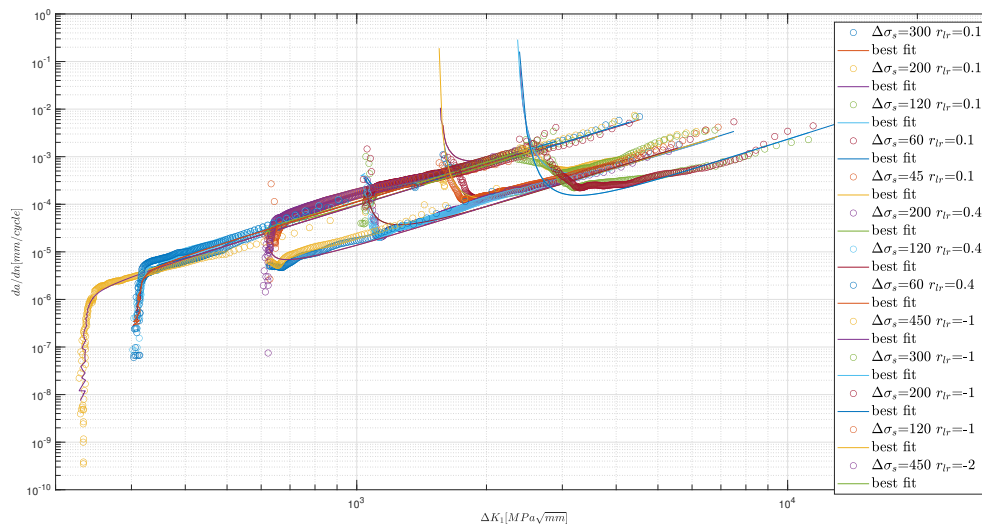
Figure 13.6: Weibull distribution maximum likelihood fit crack growth data for sharp notch.
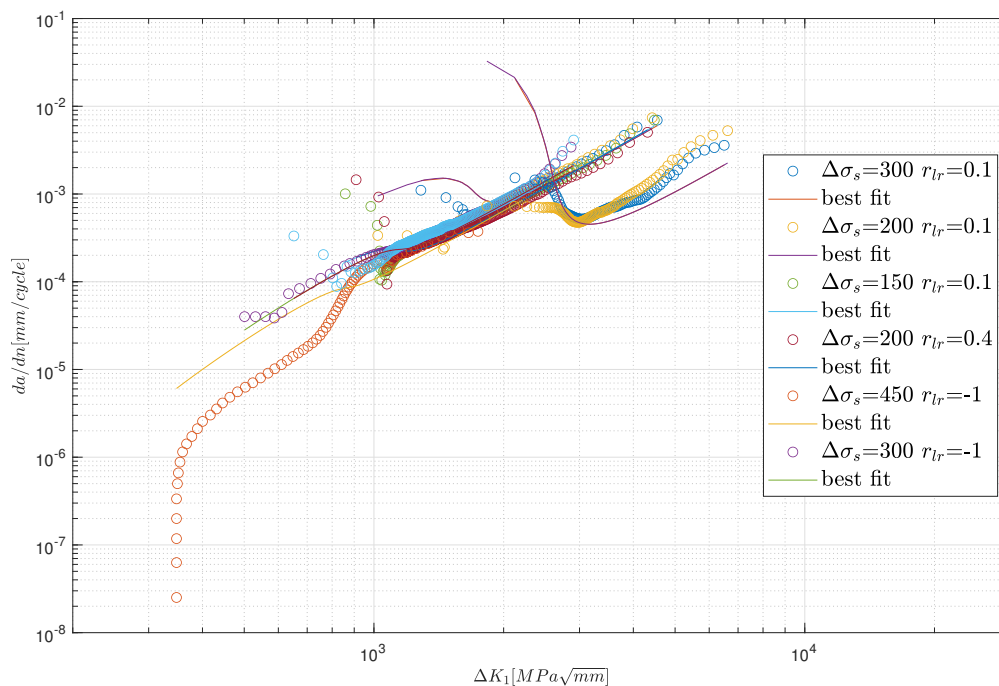
Figure 13.7: Weibull distribution maximum likelihood fit crack growth data for blunt notch.

The estimated crack growth curves can be compared to the Potential drop and one-step DIC data with the obtained total life parameters. The estimates based on welded data are not expected to align with the obtained data but provide insight into the effects of the welding on the estimated behaviour.
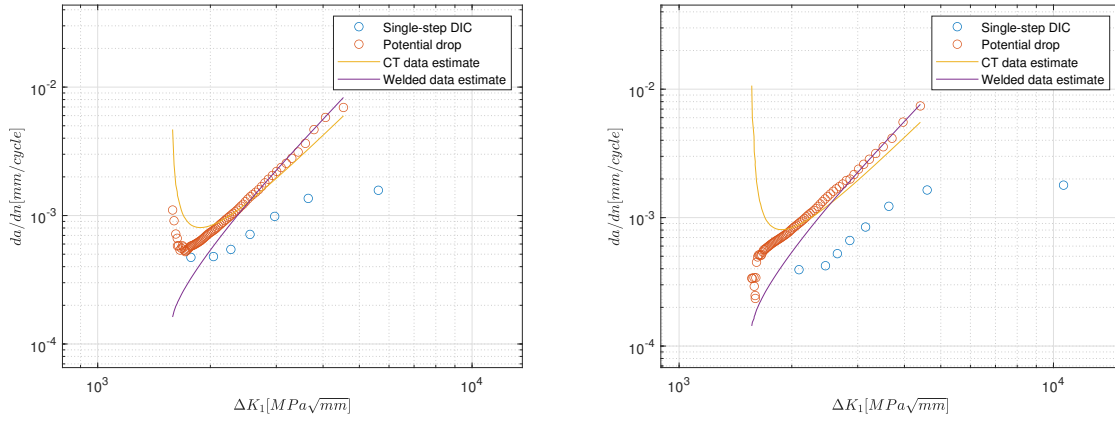
Figure 13.8: The obtained crack growth relations for serie 1(left) and serie 2 (right).
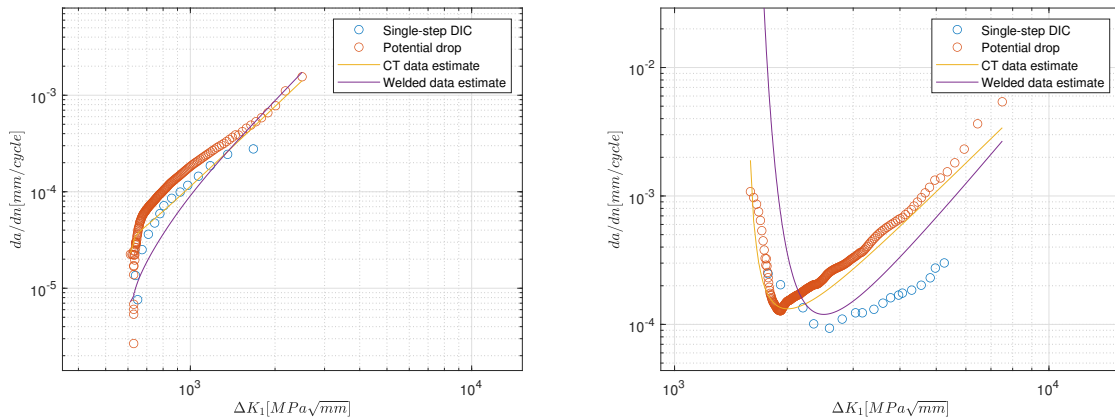
Figure 13.9: The obtained crack growth relations for serie 3(left) and serie 4(right).
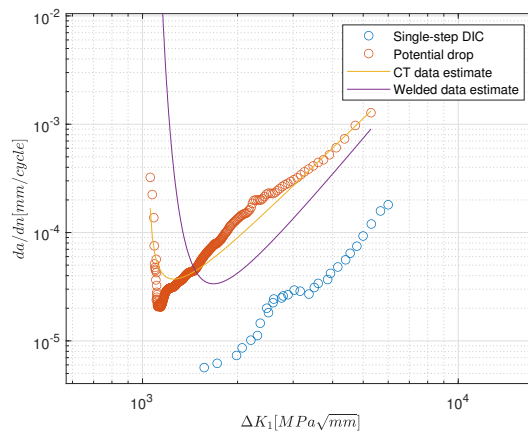
Figure 13.10: The obtained crack growth relations for serie 5.

An interesting observation arises when observing series 3 and 4, wherein the welded estimate exhibits a rightward shift from the point at which the crack growth transitions into a stabilized Paris relation. This phenomenon could be attributed to an increase in initial effect size, which can accelerate the initial crack growth.

Moreover, an interesting difference appears between the two estimates for the first two series. The welded estimate demonstrates a consistent monotonic trend, whereas the non-welded estimate displays non-monotonic behaviour. A corresponding pattern would be anticipated since series 1 and 2 share identical loading conditions. However, the difference between the potential drop results for both series might indicate that this loading condition is between these two behaviours, which is supported by the subtle effect. The estimate could be influenced by the more common behaviour of the data, with the welded data including more monotonic behaviour.

Finally, it is noteworthy that despite the welded estimate being derived from failure data, it still manages to predict monotonic behaviour. This observation is important as these data points were less explicitly incorporated than in the crack growth dataset.

14. Case study

This chapter presents the outcomes of the case study provided by Bureau Veritas, which is an integral part of the final aim of this thesis, applying the total life model to a genuine engineering scenario and comparing the approach to a common engineering approach. This case study's assessment requires examining two essential components: fatigue loading and resistance.

The fatigue resistance can be derived from the total life model, requiring the total life parameters. The evaluation specifically concerns the identification of a cracked location within a welded joint. Consequently, the parameters employed in this model are the parameters obtained from the welded failure data presented in Chapter 13. The wave loading has been determined following a representative load case scenario and a spectral approach to determine the expected wave loading for the case study. In combination with the cargo loading, this provides the complete load condition of the ship.

Both methods of obtaining the loading result in several loading scenarios from which the loading can be applied to a detailed hotspot FEM model with solid elements. These solid elements obtain the through-thickness stress distribution and structural stress. The structural stress in all methods is obtained following the nodal force method (Eq. 2.4-2.5). This method was chosen because the resulting analytical trough thickness stress distributions provided a better fit to the FEM values than a stress value-based determination.

14.1. Rule-based wave loading

The Bureau Veritas rules provide maximum and minimum conditions for each of the four load cases (Sec. 10.1.1). The application of these conditions upon the cargo hold model results in 8 different stress states at the hotspot location. The forces and displacements are taken from the cargo model and prescribed on the boundary of the detailed FEM model, in which the weld was modelled with solid elements. It is assumed that the combination of the maximum and minimum of each load case represents the stress range of a representative cycle.

	$\sigma_{s,max}$	$\sigma_{s,min}$	r_s	C_{bw}
Load case A	265.7	-76.9	0.45	0.1
Load case B	92.6	92.6	0.42	0.1
Load case C	328.0	-147	0.43	0.2
Load case D	273	-75.5	0.50	0.2

Table 14.1: Stress distributions parameters from the BV load cases.

With the obtained structural stress, the analytical stress distribution is determined. This distribution can be compared to the stresses obtained from the FEM analysis. In Fig. 14.1, the comparison can be seen for the maximum stress state of load case A, with C_{bw} assumed to be 0.1, as this value for the weld load-carrying coefficient provided the best fit regarding this distribution.
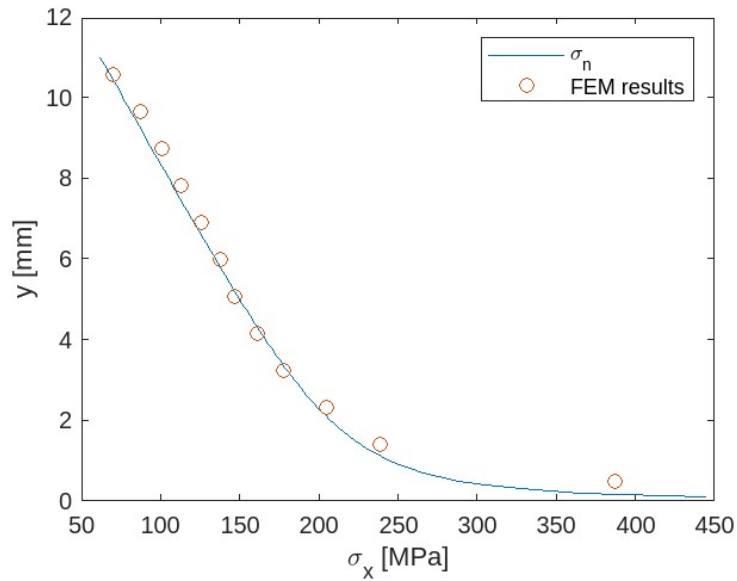
Figure 14.1: Through-thickness stress distribution loading condition A max, $C_{bw} = 0.1$

With the analytical stress distribution, the notch factor can be obtained (Fig. 14.2). Although the thickness is 11 mm, only the interval from 0.01 to 8 mm is shown. This interval was chosen because of singular behaviour at the notch and full thickness. This behaviour at the notch is caused by the singular stress caused by the infinitely sharp notch. The singularity at full thickness is due to the fact that when the crack is the entire thickness, there is no material left, resulting in infinite stress.
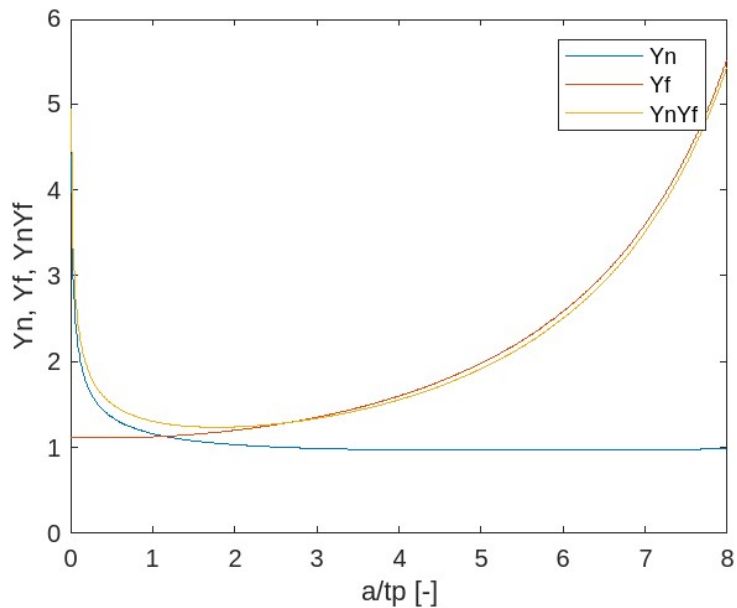
Figure 14.2: notch and far-field factor plot

The last unknown parameter is the far field factor. In general it is assumed that the handbook solutions for an edge crack provide the best fit for the case. However, for comparative reasons the damage has been calculated for an eliptical crack solution as well. lastly the non-welded parameters obtained from the CT specimen have been taken into account. This could represent a case were the party was made out of a solid part of steel and is as well just incorperated out of comparative reasons. The damage of each load case can be determined according to the procedure described in chapter 10. Following the Bureau Veritas rules each load case has an associated weight factor to add them up into a total damage value. Lastly, following from the rules this sum has been multiplied with a sailing factor of 0.8.

	Load case A	Load case B	Load case C	Load case D	Total	Life [years]
Damage welded $Y_{f,eliptical}$	0.0355	0	0.1022	0.0453	0.0441	22.69
Damage welded $Y_{f,SEC}$	0.0580	0	0.1826	0.0778	0.0772	12.95
Damage non-welded $Y_{f,eliptical}$	0.0077	0	0.0180	0.0094	0.0059	168
Damage non-welded $Y_{f,SEC}$	0.0132	0	0.0333	0.0172	0.0133	75.2
Weight factor	1/6	1/6	1/3	1/3	1	-

Table 14.2: The damages due induced by the load cases based on different Far field and parameter assumptions.

It can be observed that the variations in the assumed parameters and far field distribution result in a drastically different expected lifetime. Utilizing parameters from non-welded conditions leads to an almost infinite lifespan projection for the weld. However, the expected lifetime is calculated to be 12.95 years upon employing the most representative parameters. This lifetime aligns with the observation of a 40 cm through-thickness crack after roughly ten years, suggesting that the crack could have been entirely through-thickness before this point.

Notably, the current calculation method is based on small-scale specimens, thus neglecting large-scale effects in the presented lifespan estimation. Among these factors, hierarchy and attracted load path could alter the main load path and reduce the load upon the hot spot. This effect could decelerate the crack growth rate following the initial formation of a small crack.

The results can be compared to the results following from the standard Bureau Veritas rules evaluation. in which the structural hot spot concept is used for the determination.

	Load case A	Load case B	Load case C	Load case D	Total	Life [years]
Damage	0.1075	0	0.2655	0.1295	0.149	6.71
Weight factor	1/6	1/6	1/3	1/3	1	-

Table 14.3: Bureau Veritas rule based hotspot structural stres result

From the structural hotspot-based approach, it can be observed that the expected lifetime is significantly shorter than the total life obtained results. This difference could be explained by the fact that the rule-based method makes use of design curves instead of maximum likelihood values. Additionally, due to the increased uncertainty of the structural hot spot concept compared to the total life concept, it requires more conservatism in order to obtain the same confidence bound.

Furthermore, it is observed that in both methodologies, when subjected to load case B, the incurred damage becomes zero. This result stems from the interaction of the applied forces, resulting in the maximum and minimum loads becoming equal for this specific load case. These equal loads result in the structural stress range induced by this specific load case diminishing to zero.

14.2. Wave Spectrum loading

In an effort to reduce the uncertainty on the loading side of the fatigue lifetime determination in the case study, a spectral analysis was performed (Sec. 10.1.2). A full free-floating ship model is used in a hydro-structural solver to obtain the structural response of the ship in the different sea states.

Each sea state is represented by a single regular wave corresponding to the spectrum's wave period and significant wave height. To limit the research scope, two representative wave directions are chosen (front quartering waves 135 and 225 degrees) instead of a full 365-degree wave field.

The analysis is performed according to a time series in which waves come in contact with the ship. The initial stages should be ignored in further analysis, as a start-up phase is present in which the loading builds up. Afterwards, the loading and response stabilize in a sinusoidal pattern. However, due to phase shifts of the response compared to the wave loading, it is difficult to determine the exact moment at which the structural stress is maximum and minimum in the hot spot. Therefore, three semi-random times have been chosen to

extract the forces and displacements upon the detail. Due to the regular wave applied, it can be assumed that the structural response will show perfect sinusoidal behaviour. Additionally, the hydro-structural model provides the response frequency.

After determining the structural stress at each of the three semi-random moments, a sinusoidal function can be fitted through the three data points in order to obtain the structural stress amplitude, phase shift and mean shift.
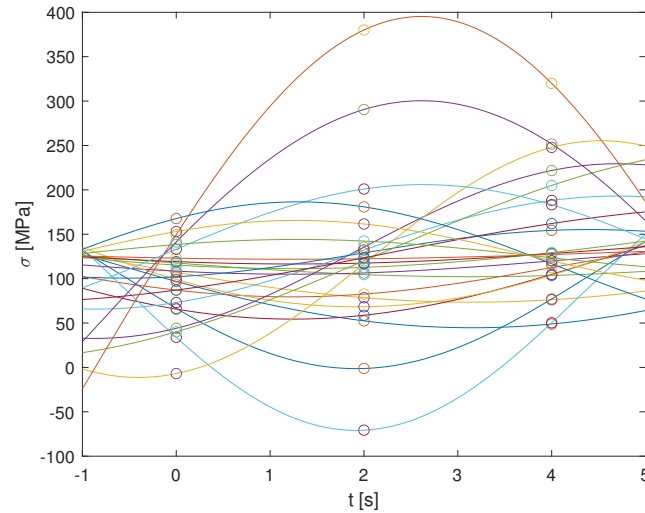
Figure 14.3: Obtained structural stress time series.

The structural stress range and the mechanical loading ratio can be determined from the amplitude and the mean shift. The same procedure is used to determine the analytical through-thickness stress formulation as in the Bureau Veritas load case procedure, with the remaining undetermined parameter being the structural stress bending ratio. This value was fairly constant at the three evaluated points and over each sea state, around 0.38, except for a few points. These deviations occur when the structural stress is nearly zero, which can skew this ratio. This is not likely to occur at the response peak; therefore, the loading ratio of 0.38 is assumed at the maximum and minimum stress.

Hs [m]/Tz [s]	4.5	7.5	10.5	13.5
3.5	15	239	30	35
5.5	34	206	66	105
8.5	72	319	143	163

Hs [m]/Tz [s]	4.5	7.5	10.5	13.5
3.5	35	159	109	55
5.5	79	498	239	127
8.5	146	771	266	196

Table 14.4: Structural stress ($\Delta\sigma_s[MPa]$) for a 135 degree (left) and a 225 degrees (right) wave.

Hs [m]/Tz [s]	4.5	7.5	10.5	13.5
3.5	0.88	0.22	0.78	0.74
5.5	0.78	-0.01	0.54	0.41
8.5	0.61	-0.29	0.27	0.22

Hs [m]/Tz [s]	4.5	7.5	10.5	13.5
3.5	0.75	0.22	0.40	0.65
5.5	0.52	-0.66	0.04	0.34
8.5	0.21	-0.95	-0.04	0.14

Table 14.5: Mechanical loading ratio (r_{lr}) for a 135 degree (left) and a 225 degree (right) wave.

The notch factor is obtained with the obtained loading parameters and the following analytical through-thickness stress distributions, and a single-edge crack formulation is used to obtain the far-field stress distribution. Following, the total life fatigue resistance parameter is established for each sea state, which

allows the Basquin relation to be used to determine the lifetime in cycles corresponding to each sea state. A yearly damage value is obtained by dividing the total yearly expected number of waves by the calculated resistance.

Hs [m]/Tz [s]	4.5	7.5	10.5	13.5	Hs [m]/Tz [s]	4.5	7.5	10.5	13.5
3.5	0.000	0.246	0.000	0.001	3.5	0.001	0.069	0.023	0.004
5.5	0.001	0.151	0.006	0.021	5.5	0.009	1.202	0.241	0.036
8.5	0.008	0.382	0.051	0.074	8.5	0.052	3.940	0.308	0.131

Table 14.6: Yearly damage induced by a 135 degree (left) and a 225 degrees (right) wave.

Assuming the likelihood of the 135 and 225-degree waves is equal, the total yearly damage can be calculated by averaging the damage in both directions.

Hs [m]/Tz [s]	4.5	7.5	10.5	13.5
3.5	0.001	0.126	0.010	0.002
5.5	0.004	0.541	0.099	0.023
8.5	0.024	1.729	0.144	0.082

Table 14.7: Total yearly damage for each sea-state.

The expected pattern of higher waves resulting in increased damage can be observed from the damage per sea state. Interstingly, a peak can be observed in which the waves with a period of 7.5 seconds induce the largest unweighted damage. A comparison with the waves with a period of 4.5 seconds shows a significant decrease in damage, although the yearly amount of waves is equal for each sea state. This shows the dominating effect of the stress range. When comparing loading ratios, the mean stress level can be concluded to be significantly lower for the waves with a period of 7.5 seconds. However, the limited effect of the higher mean stress is expected as it does not result in a higher maximum stress due to the smaller stress range.

Following the yearly damage for each sea state, the directions are averaged, and the sea spectrum (Tab. 10.1) is used to determine the weighted average of the yearly damage from each sea state. Similar to the load case-based approach, a sailing factor of 0.8 is applied. Allowing for the determination of the expected lifetime.

Yearly Damage	0.1036 [-]
Expected life time	9.65 [years]

Table 14.8: Total life time, Homer based results.

According to this method, the expected lifetime provides a shorter lifetime than the total life concept with the Bureau Veritas loading conditions. However, this method resulted in a longer lifetime than the structural hotspot concept with the load case approach. Indicating that the increase in conservatism results in a larger difference than the difference in loading.

IV

Judgement and future work

15. Conclusion

The results of the research undertaken in this study allow for several conclusions to be drawn. These conclusions can be structured in the format of the answers to the relevant research questions. The overarching research question is answered by answering each of these research questions and combining their outcomes; additionally, the research hypothesis is evaluated.

Can Airy stress functions be used in a one-step DIC approach to effectively capture the far field stress distribution?

This study successfully formulated and implemented a global one-step Digital Image Correlation (DIC) methodology. This one-step approach was applied in conjunction with a diverse set of basis functions corresponding to the specific kinematics of the region of interest under investigation. Notably, the incorporation of linear Airy stress functions into the one-step DIC allowed its utilization in the analysis of the far-field stress distribution. Subsequently, the developed methodology was employed to determine the far-field stress distribution within a T-joint specimen. The outcomes obtained through the global one-step DIC approach were in agreement with those derived from the two-step Finite Element Method (FEM)-based approach and a localized two-step subset-based approach.

In the context of a Compact Tension (CT) specimen, determining the far-field stress distribution presented a challenge, primarily following from its geometry. In this instance, the far-field stress distribution cannot be independently observed but follows as a result of superimposing the through-thickness stress distribution within the notch region. Notably, the application of the developed methodology employing linear stress functions in the notch region yielded unsatisfactory results in achieving the far-field stress distribution. It is important to emphasize that this limitation in obtaining the far-field distribution is attributed not to any inherent flaw in the implementation of the one-step DIC approach but rather to the constraints- the underlying field assumption imposes on the correlation procedure. This conclusion is supported by the observation that the two-step FEM-based approach exhibited the same behaviour in this context.

Can the Williams displacement field solution be used in a one-step DIC procedure as a reduced kinematic basis for the notch region?

This research effectively integrated the Williams series solution into the established global one-step Digital Image Correlation (DIC) procedure, aiming to analyse the displacement field around a cracked geometry. Initially, the methodology was deployed to analyse a long crack under straightforward far-field stress conditions. The results showed that a limited number of Williams terms were sufficient to accurately describe the displacement field around the crack. Furthermore, a comparative analysis of the results obtained through this method against those from a two-step FEM-based DIC approach revealed significant similarity. Importantly, this approach removed the necessity of intermediate kinematic assumptions, enhancing the accuracy of the global field determination. Subsequently, the one-step DIC approach was applied to the Compact Tension (CT) specimens that were the primary focus of this research. A convergence study showed the need for an increased number of Williams terms to analyse these specimens effectively.

Moreover, it was observed that despite the inherent capacity of the Williams series solution to account for discontinuities within the displacement field, a masking procedure needed to be implemented around the crack for two reasons. Firstly, the employed asymptotic Williams solution describes a crack with minimal widening. This property is invalidated in cases involving substantial crack widening, thereby invalidating the assumed continuities around the crack. Secondly, when the crack tip location precisely coincides with an evaluated pixel, the singular term in the crack tip determination algorithm results in an infinite value at that specific location, consequently causing the correlation algorithm to malfunction.

Does one-step DIC improve the crack tip estimate with respect to a two-step approach?

This research has presented four procedures to obtain the crack size estimate: the residual method in a two-step approach, the singular term method in a two-step approach, the singular term method in a one-step approach and the potential drop method.

Due to the variance definition, the crack-tip uncertainty can not be determined explicitly. However, considering the reduced uncertainty of the displacement field amplitudes, it can be assumed that the crack-tip location assumption is more accurate following the one-step approach than the two-step approach employing the singular term method. However, due to the difference in procedure, an increased accuracy compared to the residual error method can not necessarily be drawn from the residual approach.

Furthermore, it can not be undoubtedly argued that the developed one-step approach improves crack-tip determination compared to potential drop measurements, as no specific error measure is known. Additionally, a significant difference between the methods has been observed for the analyzed experiments with a mechanical loading ratio of -1. However, the DIC method allows the decoupling of the analysis from the potential drop calibration curves, which can limit accuracy when deviant geometries are investigated.

Additionally, one of the main constraints of the singular term methodology employed in the one-step approach is its inherent limitation in estimating the location of the crack tip relative to the crack propagation direction. This constraint requires prior knowledge of the crack tip location in the direction perpendicular to the crack propagation vector. Notably, this constraint is also applicable to the two-step FEM-based approach when employing the same crack-tip estimation technique. However, the two-step nature of the procedure allows for more freedom in the choice of the used crack-tip estimation algorithm. Specifically, the residual error method allows for a higher degree of freedom in order to determine the crack-tip location.

For these reasons, it can not be concluded that the one-step approach is to be preferred over the two-step approach.

Can one-step DIC be effectively used to Validate a crack growth model?

It cannot be definitively concluded that the one-step DIC approach effectively serves as a validation tool for the total-life crack growth model. This uncertainty follows from the substantial difference between the SIF ranges obtained through the DIC approach and those derived from analytical calculations. Consequently, the parameters in the total-life model are not validated. Nonetheless, it is worth noting that the model can capture both monotonic and non-monotonic behaviours in the short crack growth region. This observation supports the model's underlying assumptions about the elastoplastic behaviour around the notch determining the short crack growth. Moreover, these behaviours are effectively incorporated through the threshold stress and notch plasticity factors.

Can the two stage crack growth model predict the life time behaviour of a hot spot in an actual vessel?

In the presented case study, the expected lifetime of a critical hot spot within a general cargo vessel has been determined following the fatigue resistance and loading characterisation. The fatigue resistance was determined through parameter fitting employing maximum likelihood estimation. The data representing as-welded conditions showed conformity to the normal distribution, rendering it the most suitable. The load determination was performed through two distinct methods. Initially, four representative load cases from the Bureau Veritas rules were employed and subsequently extrapolated to encapsulate the entire loading spectrum. Secondly, a wave spectrum approach was used to minimise loading-related uncertainties. The loading data generated by both methodologies were subsequently applied to a solid element FEM model of the critical weld allowing for the determination of the structural stresses and through-thickness stress distribution. When inserted in the total life formulation, these result in the total stress load parameter. Collectively, this approach provided realistic estimations of the damage and fatigue lifetime of the detail.

Can the two stage crack growth model improve the prediction of the life time behaviour with respect to a classification rule based assessment?

Implementing the total-life model has shown a reduction in the uncertainty associated with the fatigue resistance relationship compared to the structural hot-spot concept, which is commonly employed in rule-based approaches. This uncertainty reduction indicates an increase in the accuracy of the fatigue resistance. In the presented case study, this reduction in uncertainty translated into the prediction of a longer lifetime due to the decreased level of required conservatism.

However, it is essential to realise the current limitations of the total-life model. Currently, the model should only be applied if the stress intensity range is being determined using the same procedures employed in the parameter fitting process, primarily due to the uncertainty in the fitting parameters stemming from the

discrepancies in the SIF estimates. Moreover, it should be noted that the improvement of the lifetime estimate depends on the loading data's accuracy. Therefore, the model excels in laboratory conditions where loading is precisely known. However, in ship design, where loading is characterised by high stochasticity, the total life model's accuracy increase is diminished. Consequently, in the design phase, the total-life model may not improve accuracy compared with conventional rule-based approaches.

Concluding from the answers to the research questions presented above, the main research question can be answered:

Can a two-stage crack growth model be used to improve the fatigue life time estimate of arc-welded joints in marine structures?

It can be concluded to be, that although the model can be used in order to predict the lifetime of arc-welded maritime structures, in the current stage of the total life model, combined with the inherent uncertainties in the loading of maritime structures, the total life model does not provide a significant improvement in the lifetime estimate.

Furthermore evaluating the research hypothesis:

In order to improve the fatigue total life time estimate of arc-welded joints in steel marine structures, validation of the involved two-stage crack growth model requires a one-step DIC approach.

The one-step DIC approach could be used for validating the total-life model as it demonstrates increased accuracy compared to the two-step DIC approach. Nevertheless, given the substantial similarity with the results obtained from the two-step approach, adopting the one-step approach may not be necessary, especially considering the additional flexibility in SIF and crack-tip estimation procedures. Additionally, explaining the SIF discrepancy is required before employing any DIC approaches for validation.

16. Discussion

From this research, several avenues of investigation remain. This chapter will discuss which improvements can be made in future work, as well as several questions following the conclusions of this research. First, the discussion points resulting from SIF estimates obtained through DIC will be discussed, followed by the obtained crack sizes. Lastly, possible further improvements concerning the case study will be discussed.

16.1. Stress intensity factor

Considering the discrepancies between the expected loading of the specimens and the obtained loading parameters through DIC is a primary concern. Further investigation must be performed to investigate if the forces reported by the exciters during the experiments translate to the structural stresses expected to be caused by such a method.

The first proposed avenue of further investigation follows from the structural stress calculations. The calculations performed in this research showed that the first-order FEM-based approach resulted in a discontinuous stress field from which the structural stress could not be adequately determined. Therefore, the continuous stress field obtained from the one-step approach was used. In finite element calculation, the calculation of the structural stress based on nodal forces increased accuracy. Additionally, although the initial investigation did not show the Williams solution resulting in any accuracy loss, confirming the loading independent of the Williams formulation could be beneficial. Therefore, it is proposed to introduce a second-order FEM-based approach in future work, which introduces second-order continuity, resulting in a continuous stress field description. This increase in continuity decreases the fluctuations observed in the trough-thickness stress distribution obtained with a linear shape function FEM-based DIC approach, allowing for an adequate determination of the structural stress with this approach.

Besides obtaining the structural stress with a higher order FEM-based DIC approach, it could also be used to directly determine the Stress intensity factor (Sec: 6.1.2). However, it should be noted that in such an approach, the elements must be orientated around the crack tip, and the nodes must be allowed to coincide. These requirements around the crack tip would result in a significantly more complex element description than the square grid-based approach employed in the FEM-based DIC approach in this research. A distinct advantage of such a method could be a further decrease in the made errors because it was observed that the increase in error of the two-step approach originates from the post-processing step. Compared to the first step of the two-step approach, the residual grey-level error is increased due to the increased enforced constraint in the displacement field. Therefore, a higher confidence value could be obtained assuming the Stress intensity factor determination method does not introduce errors in its own right. However, the calculated variance for the SIF from the one-step approach was already relatively small, making this increase in confidence not a specific goal in its own right.

In the data series evaluated in this research, all the images were captured at the maximum loading condition, and the stress range was obtained as a linear scaler from the known loading ratio. The obtained stress range could be validated by including minimum load images in the series. Besides the stress intensity range, this also allows for a complete investigation of the loading application.

In case additional experiments are conducted for further investigative purposes, collecting images from both sides of the cracked specimen could provide additional insights. A comparison of front-face and back-face data could rule out three-dimensional effects.

16.2. Crack size

The difference in crack size estimates between the potential drop results and those obtained from the one-step DIC approach, specifically within the series with a load ratio of -1, represented another unanticipated outcome of this research. In order to determine if the loading ratio is the origin of this issue, additional series should be investigated. If the discrepancy proves to be constrained to the two evaluated series, it can be hypothesised that an electrical leak was present at these series, disrupting the Potential drop results.

Alternatively, if more series are affected, a possible explanation could be found in the fact that these experiments have the lowest load level. This lower load level could result in the displacement field being less pronounced, which could result in more ambiguity in the fitting process of the Williams solution onto the displacement field.

Additionally, this lower loading results in the plasticity-affected area decreasing. It could be further investigated if smaller masking of the crack tip would result in a better estimate of the crack tip in these lower load cases.

Furthermore, lower stress series with positive loading ratios should be analysed to confirm whether the problem would be caused due to the lower load level. However, it should be noted that the difference between the maximum load of Serie 3 and Serie 4 was already only 50 MPa, and Serie 3 showed good alignment with the potential drop results.

Another possible reason that could explain the difference in the results of load ratio -1 is the paint. Because the speckle pattern was applied with a paint that proved to be significantly more elastic, as it can be seen spanning the crack opening in some of the larger images, it could possibly be restored to its original state by closing the cracked specimen at negative loading ratios. Alternatively, it could be that the paint has remained intact whilst a crack has formed underneath, resulting in a crack size underestimation. However, this is deemed very unlikely. Because this would only affect the direct crack region, whilst this crack region is masked out completely, the DIC procedure would not consider such an effect.

Figure 16.1: Intact paint layer over large crack.

16.3. Case study

For the application of the total-life model on actual marine structures, some points of concern remain as well. Firstly, the welded parameter determination should, in future work, be elaborated to a two-slope model. The two-slope behaviour can be used to capture the random variable behaviour of the threshold stress, which was excluded in this research due to the integration procedure not being straightforward with the inclusion of this randomly distributed parameter.

Furthermore, the far-field factor at hot spot type A should be further investigated. The obtained damage based on an elliptical or edge crack formulation varied significantly. The main difficulty in the elliptical crack formulation comes from the unknown elliptical ratio. Future work could include the incorporation of an elliptical ratio estimator. Alternatively, the error made through the edge crack assumption could be investigated.

Lastly, it is inherent to fatigue analysis that the uncertainty in fatigue predictions follows from both the resistance and loading side. Therefore, the effort to decrease the uncertainty in fatigue lifetime predictions should follow from both of these perspectives. Therefore, full advantage of the total life model can only be taken when the uncertainty in the loading is decreased, which is practically impossible to achieve in the design stage. However, in the case study in this research, the crack growth is evaluated retrospectively. An effort to accurately reconstruct the loading has been made in the form of determining the approximate sailing

routes to determine a super-positioned sea spectrum for this ship. Although this reconstruction can be performed in greater detail, there exists a limit to the possibilities. In an ideal scenario, monitoring and atomisation of the data collection would be employed to obtain the loading over the structure's lifetime.

References

ASTM. (2016). Standard test method for measurement of fatigue crack growth rates. ASTM.

Baker, S., & Matthews, I. (2004). Lucas-kanade 20 years on: A unifying framework. International Journal of Computer Vision - IJCV.

Barber, J., & Klarbring, A. (2003). Solid mechanics and its applications.

Barhli, S., Mostafavi, M., Cinar, A., Hollis, D., & Marrow, T. (2017). J-integral calculation by finite element processing of measured full-field surface displacements. Experimental Mechanics, 57, 997–1009. https://doi.org/10.1007/s11340-017-0275-1

Bergonnier, S., Hild, F., & Roux, S. (2007). Local anisotropy analysis for non-smooth images. Pattern Recognition, 40(2), 544–556. https://doi.org/https://doi.org/10.1016/j.patcog.2005.09.013

Besnard, G., Hild, F., & Roux, S. (2006). "finite-element" displacement fields analysis from digital images: Application to portevin–le châtelier bands. Experimental Mechanics, 46. https://doi.org/10.1007/s11340-006-9824-8

Besnard, G., Leclerc, H., Hild, F., Roux, S., & Swiergiel, N. (2012). Analysis of image series through global digital image correlation. The Journal of Strain Analysis for Engineering Design, 47, 214–228. https://doi.org/10.1177/0309324712441435

Björck, Å. (1967). Solving linear least squares problems by gram-schmidt orthogonalization [Cited by: 332]. BIT, 7(1), 1–21. https://doi.org/10.1007/BF01934122

Bouledroua, O., Meliani, M. H., & Pluvinage, G. (2016). A review of t-stress calculation methods in fracture mechanics computation. Nature & Technology/Nature & Technologie, (15).

Bower, A. (2009). Applied mechanics of solids. CRC Press. https://books.google.nl/books?id=1%5C_sCzMNZMEsC

Bracewell, R. N., & Bracewell, R. N. (1986). The fourier transform and its applications (Vol. 31999). McGraw-Hill New York.

Bureau Veritas. (2020). Rule note ni 611 dt r01 e. Guidelines for fatigue assesment of ships and offshore units.

Bureau Veritas. (2022). Part b, ch7, sec4. Rules for the classification of steel ships.

Caporossi, P., Mazzanti, P., & Bozzano, F. (2018). Digital image correlation (dic) analysis of the 3 december 2013 montescaglioso landslide (basilicata, southern italy): Results from a multi-dataset investigation. ISPRS International Journal of Geo-Information, 7(9). https://doi.org/10.3390/ijgi7090372

Chen, J., & Liu, Y. (2022). Fatigue modeling using neural networks: A comprehensive review. Fatigue & Fracture of Engineering Materials & Structures, 45(4), 945–979.

Cisilino, A., & Aliabadi, M. (1997). Three-dimensional bem analysis for fatigue crack growth in welded components. International Journal of Pressure Vessels and Piping, 70(2), 135–144. https://doi.org/https://doi.org/10.1016/S0308-0161(96)00031-2

Clark, G., & Knott, J. (1975). Measurement of fatigue cracks in notched specimens by means of theoretical electrical potential calibrations. Journal of the Mechanics and Physics of Solids, 23(4), 265–276. https://doi.org/https://doi.org/10.1016/0022-5096(75)90028-9

Dekking, F. M., Kraaikamp, C., Lopuhaä, H. P., & Meester, L. E. (2005). A modern introduction to probability and statistics: Understanding why and how (Vol. 488). Springer.

den Besten, H. (2015). Fatigue resistance of welded joints in aluminium high-speed craft: A total stress concept (Doctoral dissertation). https://doi.org/10.4233/uuid:370b3d44-f4a6-403e-9629-d36174c3aca4

den Besten, H. (2018). Fatigue damage criteria classification, modelling developments and trends for welded joints in marine structures. Ships and Offshore Structures, 13(8), 787–808. https://doi.org/10.1080/17445302.2018.1463609

Dong, P. (2001). A structural stress definition and numerical implementation for fatigue analysis of welded joints. International Journal of Fatigue, 23(10), 865–876.

Dong, P., Hong, J. K., & De Jesus, A. M. P. (2006). Analysis of Recent Fatigue Data Using the Structural Stress Procedure in ASME Div 2 Rewrite. Journal of Pressure Vessel Technology, 129(3), 355–362. https://doi.org/10.1115/1.2748818

El-Awady, K. A., Lavenstein, S., & El-Awady, J. A. (2023). Three-dimensional surface displacement tracking for in-situ experiments: An alternative to digital image correlation (dic). Scripta Materialia, 224. https://doi.org/10.1016/j.scriptamat.2022.115120

Elguedj, T., Jan, Y., Combescure, A., Leblé, B., & Barras, G. (2018). X-fem analysis of dynamic crack growth under transient loading in thick shells. International Journal of Impact Engineering, 122, 228–250. https://doi.org/https://doi.org/10.1016/j.ijimpeng.2018.08.013

Gandossi, L., Summers, S., Taylor, N., Hurst, R., Hulm, B., & Parker, J. (2001). The potential drop method for monitoring crack growth in real components subjected to combined fatigue and creep conditions: Application of fe techniques for deriving calibration curves. International Journal of Pressure Vessels and Piping, 78(11), 881–891. https://doi.org/https://doi.org/10.1016/S0308-0161(01)00103-X

Grebenyuk, A. A., & Ryabukho, V. P. (2011). Digital image correlation with fast Fourier transform for large displacement measurement. In V. V. Tuchin & E. A. Genina (Eds.), Saratov fall meeting 2010: Optical technologies in biophysics and medicine xii (79990B). SPIE. https://doi.org/10.1117/12.887673

Henninger, C., Roux, S., & Hild, F. (2010). Enriched kinematic fields of cracked structures. International Journal of Solids and Structures, 47(24), 3305–3316. https://doi.org/https://doi.org/10.1016/j.ijsolstr.2010.08.012

Hild, F., Raka, B., Baudequin, M., Roux, S., & Cantelaube, F. (2002). Multiscale displacement field measurements of compressed mineral-wool samples by digital image correlation. Appl. Opt., 41(32), 6815–6828. https://doi.org/10.1364/AO.41.006815

Hild, F., & Roux, S. (2008). Correliq4: A software for finite element displacement field measurements by digital image correlation. Rapport interne LMT Cachan, 269, 195.

Hild, F., & Roux, S. (2012). Comparison of local and global approaches to digital image correlation. Experimental Mechanics, 52. https://doi.org/10.1007/s11340-012-9603-7

Hobbacher, A. et al. (2016). Recommendations for fatigue design of welded joints and components (Vol. 47). Springer.

Janssen, M., Zuidema, J., & Wanhill, R. (2004). Fracture mechanics - 2nd edition. (Vol. 2nd edition). Spon Press.

Leplay, P., Réthoré, J., Meille, S., & Baietto, M.-C. (2011). Identification of damage and cracking behaviours based on energy dissipation mode analysis in a quasi-brittle material using digital image correlation. International Journal of Fracture, 171, 35–50. https://doi.org/10.1007/s10704-011-9624-8

Lewis, J. (2001). Fast normalized cross-correlation. Ind. Light Magic, 10.

Long, X., Zhao, S., Jiang, C., Li, W., & Liu, C. (2021). Deep learning-based planar crack damage evaluation using convolutional neural networks [Cited by: 12]. Engineering Fracture Mechanics, 246. https://doi.org/10.1016/j.engfracmech.2021.107604

Luo, P. F., Chao, Y. J., Sutton, M. A., & Peters, W. H. (1993). Accurate measurement of three-dimensional deformations in deformable and rigid bodies using computer vision. Experimental Mechanics, 33, 123–132.

Maljar, D., & Stopjaková, V. (2021). Understanding the fourier and laplace transforms through visual interpretation. 2021 19th International Conference on Emerging eLearning Technologies and Applications (ICETA), 231–236. https://doi.org/10.1109/ICETA54173.2021.9726659

Mathieu, F., Hild, F., & Roux, S. (2012). Identification of a crack propagation law by digital image correlation. International Journal of Fatigue, 36(1), 146–154. https://doi.org/https://doi.org/10.1016/j.ijfatigue.2011.08.004

Oertel, G. (1996). Stress and deformation: A handbook on tensors in geology.

Pan, B., Xie, H., & Wang, Z. (2010). Equivalence of digital image correlation criteria for pattern matching. Appl. Opt., 49(28), 5501–5509. https://doi.org/10.1364/AO.49.005501

Prins, H. (n.d.). https://www.tudelft.nl/en/cse/events/partners-stakeholders-events-1/kick-off-dcse-event-entitled-future-computing/speakers/drir-hj-prins visited on: 28-9-2021

Qin, Y., den Besten, H., Palkar, S., & Kaminski, M. L. (2021). Mid- and high-cycle fatigue of welded joints in steel marine structures: Effective notch stress and total stress concept evaluations. International Journal of Fatigue, 142, 105822. https://doi.org/https://doi.org/10.1016/j.ijfatigue.2020.105822

Qin, Y., den Besten, H., Kaminski, M., & Palkar, S. (2019). Fatigue design of welded double-sided t-joints and double-sided cruciform joints in steel marine structures: A total stress concept. Fatigue & Fracture of Engineering Materials & Structures, 42. https://doi.org/10.1111/ffe.13089

Ravandi, S. H., & Toriumi, K. (1995). Fourier transform analysis of plain weave fabric appearance. Textile Research Journal, 65(11), 676–683. https://doi.org/10.1177/004051759506501108

Réthoré, J., Hild, F., & Roux, S. (2008). Extended digital image correlation with crack shape optimization [Cited by: 196; All Open Access, Green Open Access]. International Journal for Numerical Methods in Engineering, 73(2), 248–272. https://doi.org/10.1002/nme.2070

Réthoré, J., Roux, S., & Hild, F. (2011). Optimal and noise-robust extraction of fracture mechanics parameters from kinematic measurements. Engineering Fracture Mechanics, 78(9), 1827–1845. https://doi.org/https://doi.org/10.1016/j.engfracmech.2011.01.012

Rice, J. R. (1968). A path independent integral and the approximate analysis of strain concentration by notches and cracks.

Roux, S., & Hild, F. (2006). Stress intensity factor measurements from digital image correlation: Post-processing and integrated approaches. International Journal of Fracture, 140. https://doi.org/10.1007/s10704-006-6631-2

Roux, S., Réthoré, J., & Hild, F. (2009). Digital image correlation and fracture: An advanced technique for estimating stress intensity factors of 2d and 3d cracks. Journal of Physics D Applied Physics, 42. https://doi.org/10.1088/0022-3727/42/21/214004

Roux-Langlois, C., Gravouil, A., Baietto, M.-C., Réthoré, J., Mathieu, F., Hild, F., & Roux, S. (2015). Dic identification and x-fem simulation of fatigue crack growth based on the williams' series. International Journal of Solids and Structures, 53, 38–47. https://doi.org/https://doi.org/10.1016/j.ijsolstr.2014.10.026

Schafer, R. W. (2011). What is a savitzky-golay filter? [lecture notes]. IEEE Signal Processing Magazine, 28(4), 111–117. https://doi.org/10.1109/MSP.2011.941097

Sutton, M. . A. ., Orteu, J. . J. ., & Schreier, H. . (2009). Image Correlation for Shape, Motion and Deformation Measurements: Basic Concepts,Theory and Applications (2009th ed.). Springer.

Tada, H., Paris, P., & Irwin, G. (2000). The stress analysis of cracks handbook. ASME Press. https://books.google.nl/books?id=9tfAQgAACAAJ

Tanaka, K., Nakai, Y., & Yamashita, M. (1981). Fatigue growth threshold of small cracks. International Journal of Fracture, 17, 519–533.

Van Loan, C. (1992). Computational frameworks for the fast fourier transform. Society for Industrial; Applied Mathematics. https://doi.org/10.1137/1.9781611970999

Vargas, R., Neggers, J., Canto, R., Rodrigues, J., & Hild, F. (2016). Analysis of wedge splitting test on refractory castable via integrated dic. Journal of the European Ceramic Society, 36(16), 4309–4317. https://doi.org/https://doi.org/10.1016/j.jeurceramsoc.2016.07.007

Vargas, R., Neggers, J., Canto, R., Rodrigues, J., & Hild, F. (2018). Comparison of two full-field identification methods for the wedge splitting test on a refractory. Journal of the European Ceramic Society, 38(16), 5569–5579. https://doi.org/https://doi.org/10.1016/j.jeurceramsoc.2018.07.039

Volkov, V., Zhu, Y., & De Graef, M. (2002). A new symmetrized solution for phase retrieval using the transport of intensity equation. Micron, 33(5), 411–416. https://doi.org/https://doi.org/10.1016/S0968-4328(02)00017-3

Wang, B., Pan, B., & Lubineau, G. (2015). Some practical considerations in finite element-based digital image correlation. Optics and Lasers in Engineering, 73, 22–32. https://doi.org/https://doi.org/10.1016/j.optlaseng.2015.03.010

Williams, M. L. (1952). Stress singularities resulting from various boundary conditions in angular corners of plates in extension. Journal of Applied Mechanics, 19(4), 526–528.

Williams, M. L. (1957). On the stress distribution at the base of a stationary crack.

Wu, Z., Guo, W., Chen, Z., Wang, H., Li, X., & Zhang, Q. (2022). Three-dimensional shape and deformation measurement on complex structure parts [Cited by: 0; All Open Access, Gold Open Access, Green Open Access]. Scientific Reports, 12(1). https://doi.org/10.1038/s41598-022-11702-x

Xiao, Z.-G., & Yamada, K. (2004). A method of determining geometric stress for fatigue strength evaluation of steel welded joints. International Journal of Fatigue, 26(12), 1277–1293. https://doi.org/https://doi.org/10.1016/j.ijfatigue.2004.05.001

Xu, X., Su, Y., Cai, Y., Cheng, T., & Zhang, Q. (2015). Effects of various shape functions and subset size in local deformation measurements using dic. Experimental Mechanics, 55, 1575–1590.

Yang, J., & Bhattacharya, K. (2019). Augmented lagrangian digital image correlation. Experimental Mechanics, 59, 187–205.

Zi, G., & Belytschko, T. (2003). New crack-tip elements for xfem and applications to cohesive cracks. International Journal for Numerical Methods in Engineering, 57, 2221–2240. https://doi.org/10.1002/nme.849

Zienkiewicz, O. . C. ., & Taylor, R. . L. . (2000). Finite Element Method: Volume 1, Fifth Edition (Finite Element Method Ser) (5th ed.). Butterworth-Heinemann.